IDO / 78-1701.a.3

TOPICAL REPORT

INTERPRETATION OF A SEISMIC REFRACTION PROFILE ACROSS THE ROOSEVELT HOT SPRINGS, UTAH AND VICINITY

by

Rodney C. Gertson and Robert B. Smith

Work performed under Contract No.

DE-AC07-78ET28392

Department of Geology and Geophysics

University of Utah

Salt Lake City, Utah (USA)

March 1979

Prepared for

DEPARTMENT OF ENERGY

Division of Geothermal Energy

DISCLAIMER

NOTICE

This report was prepared to document work sponsored by the United States Government. Neither the United States nor its agent, the United States Department of Energy, nor any Federal employees, nor any of their contractors, subcontractors or their employees, makes any warranty, express or implied, or assumes any legal liability or responsibility for the accuracy, completeness, or usefulness of any information, apparatus, product or process disclosed, or represents that its use would not infringe privately owned rights.

NOTICE

Reference to a company or product name does not imply approval or recommendation of the product by the University of Utah or the U.S. Department of Energy to the exclusion of others that may be suitable.

WBM

ABSTRACT

In April, 1977, a seismic refraction profile was recorded across the Milford Valley, the Roosevelt Hot Springs KGRA, and the northern Mineral Mountains in southwestern Utah. Seven shot points were used to provide multiple subsurface seismic refraction coverage along the 30 km east-west profile line. Since an inspection of power spectrums revealed large components of 60 Hz noise on some traces, computer routines were used to low-pass filter all seismograms. Amplitude information was utilized by normalizing all traces that recorded the same blast.

Subsurface structural modeling was conducted by means of first arrival P-wave delay-time analysis and ray tracing. Herglotz-Wiechert travel-time inversion was used for the velocity-depth distribution in the Mineral Mountains. The interpretation of the P-wave travel-times suggests that the Milford Valley fill consists of two units with a total thickness of at least 1.8 km. The surficial layer is composed of Quaternary sands and clays with a velocity of 1.8 km/s. A deeper horizon with a velocity of 4.0 km/s is interpreted to be Tertiary sediments on the basis of gravity modeling across the Milford Valley using estimated densities from velocity-density relationships. The deepest layer identified from the seismic data is interpreted as a bedrock unit of Precambrian(?) gneisses. A true velocity of 6.7 km/s for the valley basement was determined from reversed subsurface

P-waves and from a sonic log obained in a well drilled into metamorphics near the refraction line.

In the vicinity of the Roosevelt KGRA, a thin low velocity alluvial layer covers a basement igneous complex with a velocity of 5.2 km/s. Synthetic seismograms suggest that a slight velocity gradient in the upper 0.1 km of basement rock may account for the absence of reflections in the record sections. Analysis of the refraction data also indicates that the main range front faulting begins at least one kilometer west of the Opal Mound fault. Amplitude decay of the first P-wave arrivals shows decreased attenuation for seismic waves that propagate across the hot springs area.

Granite velocities between 3.3 km/s and 4.0 km/s were calculated from the travel-times in the Mineral Mountains. These velocities may not be representative of the majority of the pluton because the refraction profile closely followed the east-west Hot Springs fault zone. An east dipping 5.5 km/s layer at a depth between 0.7 km and 1.5 km beneath the range corresponds to an increase in velocity indicated on a sonic log at the eastern edge of the geothermal area.

ACKNOWLEDGMENTS

I would like to express my gratitude to the Supervisory committee members. Dr. R. B. Smith supervised the research and assisted in the preparation of the manuscript. Drs. D. S. Chapman and W. P. Nash examined the thesis and proposed many valuable suggestions.

Fieldwork was conducted under the direction of Dr. R. B. Smith with the assistance of Dr. W. R. Sill of the University of Utah and Mr. W. H. Jackson, formerly of the U.S.G.S. The magnetic tape decoding program was written by C. Nutter, of the Department of Geology and Geophysics. Dr. J. Scott at the U.S. Geological Survey, Denver, provided the seismic refraction interpretation package.

A special thanks is extended to Dr. J. Ansorge visiting from the Institute of Geophysics, Swiss Federal Institute of Technology, Zurich. He contributed many hours of discussion that were greatly appreciated. Numerous students helped in my understanding of this project along with several workers at the Earth Science Laboratory of the University of Utah Research Institute.

My sincere appreciation is also given to my wife, Susan. She encouraged and assisted in various ways throughout my studies.

Financial support was provided to me by a Shell Fellowship in Geophysics for the academic year 1976-77, a Mobil Oil Corp. grant, and the Special Geophysics Fund for 1977-78. Research funding came under the Department of Energy, Division of Geothermal Energy (DOE/DGE) contract DE-AC07-78ET28392.

TABLE OF CONTENTS

ILLUSTRATIONS

Illustrations (continued)

CHAPTER 1

INTRODUCTION

Increasing demand by the public and private industry for energy have put severe strains on current energy sources. For this reason, new alternate energy sources must be exploited. Geothermal power is one alternative with a promising future.

Geophysical exploration methods, principally heat flow and electrical measurements, have been used for some time to assist in locating and delineating geothermal areas. However, because of both geologically complex conditions and in many cases a lack of discernable earthquakes, conventional seismological methods have not been routinely implemented. Microearthquake surveys and ground noise studies have been the most commonly attempted passive seismological methods. Active seismic exploration methods, i.e., refraction and reflection, have met with only moderate success due to disturbing ground noise and unusually high attenuation of seismic waves (Hochstein and Hunt, 1970).

Before the interpretation of seismic data can be begun, the physical basis of seismological techniques for the exploration of geothermal resources must be understood. The characterisitics of P- and S-wave propagation through a hydrothermal reservoir will reflect the average static reservoir properties. Velocity and attenuation of seismic waves are influenced by several factors, all or none of which

may be anomalous in a geothermal system. These include rock type, porosity, water content, temperature, pressure, and degree of fracturing. As these parameters vary the associated elastic properties of the rock changes. If high temperatures, high porosity, and fracture zones exist in a geothermal system relatively low velocities and high attenuation may occur. However, metamorphism and induration of sediments by silica or carbonates may increase seismic velocities and produce a decrease in attenuation. A combination of these effects may result in an insignificant velocity change (or impedance) or a small change in attenuation.

Seismic refraction surveys of geothermal areas have not been employed extensively compared with other geophysical methods. In the past, refraction has generally been used as a reconnaissance tool for near- surface structure. Palmasson (1975) suggests that refraction is quite useful in volcanic and geologically complex areas, especially in conjunction with gravity surveys since density and seismic velocity are empirically related. When an anomalous mass distribution is detected by gravity, the source can not be unambiguously interpreted without the information that a refraction survey could provide.

Several refraction surveys have been undertaken in geothermal areas around the world. In Iceland, Bjornsson et al. (1970) studied the Reykjanes thermal field and found that aquifer bearing horizons were more abundant in association with deeper material than in shallow, more porous layers. Investigations in the Long Valley, California, caldera by Hill (1976) gave possible evidence for the roof of a magma chamber at a depth of 7 to 8 km. Arrivals on two

refraction record sections with higher apparent velocities than the first arrivals and 180° phase shifts were interpreted as being reflections from a horizon across which the velocity decreases with depth. Hill (1976) also found near-surface effects of the hydrothermal system in the changing frequency content of wave groups.

Hochstein and Hunt (1970), using refraction methods at the Broadlands geothermal field in New Zealand, outlined two large buried domes of rhyolite by contouring the depths to the refracting interface. Record sections indicated an increase in P-wave velocity where thermal alteration increased and areas of warm and steaming ground experienced greater attenuation than regions outside the geothermal field. On the other hand, Majer and McEvilly (1979) found less attenuation in the production zone of the Geysers geothermal system of northern California than outside of it. This is also true at the Leach Hot Springs in Nevada where the densification of sediments by the deposition of silica is believed to be the cause for the decrease in attenuation and an increase in P-wave velocity (Beyer et al., 1976).

The Roosevelt Known Geothermal Resource Area (KGRA), located 19 kilometers northeast of Milford, Utah, has been studied extensively by the University of Utah in order to determine its energy potential. Temperature measurements in 47 drill holes have defined the size and shape of the near surface hydrothermal system (Ward et al., 1978). Heat flow values range from subnormal (< 100 mW/m^2) in the Mineral Mountains to > 8 W/m^2 in the heart of the thermal anomaly. To gather additional information about the geothermal regime, a reversed

refraction profile with seven shot points was recorded across the Milford Valley, the Roosevelt Hot Springs KGRA, and the northern Mineral Mountains during April, 1977. The experiment was planned and supervised by the Department of Geology and Geophysics of the University of Utah and conducted under sub-contract by the Microgeophysics Corporation.

The principal objective of this thesis was the interpretation of the multifold seismic refraction data across the Roosevelt KGRA. The interpretation involved the definition of the upper-crustal velocity structure and how the structure might effect the reservoir and flow properties of the heat source. Other geophysical data indicate numerous north-south normal faults bounding the eastern edge of the Milford Valley and dissecting the Roosevelt KGRA. The seismic experiment was planned to better define the fault locations since they may control fluid conduits in the geothermal reservoir. A secondary and long-term objective was to directly assess the source of the thermal anomaly by use of the seismic refraction method. Goldstein et al. (1978) have stated that to date, no direct evidence for near surface melts or fractional melts have been found to be associated with known geothermal reservoirs. However, Sanford et al. (1977) have suggested the existence of a magma at a depth of 18 km to 20 km beneath Socorro, New Mexico, by analysis of S_XP and S_XS reflections on microearthquake seismograms. The work reported in this thesis describes the seismic refraction experiment and presents the interpretation of its results.

CHAPTER 2

GEOLOGY AND GEOPHYSICS

The Roosevelt Hot Springs KGRA and the surrounding region are located at the eastern edge of the Basin and Range physiographic province, near the transition to the Colorado Plateau. The Mineral Mountains are an uplifted horst flanked by two alluvium-filled grabens with the Beaver Valley to the east and the Milford Valley to the west. Relief between the valleys and the ranges is as large as 1.3 km.

The Mineral Mountains are dominated by a Tertiary granitic pluton covering approximately 250 square kilometers that is the largest outcropping intrusive body in Utah (Figure 1). The pluton is cut extensively by acidic and basic dikes, most of which are striking north-south. Also, extensive Quaternary volcanism has occurred along the length of the range.

Evans (1978) mapped over a dozen Quaternary rhyolite domes and flows in the central Mineral Mountains. K-Ar dating has established their ages to be between 0.8 and 0.5 m.y. (Ward et al, 1978). Similarities in the petrologic and chemical composition of the domes suggest they probably originated from the same magma source that was produced by partial fusion of crustal rocks.

Cambrian-age sedimentary rocks are found at the northern end of the range while Permian limestones and Mesozoic limestones, shales, and sandstone are found in the southern and southeastern portion of

Figure 1. General geologic map of the Milford Valley and the Mineral Mountains, Beaver County, Utah. Data compiled primarily from Evans (1977) and Nielson et al. (1978).

Legend

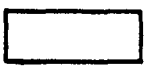

Quaternary alluvium

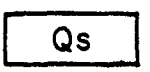

Quaternary hot spring deposits

Quaternary basalts

Quaternary rhyolite flows and domes

Mesozoic and Paleozoic sedimentary rocks

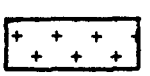

Tertiary granite

Precambrian (?) gneiss

faults

geologic contact

shot point locations

well locations of sonic logs

near surface hydrothermal system, 400 mW/m^2 contour from Ward et al. (1978)

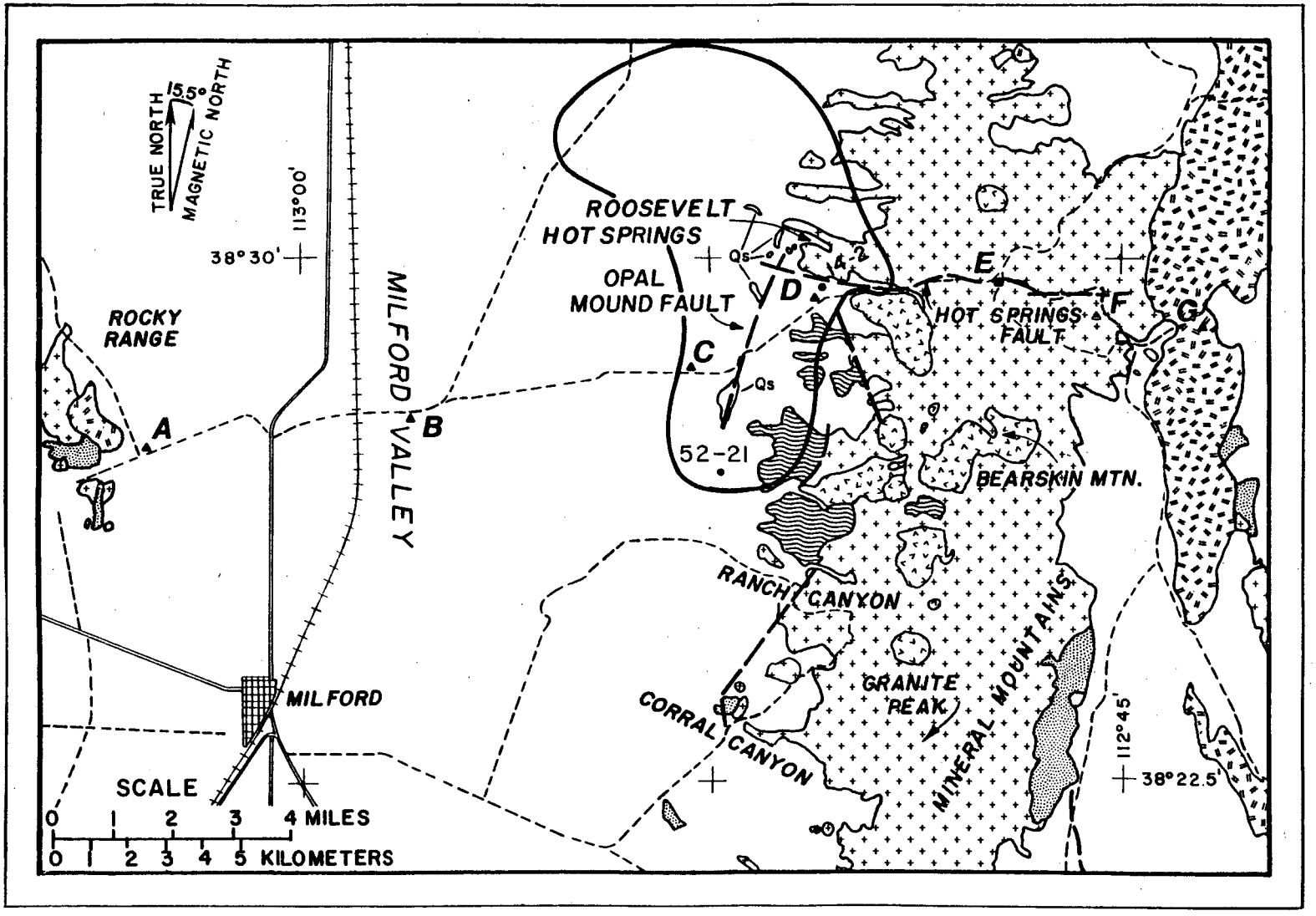
TRUE NORTH
15°
MAGNETIC NORTH
113°00'
38°30'
ROCKY RANGE
MILFORD VALLEY
ROOSEVELT HOT SPRINGS
OPAL MOUND FAULT
HOT SPRINGS FAULT
A
B
C
D
E
F
G
Qs
52-21
BEARSKIN MTN.
RANCH CANYON
GRANITE PEAK
CORRAL CANYON
MINERAL MOUNTAINS
MILFORD
112°45'
38°22.5'
SCALE
0 1 2 3 4 MILES
0 1 2 3 4 5 KILOMETERS

the Mineral Mountains. Paleozoic sedimentary rock outcrops on the western side of the Milford Valley.

A belt of gneiss and schist along the western flank of the Mineral Mountains is invaded by the principal phase of the Tertiary granite. On the basis of lithologic similarity with Precambrian rocks found in Utah, these metamorphic rocks are tentatively assigned a Precambrian age. The westernmost exposures of the metamorphics are found in a horst block bounded on the east by the Opal Mound fault. Additional discussions of the geology of the Mineral Mountains can be found in Earll (1957), Liese (1957), Condie (1960), Lipman et al. (1978), and Evans (1978).

The seismic refraction profile reported here extended from the Rocky Range, on the western side of the Milford Valley, 30 km across the Roosevelt Hot Springs area to the eastern edge of the Mineral Mountains (Figure 1). Shot points A, B, C, and D were detonated within valley fill. Gravity profiles by Carter and Cook (1978) suggest that the depth to bedrock in the valley reaches a depth of 1.5 km. Shot point B, near the center of the valley, is located above the area of maximum alluvium thickness. Thinning of the alluvial cover must occur to the east and west since bedrock outcrops on both sides of the valley. This is confirmed by the presence of igneous rock encountered at 76 m depth in Thermal Power drillhole 14-2 located approximately 0.4 km north of shot point D. The remainder of the shot locations were in igneous rock. Shot points E and F were exploded in granite, and shot point G was exploded in a Quaternary basalt flow.

Of special interest to the energy industry is the Roosevelt Hot

Springs geothermal prospect at the western edge of the Mineral Mountains near Hot Springs Wash. Located here are a 6 km by 12 km thermal field with thermal gradient measurements up to 960° C/km and a zone of hydrothermal alteration representative of a shallow hydrothermal system. A system of faults that controls the near-surface fluid flow governs the shape of anomalous zones of low resistivity (Ward and Sill, 1976) and high heat flow (Sill and Bodell, 1977; Wilson and Chapman, 1978).

Numerous faults in the Roosevelt KGRA were mapped using geology, aerial photography, resistivity, gravity, and magnetic data. The youngest faults are north north-east trending and control the present hydrothermal activity. East-west faulting inferred by the presence of several valleys that extend through the Mineral Mountains and into the alluvium to the west has been produced by regional zones of weakness. Nielson et al. (1978) propose that the geothermal reservoir is controlled by the intersections of these principal zones of faulting.

Peterson (1975), Parry (1978), and Nielson et al. (1978) have conducted detailed geologic mapping of the KGRA and the surrounding area. Widespread hot spring deposits along the Opal Mound fault are primarily composed of siliceous sinter and sinter-cemented alluvium resulting from the deposition of silica. Although displacement on the Opal Mound fault, as interpreted from gravity measurements (Crebs and Cook, 1976), is only about 50 m the fault appears to be the major controlling structure in the hydrologic regime since the anomalous zone of heat flow is centered upon the fault.

Extensive geophysical work in the Roosevelt thermal area has been

summarized in Ward et al. (1978). Crebs and Cook (1976), Thangsuphanich (1976), Brumbaugh and Cook (1978), and Carter and Cook (1978) have given results of gravity and magnetic surveys. An elongate gravity low with 2 mgal closure corresponding to a series of rhyolite domes possibly indicates a low-density continuous intrusive body at about 2 km depth (Crebs and Cook, 1976). Small P-wave delays of up to 0.2 sec measured at stations on the west flank of the Mineral Mountains from earthquakes 30 km to the northeast may have been produced by an upper crustal low-velocity layer beneath the Mineral Mountains (Olson and Smith, 1976). Also, qualitative estimates of S-wave attenutation for ray paths that propogate beneath the Mineral Mountains and surface south of the Roosevelt Hot Springs suggest a low-Q transmission path. Both the low-velocity effect and the shear wave attenuation indicate the possibility of partial melting beneath the Mineral Mountains.

Electromagnetic and Schlumberger resistivity sounding by Tripp et al. (1978) indicates a zone of low resistivity material of about 5 Ω-m at depth of 50 m that parallels the Opal Mound fault. Intensely fractured and altered water-saturated rock is the probable cause of the low resistivity of this zone. Beneath the conductive zones is a resistive basement of essentially nonporous and unaltered rock. One-dimensional inversion of magnetotelluric soundings in the Roosevelt Hot Springs area by Wannamaker (1978) suggests an estimate of very low resistivities, less than 0.1 Ω-m at depths of 2 km to 5 km. These values are virtually impossible to obtain considering the present interpretation of the subsurface geology.

Figure 2 presents generalized sonic and lithologic logs from two wells in the vicinity of the Roosevelt Hot Springs that were used in the interpretation of the refraction data. Getty Oil Co. Well 52-21 located 2.5 km southeast of shot point C (Figure 2a) was drilled into upper amphibolite facies metamorphic rocks identified as gneiss (Ballantyne, 1978). Except for a dacite dike at a depth near 0.6 km, no other significant rock type was encountered. P-wave velocities varied from 5.5 km/s at 0.2 km depth to a maximum of 6.7 km/s at a depth of 0.8 km.

The dominant rock type in Thermal Power Well 14-2 located 0.4 km north of shot point D (Figure 2b) was a granitic textured monzonite that probably corresponds to the mapped granite (Ballantyne and Parry, 1978). A dike of microgranite intersected the drillhole at a depth between 0.5 km and 0.7 km depth, and monzonite occurred in the remainder of the well but was occasionally cut by intermediate composition dikes. A plagioclase alteration intensity log is also included for Well 14-2 as an aid to identify the fracturing in the hole. P-wave velocities appear to vary more with the degree of alteration rather than lithology. The maximum velocity encountered was 5.5 km/s between 0.7 km and 1.0 km.

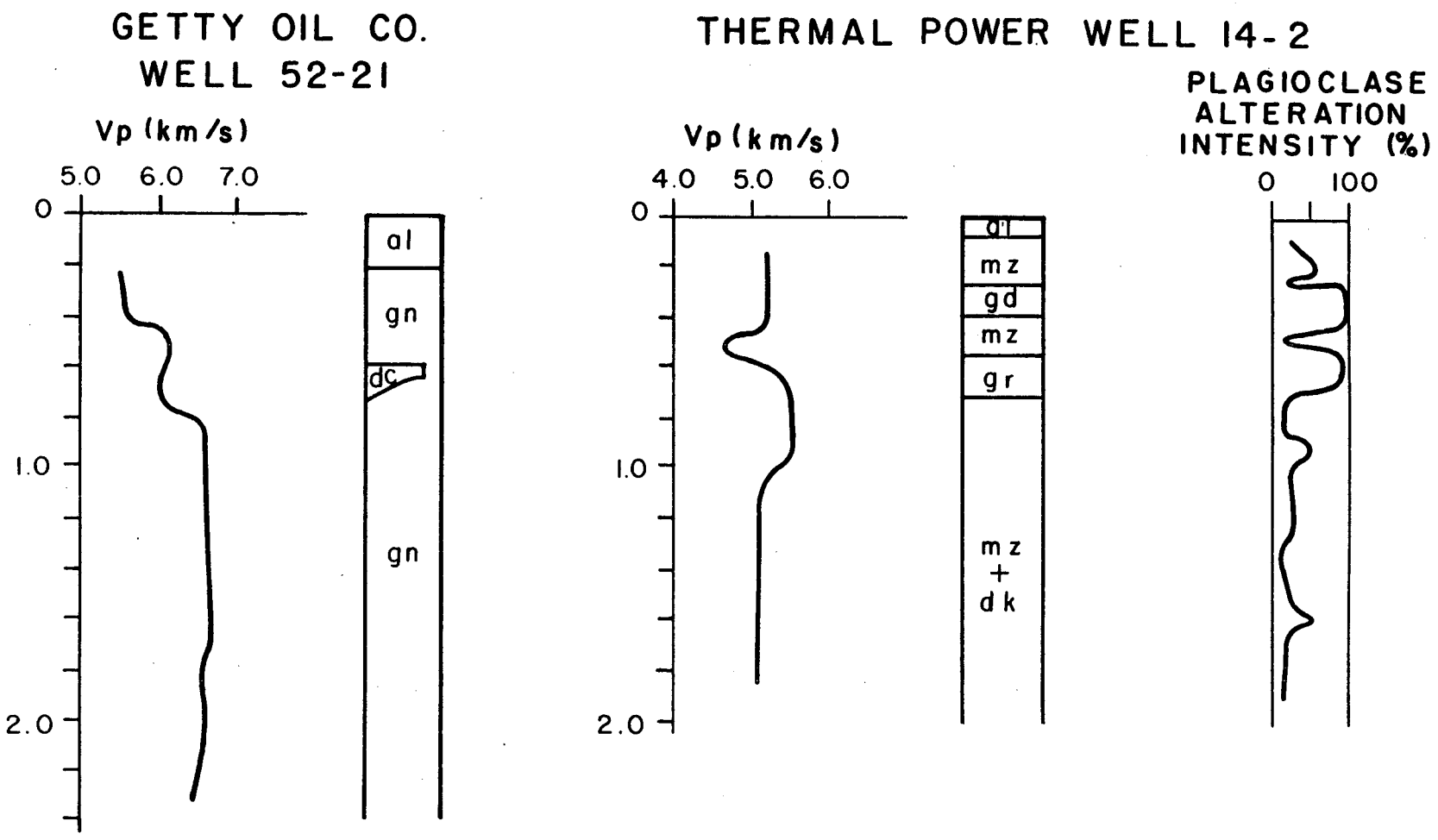

Figure 2. Generalized sonic and lithology logs used in refraction data interpretation (a) Getty Oil Co. well 52-21 drilled into metamorphic rocks (b) Thermal Power well 14-2 drilled into igneous rocks. Symbols are: al, alluvium; dc, dacite; dk, intermediate dikes; gd, granodiorite; gn, gneiss; gr, granite; mz, monzonite.

CHAPTER 3

SEISMIC DATA

Introduction

Under a subcontract from the University of Utah, the Microgeophysics Corporation of Golden, Colorado, recorded a seismic refraction profile across the Roosevelt Hot Springs KGRA. Field work began on April 20, 1977, and was completed on April 29, 1977. A report of preliminary results that described contract deliverable products was prepared by the Microgeophysics Corp. and presented to the Department of Geology and Geophysics in November, 1977. Items included the original digital field tapes, reformatted tapes, and datum corrected analog field records. Reproductions of 7 1/2-minute quadrangle topographic maps with each geophone and shotpoint location and an elevation cross-section of the profile were included. The coordinates for geophone and shotpoint locations were surveyed to the nearest meter on the Universal Transverse Mercator projection, zone 12, and elevations were recorded to the nearest foot. This information is tabulated in the contract report (Microgeophysics, 1977).

A spread of 24, vertical component geophones was employed in recording all data along the profile line with one geophone per station. Geophone spacing, though variable due to topography and surface features, was approximately 250 m. The geophone spread

occupied five, generally east-west sub-arrays of about 6 km length in order to cover the full 30 km length of the profile.

The geophones used for this experiment were model GEOSPACE HS-1 with a natural frequency of 4.5 Hz and damped at 0.6 of critical. Geophone output was recorded digitally on magnetic tape at a one millisecond (1 ms) sampling rate. The programmed gain control of the instruments was tripped far in advance of the shot so that the amplifiers settled to a final gain before the first seismic energy arrived at the geophones. Trace to trace variations were kept small by careful balancing of each channel. Typically, the instrument gain was 100 dB, which corresponds to one digital count per 0.007 microvolts input or 0.05 cm/s of ground motion per one count. Across the spread, gains were constant for all geophones while gains varied only slightly from spread to spread. The frequency response of the entire recording and geophone system is shown in Figure 3.

Seven shot locations were used during the experiment with each location having multiple shots. Charge weights depended upon the distance to the spread. For the largest blasts multiple holes were necessary to prevent blowouts. The Microgeophysics report lists the total charge weights for each blast and the length of the primacord used for ignition of the explosives in the hole.

Several shots were detonated and recorded into each spread in order to provide multiple subsurface coverage. All spreads were reversed except for the westernmost spread, no. 1, which received energy only from shot point A. Of the four reversed spreads, five shots were recorded by spread 2, six shots by spreads 3 and 4, and

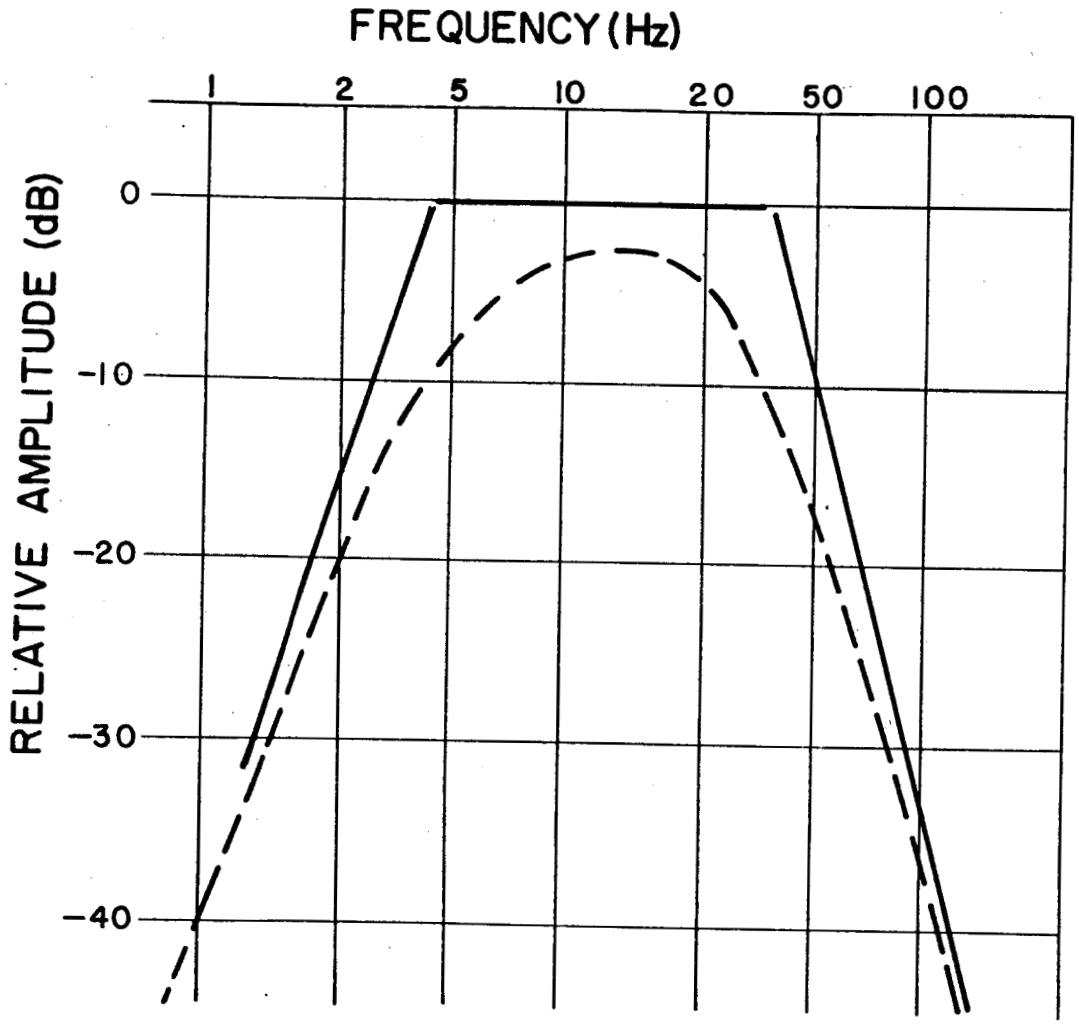

Figure 3. Frequency response of the recording and geophone system used in the seismic refraction profile (after Microgeophysics, 1977). Solid line is response with all filters out. Dashed line is response with 5 Hz low cut and 30 Hz high cut.

four shots by spread 5.

When recording was completed at one spread location, the seismometer array was moved, however the end geophone of the new spread occupied the same location as the end geophone of a previous spread in order to tie adjacent spreads together. This allowed the data to be correlated from one spread to another and provided an amplitude tie for normalized amplitude record sections.

The origin timing signal was recorded on channel 12 for all spreads except when channel 1 recorded the time break for shot A, spread 1. Due to the nature of the shot-spread configurations, where in many cases geophone 12 was far from the source, the origin-time signal was generated by the following method. A piece of wire stemming from an oscillator generating a 3 kHz signal was wrapped around the primacord used for ignition of the charges. The signal was relayed by FM radio to the recording truck located at the geophone array, and was the input for channel 12. When the primacord was detonated, an electrical connection was broken that stopped the broadcast of the 3 kHz signal. The receiving antenna detected this interruption and a large voltage change was recorded on the time-break channel input. However, the break was not the actual time of shot detonation but was about 5 ms before detonation. The actual origin time was calculated since both the primacord length and velocity of primacord detonation were known. The accuracy of the origin time is within ± 0.005 sec.

Data Processing

The original 21-track field tapes, on which the data were collected, were not convenient for routine computer analysis. Therefore, the Microgeophysics Corp. supplied three reformatted 9-track tapes containing the original field information. Other problems with reading bits on the 9-track tape required the use of a decoding program so that the information would be readily available in a readable form. The Appendix lists a program, TPREAD.DECODE, as well as all other Fortran programs necessary for this data manipulation.

Upon inspection of random traces from various spreads, it was noted that a high frequency component masked many signals to such an extent that the character of first and later arrivals were often indistinguishable. This prompted an inspection of the power spectrums using computer programs POWER.DRIVE and POWER.SPECT. Figures 4a and 4b are typical examples of the power spectrums of traces with and without the high-frequency noise. Note that most power in the seismograms was contained in frequencies below 40 Hz. This was true for all traces examined except for those showing large components of 60 Hz noise. Close proximity of high voltage powerlines to the recording spread is the most likely cause of the 60 Hz signal.

Power spectrum estimation was accomplished following the method described in Oppenheim and Schafer (1975). Since the Fourier transform of any real finite length sequence $x(n)$, $0 \leq n \leq N-1$, is

$$X(e^{j\omega}) = \sum_{n=0}^{N-1} x(n)e^{-j\omega n} \qquad (1)$$

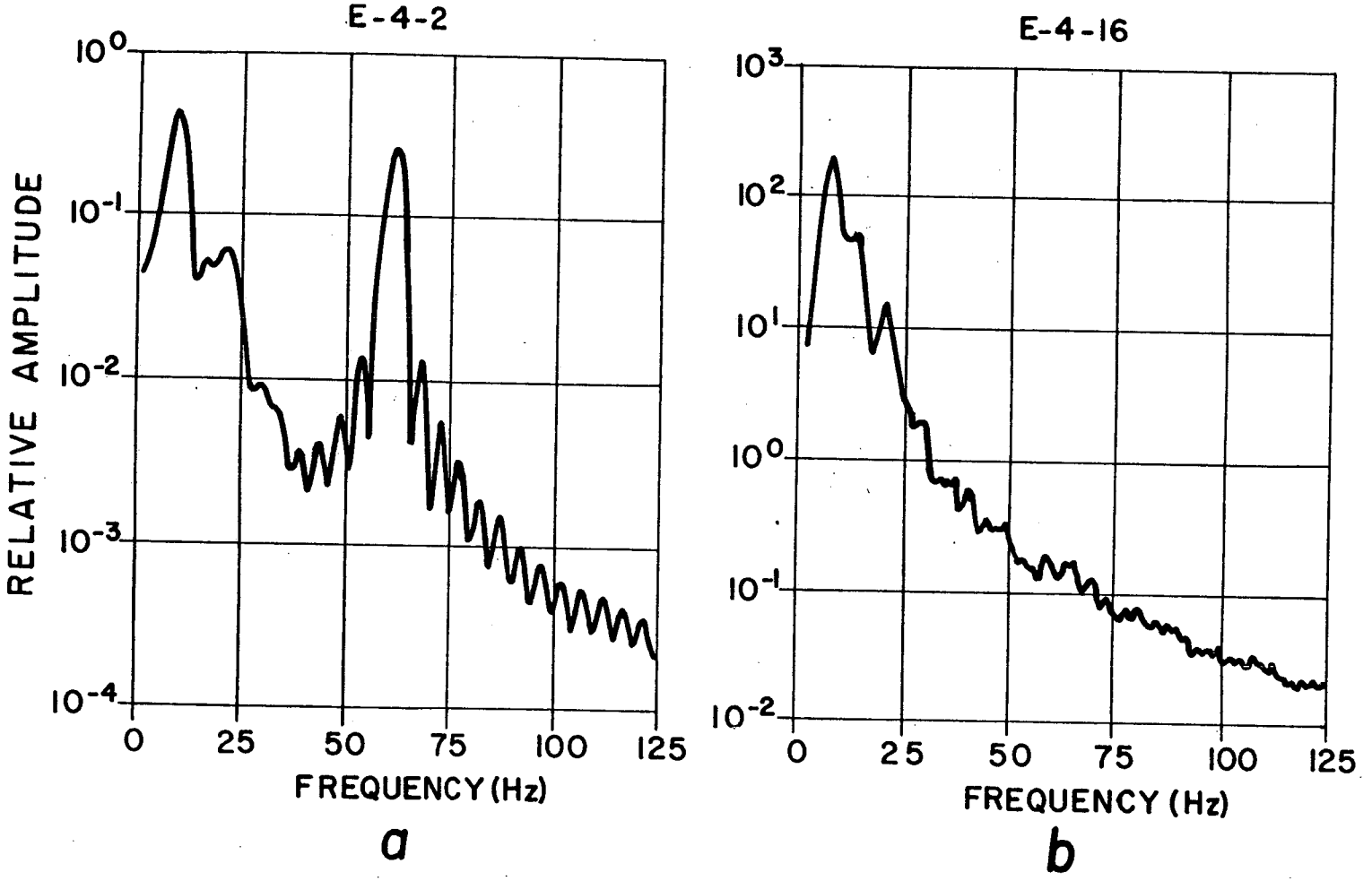

Figure 4. Power spectrums of two seismograms from spread 4, recording shot point E (a) trace 2 contains a large component of 60 Hz noise, most power contained in frequencies less than 30 Hz (b) trace 16, no 60 Hz noise, most power contained in frequencies less than 30 Hz.

the spectrum estimate or periodogram is

$$I_n(\omega) = \frac{1}{N}\left[x(e^{j\omega})\right]^2 \qquad (2)$$

However, this will not result in a consistent estimate of the power spectrum and the rapidity of fluctuations in the periodogram increases as N increases. The method used here is to smooth the periodogram by convolution with a spectrum window of known response. If $S(\omega)$ denotes the smoother periodogram, the periodogram is the Fourier transform of $c(m)$ and the window is $w(m)$, then

$$S(\omega) = \sum_{m=-(M-1)}^{M-1} c(m)\, W(m)\, e^{-j\omega m} \qquad (3)$$

Since the power spectrum is a non-negative function of frequency, we require that $S(\omega)$ be non-negative as well. A sufficient condition for $S(\omega)$ to be non-negative is that the Fourier transform of the window also be non-negative. Therefore, a Bartlett window is chosen for smoothing since the window's Fourier transform is non-negative and the window has a suitable sidelobe falloff rate.

Because of the difficulty of working with the three original data tapes (non-sequential ordering of spreads, 20 sec length records, trace header labels, etc.), it was necessary to create a new data file with information required for interpretation of the first P-wave arrivals. A computer program was designed to read, filter, decimate, and write the processed data onto a new tape. Four seconds of each trace were retained for P-wave analysis. Adequate time was allowed before the first arrival of energy on each trace so that noise levels could be judged when identifying phases.

Fortran programs REFRACTION.XYFLTR,.FILTER,.FORK,.STORE, and .WINDOW were used to process the traces (see Appendix for listings). As described earlier inspection of the power spectrums revealed most power to be in frequencies less than 40 Hz with significant components of 60 Hz noise often present. To remove the noise, a 128-point, low-pass filter with a cutoff frequency of 45 Hz was constructed. Smoothing of the filter was accomplished with a Hamming window and the result was causal and padded with zeroes out to 2^{12} points. The frequency response of the filter is shown in Figure 5 with some examples of the filter's effectiveness shown in Figures 6 and 7.

Since no significant power above approximately 60 Hz remained in any seismogram after filtering, and because a 1 ms sampling rate contains frequencies up to 500 Hz, it was decided to decimate the data. By taking every fourth sample (4 ms) the Nyquist frequency was set at 125 Hz, therefore, an anti-aliasing filter was not required. This decimation not only made the data easier to handle but it also reduced storage requirements considerably.

Identifying characters followed by the digitized filtered trace were written onto a new tape. The data were grouped by shots and ordered from west to east (shot A to shot G). The computer program REFRACSCTION.DISP was then used to plot the refraction data.

Normalized Amplitudes

To utilize amplitude information as well as travel-times from seismic data, it is necessary to adjust variations in trace amplitudes from spread to spread. The amplitude information determined from

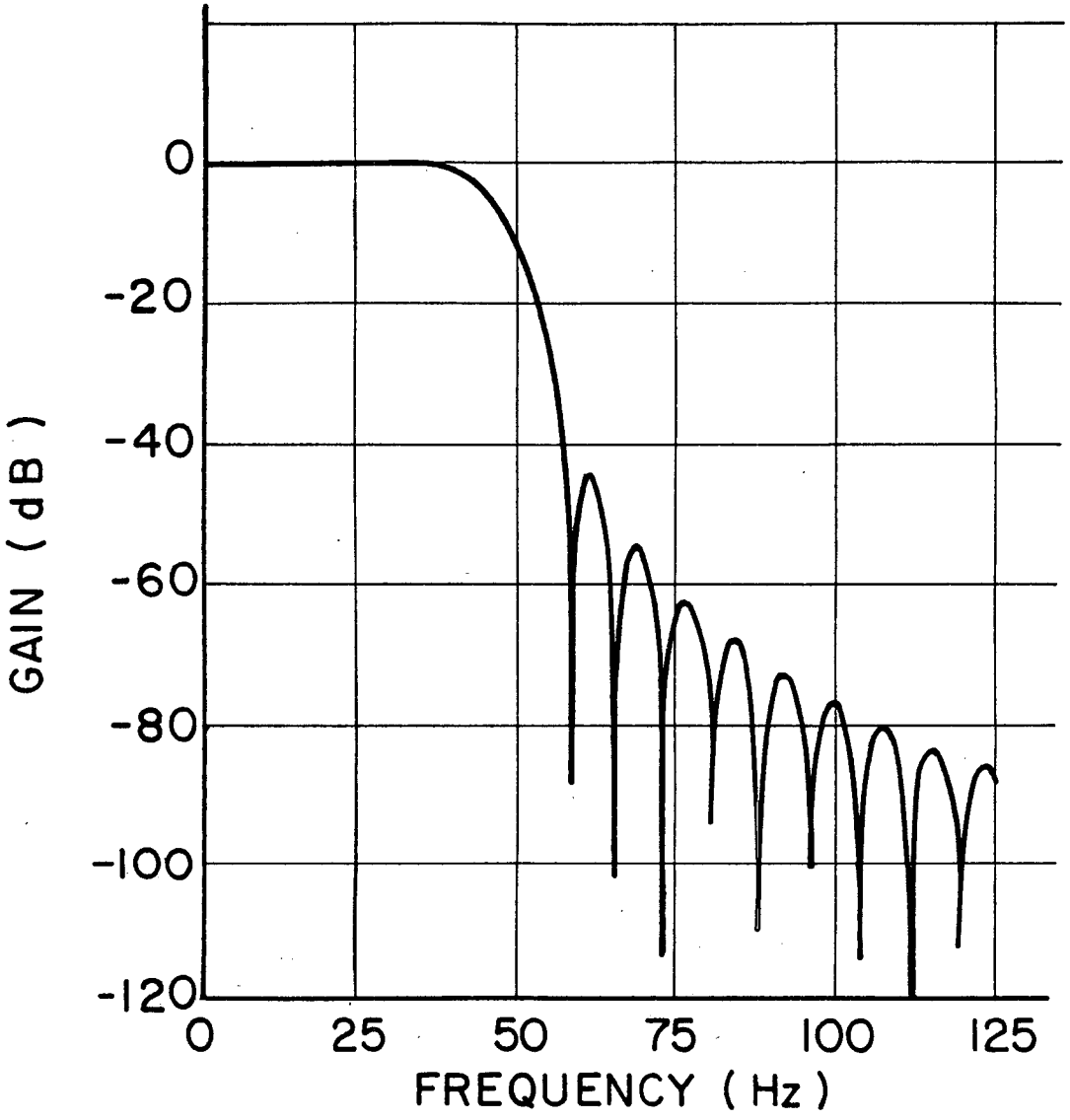

Figure 5. Frequency response of 128-point low pass filter applied to all seismograms.

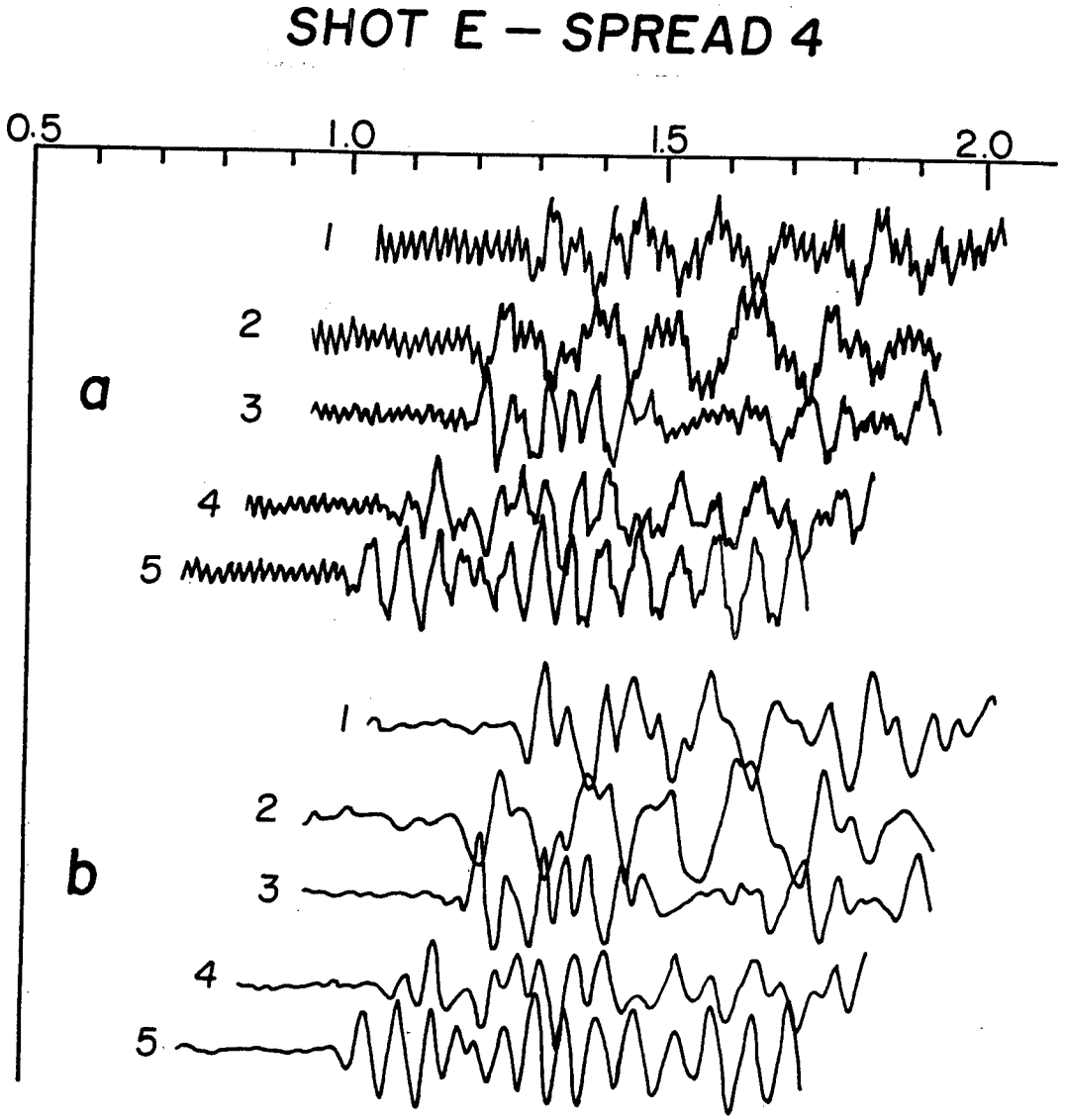

Figure 6. Five seismograms from spread 4, recording shot point E (a) traces 1 to 5 before filtering show high noise level (b) traces 1 to 5 after filtering with noise removed.

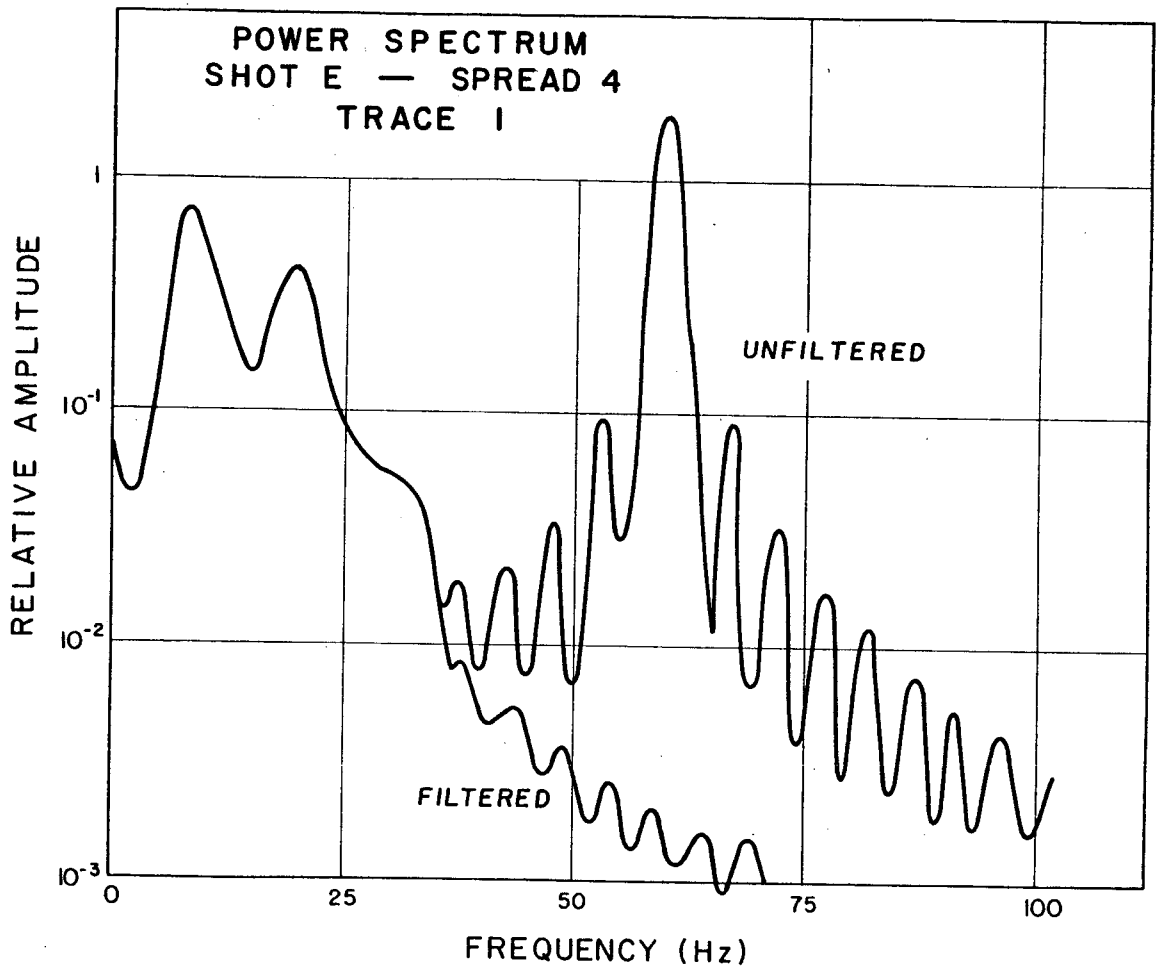

Figure 7. Power spectrum of unfiltered and filtered trace 1, spread 4, recording shot point E.

these adjustments is necessary to make interpretations of velocity gradients and anelasticity.

For the Roosevelt Hot Springs refraction profile, all data recorded from a shot point location were normalized to the spread containing the blast. Because the end geophones for adjacent spreads occupied the same location, normalization from spread to spread was relatively simple. Variations due to changes in source size or spread gains were compensated for by reducing or enhancing trace amplitudes until the amplitude was nearly identical to the proper trace. This adjustment was equivalent to recording all data using the entire profile with constant gain and a single shot.

Figure 8 demonstrates how this was done for shot point E, spreads 4 and 5. To facilitate comparison, the two traces were first plotted with their maximum value scaled to 1.3 cm. Amplitudes of several peaks and troughs of the first arriving energy were then measured. Since spread 4 contained shot point E, the spread was assigned a factor of 1. The factor for spread 5 was found by averaging the values necessary for adjusting a peak or trough on channel 1, spread 5 to be of equal value with its counterpart on channel 24, spread 4. The factor calculated for spread 5 was 0.14.

The frequency of phases used in attentuation studies lies in the 8-25 Hz range. By referring to the recording system's frequency response shown by Figure 3, it can be seen that for the range of frequencies desired in interpretation the response may be considered constant.

After all amplitude data were normalized, a comparison of

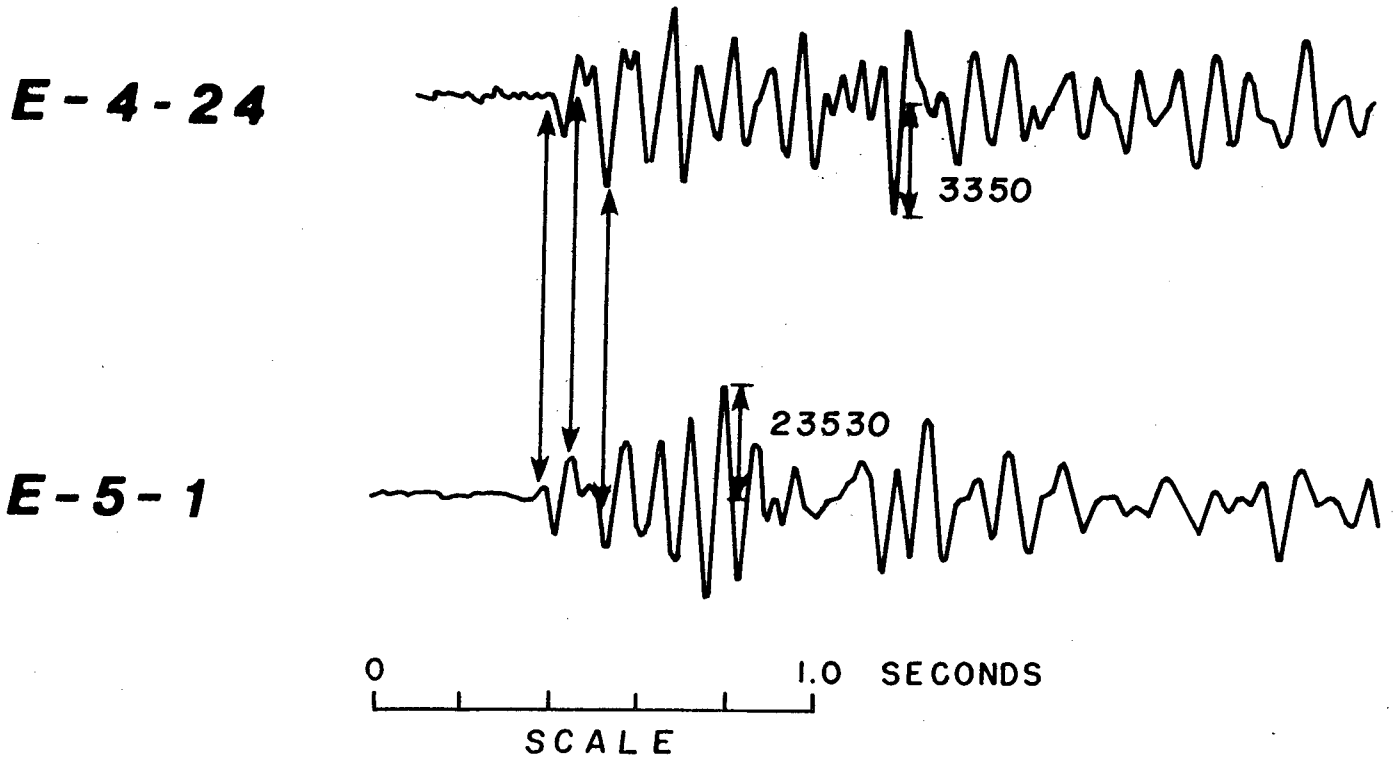

Figure 8. Normalization procedures for amplitudes on filtered spreads 4 and 5 recording shot point E. Number is the maximum zero to peak value that has been scaled to 1.3 cm. Arrows near first arrivals indicate the peaks and troughs which were measured and scaled to be equivalent in amplitude.

amplitude variations along the array then became possible. Since there were several recognizable phases, good station coverage along the line, and a high signal-to-noise ratio, these data allowed reasonable interpretations of attenuation.

CHAPTER 4

INTERPRETATION OF P-WAVE TRAVEL TIMES

Introduction

One of the primary reasons for any seismic exploration technique is the development of a structural model of the earth with velocities and thicknesses of major units. By determining travel-times of P-waves from refraction data, velocity-depth models can be theoretically generated to fit the observed data from which inferences about geology can be made.

Figure 9 is an example of reduced travel-time plots (reducing velocity = 6 km/s) used in the interpretation of the Roosevelt Hot Springs refraction data. The most useful P-wave information is contained in the first portion of each trace so that only 2 sec of each trace was plotted. With the exception of those seismograms having considerable noise, the first breaks can be clearly seen. A detailed discussion of the data is reserved for a later section. However, it would be useful to have a brief qualitative inspection here.

From shot points A, B, and C, there is a low velocity P-wave branch associated with the surface layer of the Milford Valley. This phase remains a first arrival to a much greater distance from shot point B than the same phase recorded from shot points A or C. A change in apparent velocity associated with a second velocity unit of

Figure 9. Profile coverage obtained during the refraction experiment. Two seconds of each seismogram plotted using a 6 km/s reducing time. Amplitudes scaled for optimum viewing. A, B, C, D, E, F, G are shot points. Surface geology: Qal, Quaternary alluvium; Qb, Quaternary basalt; Tg, Tertiary granite.

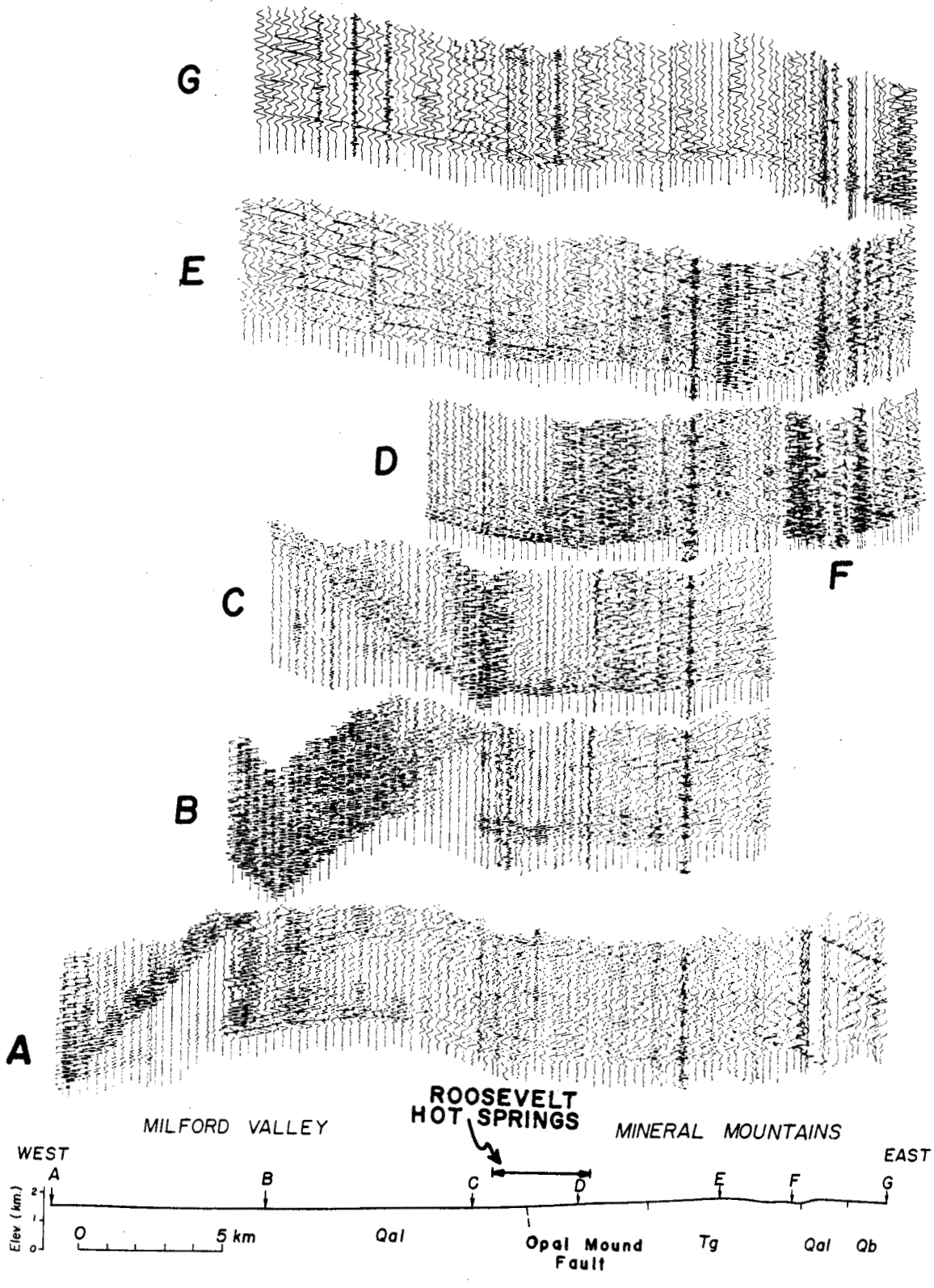
G
E
D
F
C
B
A
ROOSEVELT HOT SPRINGS
MILFORD VALLEY
MINERAL MOUNTAINS
WEST
EAST
A
B
C
D
E
F
G
Elev (km.)
2
1
0
0
5 km
Qal
Opal Mound Fault
Tg
Qal
Qb

the Milford Valley graben is clearly seen from shot points A and B.

For seismic waves propagating eastward from shot points A and B, a large increase in first-arrival apparent velocity occurs about midway between shots B and C. This phase, with an extremely high apparent velocity of 16 km/s, probably correlates with a deeper basement layer. Notice that reflected phases associated with the refraction branches are difficult to find.

The manner in which the first arrivals from shot points A and B change in apparent velocity from slow to fast to intermediate is an indication of a lateral variation in velocity. Whether or not this change is due to a change in basement dip and/or a lateral velocity change is a question that cannot be resolved by studying the record sections alone. Knowing the geology along the profile is most helpful in resolving this problem.

Geophones located in the Mineral Mountains, recording energy from shot points E, F, and G, do not appear to have recorded any phase other than the first P-wave arrival. Waves received in the Milford Valley from shot points E and G obviously have less high-frequency content than when the same geophones record energy received from shots within the valley.

Computer Analysis

Several techniques for the interpretation of seismic refraction data have been developed so that velocity-depth models may be generated from observed travel-times. The most commonly used method makes use of delay-times. First introduced by Gardner (1939),

delay-time analysis has been modified and improved by a number of workers. The computer program, SIPT., used in this study of the Roosevelt Hot Springs refraction line utilized a delay-time method described in Pakiser and Black (1957). An understanding of the general ideas behind delay-time analysis is essential before interpretation can begin. Much of the discussion is taken from Dobrin (1976).

Figure 10a is a simple cross-section for a two layer case and the travel-time versus distance plot of least-time ray paths. The refracted wave that has traveled along the velocity interface has taken a path of three legs, AB, BC, and CD. The total travel-time for this path is

$$T = \frac{x}{V_2} + \frac{2\ z\ \cos(i_c)}{V_1} \qquad (4)$$

On the time versus distance plot, this is the equation of the straight line which has a slope of $1/V_2$ and which intercepts the time axis ($x=0$) at the intercept time, $T_i = 2z \cos i_c/V_1$. The intercept time is the difference between the actual travel-time of a wave and the time that would be required if the wave traveled horizontally between the shot and receiver at the highest speed encountered along the refraction path.

For horizontal layering, the depth to the interface may be calculated from half the intercept time. Likewise, for inclined interfaces, the depth to the velocity contrast may be exactly determined by analytic means if intercept times exist for rays traveling up and down dip. However, in general, a refractor is

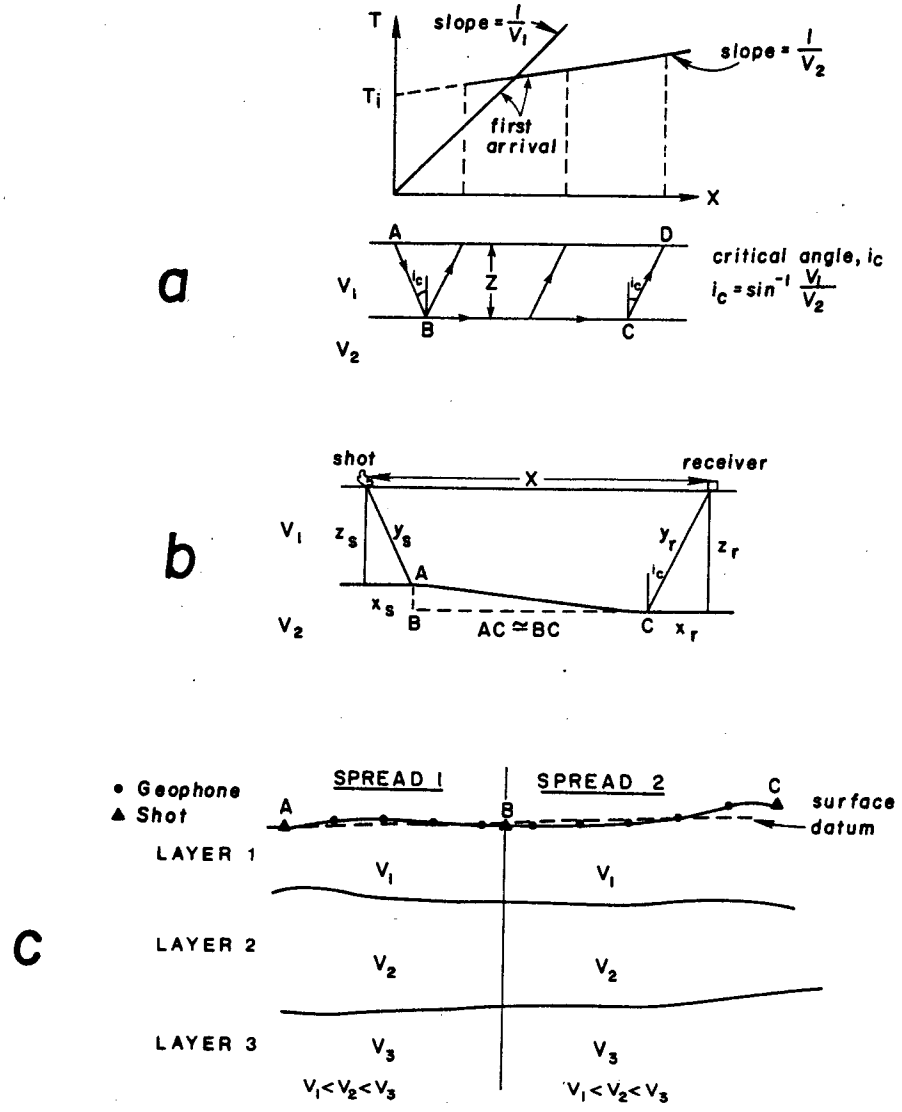

Figure 10. Diagrams showing nomenclature in delay-time analysis and in computer program SIPT, (a) ray paths of least time and time-distance curve for a horizontal interface (b) separation of intercept times into delay-times where depth under shot is different from depth under receiver (c) assumptions in SIPT: layer velocities increase with depth; datum is least-squares line through geophones.

neither horizontal nor uniformly dipping. Since depths determined from intercept times represent the sum of the respective depths to the horizon beneath the shot and the receiver, special techniques were developed to separate the depths at the two ends.

Delay-time methods are convenient for carrying out this separation and Figure 10b illustrates this point. The intercept time $T-x/V_2$ is made up of two "delay-times": D_s, associated with the shot end of the profile, and D_r, associated with the receiver end. Nearly all of the intercept time is associated with the slant paths, y_s and y_r. The travel-time for a ray is

$$T = \frac{x}{V_2} + D_s + D_r = \frac{x}{V_2} + \left(\frac{y_s}{V_1} - \frac{x_s}{V_2}\right) + \left(\frac{y_r}{V_1} - \frac{x_r}{V_2}\right)$$

$$= \frac{x}{V_2} + \frac{z_s \cos(i_c)}{V_1} + \frac{z_r \cos(i_c)}{V_2} \qquad (5)$$

the latter two terms are the delay-times for the shot point and receiver respectively. Thus it is seen that if the intercept time can be separated into component delay-times the depths at each end of the profile can be calculated. Indirect means of separation are necessary since delay-times are never measured directly.

The sum of the delay-times for the shot and any detector can be determined by subtracting x/V_2 from the arrival times. Since for any given spread the delay-time due to the shot point remains constant, the variations in delay-times are assumed to be due to variations in depths to the refractor beneath the receivers. The depth variation between any two receivers is

$$\Delta z_r = \Delta t_r \, V_2/\cos(i_c) \qquad (6)$$

where Δt_r is the difference in delay times between the two receivers. The depth point is not directly below the receiver, but is migrated toward the shot point by

$$\Delta x = x_r = z_r \tan(i_c) \qquad (7)$$

Thus, it is possible to calculate the depth variations from the total delay-time for each receiver position. If the depth at any point is known, such as from a drill hole or calculated by refraction equations where the refractor is a plane surface, the depth to the refractor can be found by adding or subtracting the appropriate depth variation.

There are other relationships that also apply. When the shot and receiver are interchanged, as for opposite ends of a reversed spread, the total delay-time is equal since identical paths are reciprocal. Also, if the total delay-time is known for two shots arriving at a given receiver then the difference in depth between the two shot points can be calculated.

All of the above relationships have neglected dip. However, for dips of less than 10°, the error is negligible and the error resulting from dips up to 25° is not serious considering the uncertainties from other sources of error.

Before delay-time analysis or any mathematical procedure is applied to refraction data the number of layers represented by the refracted arrivals and the layer from which an identified phase has been refracted must be known. Referring to Figure 10a, the travel-time segment through the origin is associated with the layer having a velocity of V_1. The second segment has been identified as a

refractor from the layer with a velocity of V_2.

To understand how the computer program, SIPT., computes the velocity-depth models it is necessary to follow the way that the input data are handled. The remainder of this section is a review of program procedures described in Scott et al. (1972) and Scott (1977).

SIPT requires several simplifying assumptions in its operation (see Figure 10c). Layer boundaries are represented by a series of straight line segments connected end-to-end beneath geophones and extending across the entire model. This requirement presents difficulties when modeling the Roosevelt Hot Springs data since layers in the Milford Valley are not continuous onto the Mineral Mountains.

It is assumed that the vertical velocity increases with layer depth and each layer of each spread has a constant horizontal velocity along its upper surface. In multispread modeling, different horizontal and vertical velocities may be assigned to the layers in each spread. This is essential when lateral velocity variations occur.

When all data are input, the velocity, V_1, of layer 1 is calculated to be the average of velocity found for rays that follow direct paths from shot points to geophones. Then, a least-squares line is fit through the geophone elevation points to serve as a datum. The user, if he so desires, may specify a datum of his own. A horizontal datum was not used in correcting travel times for the interpretation of data for two reasons. First, elevation differences along the refraction profile would cause large time and distance corrections. Second, and more importantly, the assumption that the

top of the second velocity layer is below the datum elevation would be a gross error. An elevation of 1500 meters is required for a datum to be below all geophone and shot locations. This in turn dictates a 600 m thick surface layer in the Mineral Mountains that is thought to be unreasonable. (See the elevation profile in Microgeophysics, 1977).

Datum corrections are computed and applied to the refraction travel times by simply dividing V_1 into the elevation difference between each geophone or shot and its corresponding point on the datum line. This is sufficient for removing first-order errors. Later, when the velocity, V_2, of layer 2 is calculated, datum corrections are recomputed using the slant directions of the actual raypaths.

The next step in processing refraction data is to determine the velocity of layer 2. SIPT uses two procedures. The first method is equivalent to determining the velocity by taking the inverse slope of a line through arrivals on a time-distance graph. The second method is a least-squares procedure that minimizes the variation of total delay-time differences (Scott et al., 1972). Called the Hobson-Overton method after its developers, it requires that at least two geophones receive refracted rays traveling in opposite directions from two different shot points. The formula used is:

$$V = \frac{\Sigma \Delta x_i^2 - (\Sigma \Delta x_i)^2/n}{\Sigma(\Delta x_i)(\Delta t_i) - (\Sigma \Delta x_i)(\Sigma \Delta t_i)/n} \qquad (8)$$

where V is the desired refraction velocity, Δt_i is the time difference between arrival times at geophone i from shot points on opposite ends of the spread, Δx_i is the corresponding difference between distances to geophones from the shot points, and n is the total number of

geophones used. The average difference in delay-times at the two shot points, the measure of the error of fit at each geophone, and the standard error of the group of geophones are computed along with the refraction velocity determined. Of the two techniques used, the latter method was found to give the best results.

Since V_1 and V_2 are now known, the datum corrections are recomputed using the slant direction of the ray paths. Then, the point of entry of rays entering the refracting horizon is computed from the half-intercept time, and the points of emergence of each ray are located from the delay-time associated with each geophone. A straight line is fit to the points of entry and exit to obtain an estimate of the average dip of layer 2.

The delay-time delineation of the velocity interface is improved by one pass of a ray-tracing procedure. Adjustments in depth and location of the interface is accomplished in the following manner. The first step is to compute the travel-time for a ray reaching each geophone. Half of the difference between the computed time and observed time is allotted to the ray path emerging upward toward the geophone. The average of the remaining error for all geophones is allotted to the ray path extending from the shot to the refracting horizon. The position of the layer is adjusted accordingly and the times for rays traveling in the surface layer are subtracted from the observed travel-times. This removes the effect of layer 1.

Next, the velocity of deeper layers is determined by averaging the velocities found using both the inverse slope and the Hobson-Overton techniques. After all velocities are calculated the

interface for each successive layer is delineated, first by the delay-time method, and second, by improvements from a three-pass ray-tracing procedure. The delay-time method is similar to that described previously, except that for horizons beneath layer 2, the times of ray path segments in overlying layers are subtracted from the observed travel-times. These times are determined by tracing rays upward to shot points and geophones. The delay-time calculations provide points of ray entry and emergence which are used in defining the top of the layer being delineated. Rays are traced upward through all layers between the refracting layer and the shot points and geophones. The computed times are then compared to the observed travel-times with improvements being made as before.

On the second pass of the ray-tracing procedure, the initial ray segment directions are found by using the actual dip at the point of interest on the smoothed model interface. The results are examined to detect the possible alignment of kinkiness beneath layer 2 which would suggest that errors exist in the delineation of layer 2.

After layer 2 is repositioned, the locations of all deeper layers are recomputed by the last pass of the ray-tracing and adjustment method. This completes the analysis by SIPT. The last execution of the program is to print out the velocity-depth model that has been computed. Tables are also printed that evaluate how well the times computed from the model fit the observed first arrival times.

Velocity Modeling Procedure

To construct a velocity model from the seismic refraction data,

first arrival times of P-waves were determined for all possible traces. These times were utilized in the analysis not only because of the ease of time determination but also for use with available computer routines. The determination of first P-wave arrival times used the unfiltered refraction data since these were the real and unaltered seismograms. However, first arrivals were obscured on the unfiltered traces which contained the 60 Hz noise (Figure 5). Therefore, for these seismograms, the filtered data were used. Second arrivals yielded additional structural and velocity information, but their arrival times were not used in the computer analysis of layering.

After data were input into the refraction modeling program, the apparent velocities for the various legs of the travel-time curve were determined using the two techniques described previously, the inverse slope method, and the Hobson-Overton least-squares approach. The program would then calculate a velocity-depth model using a layer velocity that was an average of the velocities found by the two methods for a single layer, or, if the user desired, using a velocity specified by the user.

The procedure for determining a velocity-depth model began using the first P-wave arrival times from two shot points of a reversed spread. For these purposes, a spread is defined to be the group of geophones located between two shot points. After the resulting model was inspected for the fit of computed travel-times to observed travel-times, additional data from shots located beyond the ends of the geophone spread were included in the computation and another

iteration was made. By using the multiple subsurface coverage of our data the best model from observed travel-times was calculated.

When working with only one spread, the computer program was allowed to change the interpretation of layer depth and dip that best fit the first arrival times. Since the velocity interfaces must be continuous in multi-spread interpretations, the next step was to combine adjacent spread data so that the interpretations of subsurface layer positions changed together.

In the Mineral Mountains, a plot of time versus distance data indicated an increasing apparent velocity with distance, especially for stations within one km of the source. This was a characteristic of a continuous increase in velocity with depth. To determine velocity information from refracton data in areas with positive velocity gradients, the Herglotz-Wiechert inversion method was applied.

Figure 11 is a diagram of paths taken by seismic waves when velocity increases with depth and the time versus distance curve that results. Any ray path from the shot that obeys Snell's Law will return to the surface at a distance x, given by

$$x = 2p(z_m) \int_0^{z_m} \frac{V(\varsigma)d\varsigma}{\sqrt{1-p^2(z_m)V^2(\varsigma)}} \qquad (9)$$

where z_m is the maximum depth of penetration of the ray, $p(z_m) = \sin i/V(z_m)$, $V(z_m)$ is the velocity and ς is the variable of integration. After a change of variables, substitutions, and integration, equation (9) becomes

$$z(p_m) = \frac{1}{\pi} \int_0^{x_m} \cosh^{-1} \frac{p(x)}{p_m} \, dx \qquad (10)$$

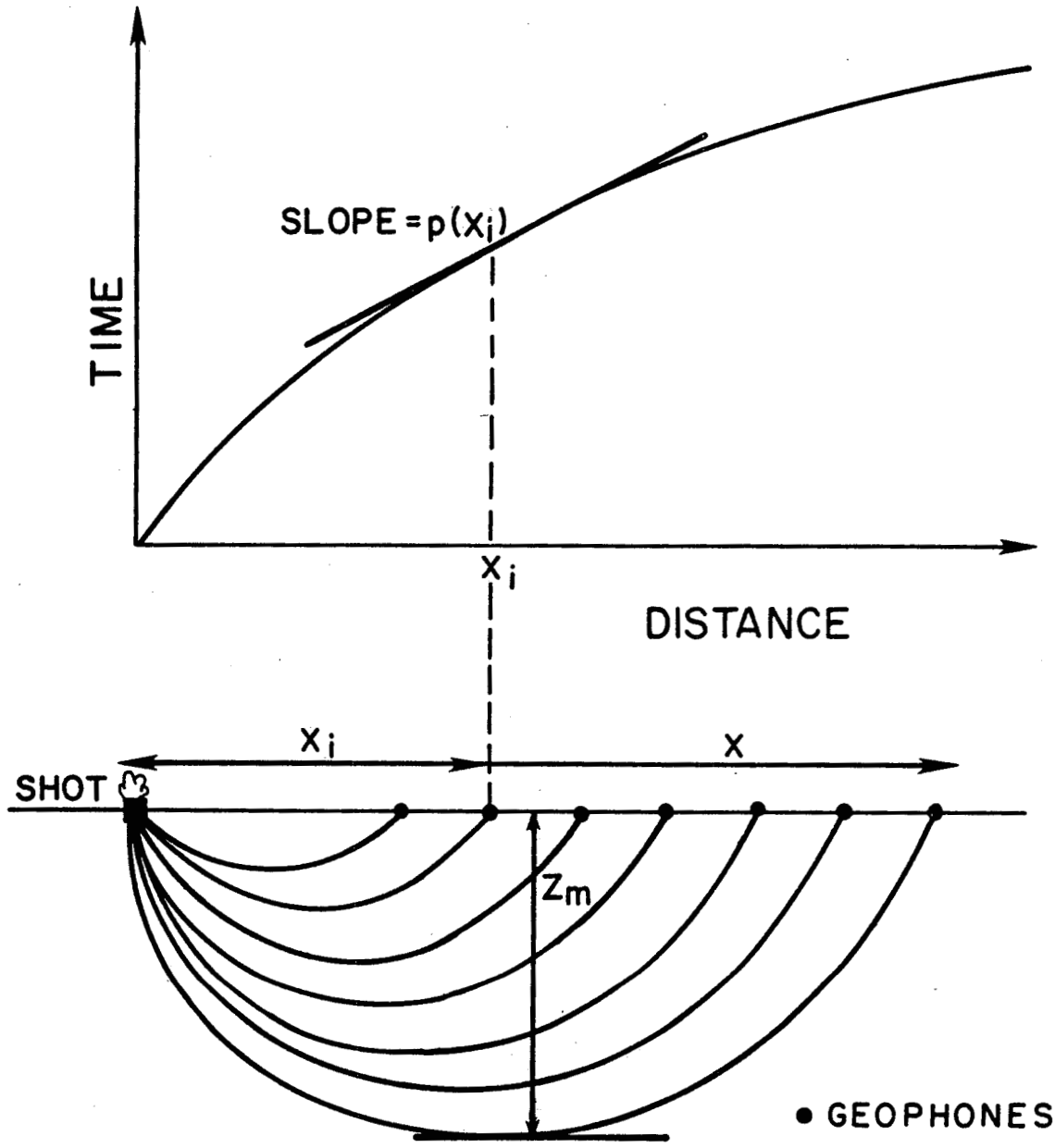

Figure 11. Ray paths and time-distance curve for velocity linearly increasing with depth. Apparent velocity at any distance x is found from the slope of the curve. z_m is the maximum depth of penetration for a given ray.

Let p_m be the parameter of the ray path whose maximum penetration is z_m. Since $(\partial t/\partial x)_z = p$, $p(x)$ is given by the slope of the time-distance graph. Also, since $\sin(i)/V = p$, the velocity at depth $z = 1/p_m$, since at this point $i = 90°$. By substituting, equation (10) becomes

$$z(V) = \frac{1}{\pi} \int_o^x \cosh^{-1}\left(V\frac{dt}{dx}\right)\, dx \qquad (11)$$

This is now in a form suitable for the direct computation of z as a function of V. Equation (11) is the Herglotz-Wiechert integral for a flat-layered model. The Appendix contains a listing of the computer program, HWINV.MAIN, which solves the Herglotz-Wiechert integral. This routine, written by R. B. Smith, requires the input of apparent velocities at different distances.

Examination of Record Sections

Figure 12 is a schematic diagram showing the layer and P-wave designations for specific arrivals interpreted in this study. These labels will be referred to in the remainder of this report.

Four seconds of each trace from the Roosevelt Hot Springs seismic refraction experiment are shown in Figures 13-19. All traces are corrected for normalized amplitudes but have been multiplied by a factor relating to their distance, x(km), from the shot. This method of display enables one to analyze the relative amplitude decay. However, those trace amplitudes within one kilometer of the energy source have been reduced considerably by this factor. From seismograms associated with shot point A, the factor is x^3, and for

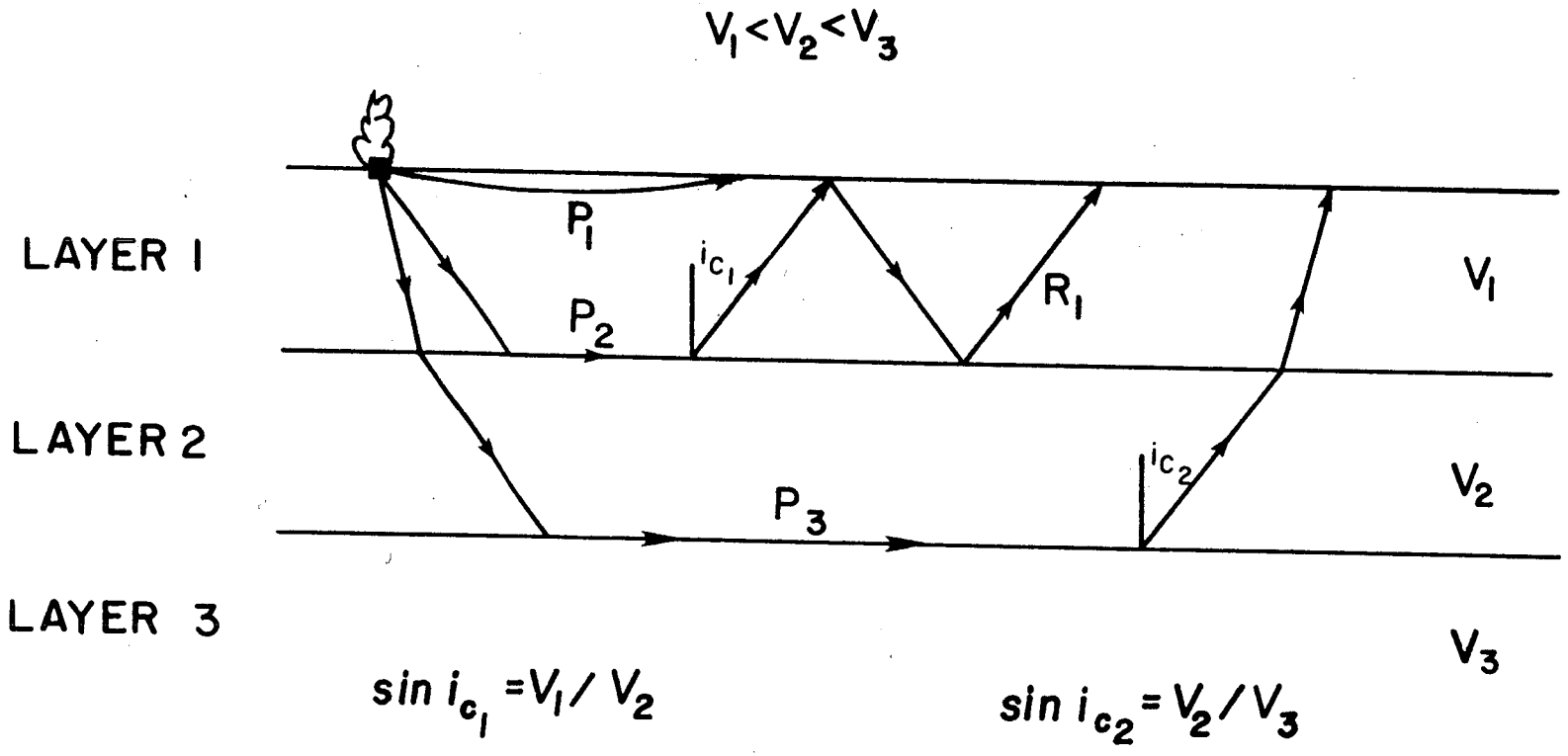

Figure 12. Illustration of labels used in phase identification: P_1, the direct wave; P_2, refracted wave from top of layer 2; P_3, refracted wave from top of layer 3; R_1, reflected wave in layer 1.

all other shot points, $x^{3/2}$. The distance scale on all plots is kilometers from shot point A.

The time scale was reduced at 6 km/s and no travel-time corrections were made for the elevation change across the profile. Datum corrections were not necessary since they were included in the modeling program, SIPT, and also since the variation in ray path length was taken into account by the ray-tracing procedure. (See the Computer Analysis section of this chapter.)

The seismograms generated by the explosion at shot point A located on the western side of the Milford Valley are shown in Figure 13. Clearly evident to a distance of at least 12 km is the direct wave, P_1, traveling at a velocity of 1.9 km/s through the unconsolidated valley alluvium.

A head wave, identified as P_2, becomes a first arrival at 0.5 km from shot point A. This implies a relatively shallow, higher velocity layer due to the small crossover distance. The presence of bedrock at the surface approximately one km to the west demonstrates the possibility of a shallow layer with a velocity greater than the alluvium. Due to the dip of the interface, the apparent velocity of P_2 increases toward the east. Near 9 km the apparent velocity becomes 5 km/s.

Because of the constant velocity of P_1 and the changes in apparent velocity of P_2, the possibility that P_1 is a misinterpreted refracted S-wave phase is remote. For example, if we assume that P_1 is an S-wave, the ratio V_p/V_s =1.8 is nearly constant to a distance of 7 km from shot point A. Then, it increases to 1.9 at 9 km and at 12

km V_p/V_s = 2.1. Where V_p/V_s would be established (between 2 and 5 km), the resulting Poisson's ratio of 0.28 would suggest an S-phase that arrived nearly one second before the arrival of P_1 at 10 km. Therefore, the identification of P_1 as a P-wave is justified.

At 11 km from shot point A, energy refracted along the top of a high-velocity interface becomes the first arrival identified as P_3. An apparent velocity of 17 km/s for this phase yields information about the attitude of the upper-surface of layer 3. Since velocities exceeding 7 km/s are unrealistic velocities for rocks in the upper 1 to 2 km of alluvium filled valleys, the interface is suggested to have a dip of 20° to the west. Near 16 km, the apparent velocity of P_3 decreases to 6 km/s.

Distinguishing between P_2 and P_3 was difficult since their first waveforms were very similar. These phases were initially interpreted as energy refracted along a single interface because the change in apparent velocity could be accounted for by changes in dip of the layer 2-layer 3 interface. However, upon plotting the first arrival amplitudes versus distance, two distinct phases were identified on the basis of the presence of a drop in amplitude by a factor of 10 occurring at about 11 km. This point will be discussed in chapter 5.

The later arrivals, R_1, and R_2, are interpreted as refracted-reflections. The arrival times for R_1 correspond closely to times for head wave energy from layer 2 reflecting off the surface of layer 1 and returning to layer 2 at the critical angle to again become a head wave.

Even though the primary goal of the experiment was concerned with refraction interpretation, associated reflections should be evident in the seismic record sections. Inspection, however, of the data revealed the absence of clearly identifiable reflections. One explanation for the absence of the reflections was that the dips of layers 2 and 3 were too excessive for the reflection of large amounts of energy back to the surface. Another explanation might be severe scattering effects from inhomogeneities in the bedrock beneath the alluvium. An attempt to find near vertical reflections will be discussed at the end of this section.

Seismograms recorded from shot point B show P_1, the direct wave, evident to a distance of at least 14 km although it remains the first arrival to only 10 km (Figure 14). Because shot point B is located near the center of the Milford Valley and probably near the position of maximum alluvial thickness, it seems reasonable to receive direct waves to larger distances before the first refracted waves from deeper layers become first arrivals. The crossover distance for shot point B is 3 km compared with only 0.5 km for shot point A. The first arrivals from deeper layers appear near 10 km as the P_2 refracted arrivals with velocities of 3.0 km/s. In the valley layer 2 is identified from this phase.

At distances greater than 12 km, P_3, the high apparent velocity phase refracted along the top of layer 3, is the first arrival. A comparison of data from shot points A and B shows evidence for P_3 being refracted along the same layer in both record sections. Notice that the apparent velocities are nearly equal, and, more importantly,

when an increase or decrease in apparent velocity occurs on spreads recording shot point A, the same velocity change occurs at the same geophone locations recording shot point B.

The lack of identifiable reflected phases on this record section possibly lies in the recording process. The data from shot point B suffered severely from the high gain levels of the recording instruments. If reflected phases have the same dominant spectral frequency as other phases present, the only possibility of detecting them is from discrimination by their amplitudes. Clipped records will mask evidence for phase changes in amplitude variations. On the other hand, different phases with equal amplitudes are distinguishable only if their frequencies are unequal.

Shotpoint C is near the eastern margin of the Milford Valley approximately 1.4 km west of the Opal Mound Fault. Figure 15 shows the high amplitude direct wave, P_1, recorded from geophones spread west from shot point C. The apparent velocity of 1.9 km/s is near that of other P_1 phases, from shot points A and B.

On the second, third, and fourth geophones west of C, P_2 is the first arrival. The apparent velocity of P_2 is much lower than P_2 seen from shots A and B. At distances less than 13.5 km the first break correlates with P_3, the event refracted along the top of the basement interface. This shot was not recorded at distances large enough to see changes in the apparent velocity of P_3. To the west of shot point C low velocity long-period surface waves are also noted.

To the east of shot point C, several differences in the first arrivals are evident. There are no longer two or three distinct

phases present as in the data recorded across the valley. In fact, the only phase appearing clearly is the first arrival. The apparent velocity of P_3 across the spreads toward the east varies slightly but remains close to 6 km/s. Only the first geophone east of shot point C records P_1. It is inferred from these observations that the alluvium cover above the basement to the east is very shallow. The geologic map (Figure 1) of the Mineral Mountains area confirms this. At approximately 6 km east of C, the alluvium pinches out and granite is exposed at the surface east of this point.

Shot point D was fired in alluvium (Figure 16). The absence of P_1 as first arrivals was again evidence for a thin alluvium fill to the east and west of the source. Layer 2 identified in the Milford Valley was not present. The P_3 phase had an apparent velocity near 6 km/s, and the only second arrivals in the record section were surface wave propagations toward the valley.

The seismograms recorded from shot point E are shown in Figure 17. For seismic waves arriving at geophones between shot points D and E and between shot points E and G, an apparent velocity of just over 4 km/s is indicated. This is a remarkably low velocity for known granites. Waves propagating to the west and arriving between shot points C and D show an increase in apparent velocity to about 6 km/s while waves arriving west of shot point C show a decrease in velocity to just over 4 km/s. One explanation for the low velocities, suggested by waves arriving west of shot point C, is that the waves have traveled a significant portion of their ray path within the low velocity layers of the Milford Valley.

Note that for seismograms east of shot point E, the amplitudes of the traces have been attenuated much more than the amplitudes for those traces an equal distance to the west of shot point E. Since the refraction profile in the Mineral Mountains nearly coincides with the Hot Springs fault the low granite velocity and high attenuation may be related to propagation through the fracture zone.

The data obtained from shot point F (Figure 18) exhibit an apparent velocity of about 5 km/s for waves propagating north from the source and an average apparent velocity of less than 4 km/s for waves propagating east. The shot was not recorded on any other spread and therefore not much additional information may be extracted from the section.

Figure 19 is a display of the traces that have been recorded from shot point G. A scaling factor was necessary in plotting to prevent the trace amplitudes near 21 km from being plotted off scale. The cause of the amplitude increase is discussed in the following section. A surface velocity of 2.8 km/s for basalt was determined from the direct wave recorded as the first arrival to distances of 1.5 km from the source. Beyond this distance an apparent velocity of approximately 4 km/s was found from the seismic waves propagating as far as shot point E.

Near 24 km an abrupt increase in first arrival velocity to greater than 6 km/s occurs. This apparent velocity is constant for at least 5 km until the observed velocity again decreases to nearly 4 km/s. Again, the decrease to a lower apparent velocity may be due to effects of the low velocity layers in the Milford Valley.

To increase the possibility of identifying reflections (if they exist) in the refraction data, all of the digitized data were plotted in an unfiltered mode. After examination of the records, four sections were chosen that represent the data for the range of different geologic conditions encountered at the Roosevelt KGRA (Figures 20-23). Twelve seconds of data are shown. This should be adequate to observe reflections from depths less than 20 km. Amplitudes have been scaled to equalize each trace's maximum value.

Shot point A, spread 1 (Figure 20) was chosen to search for reflections from the Milford Valley basement. However, other than long-period surface waves and the refracted phases previously identified, no additional phases are identifiable. As mentioned earlier, the absence of reflections may be due to the excessive dip of subsurface layers.

Figures 21 and 22 show the 12-second records within the KGRA (spread 3) from shot points C and D, respectively. Air waves moving at 350 m/s and the first arrivals are clearly seen. These spreads are located above a shallow basement and a large shallow velocity contrast inferred from the refraction data, yet no reflections are evident. Also, the spreads are within the geothermal area but no direct seismic evidence for the heat source or reservoir was noted. One explanation for the non-existence of identifiable reflected phases from a shallow interface is explored in the following Interpretation section.

From shot point E, spread 4 (Figure 23) the refracted arrivals are the only identifiable phases seen in the traces. No reflections from beneath the Mineral Mountains is found.

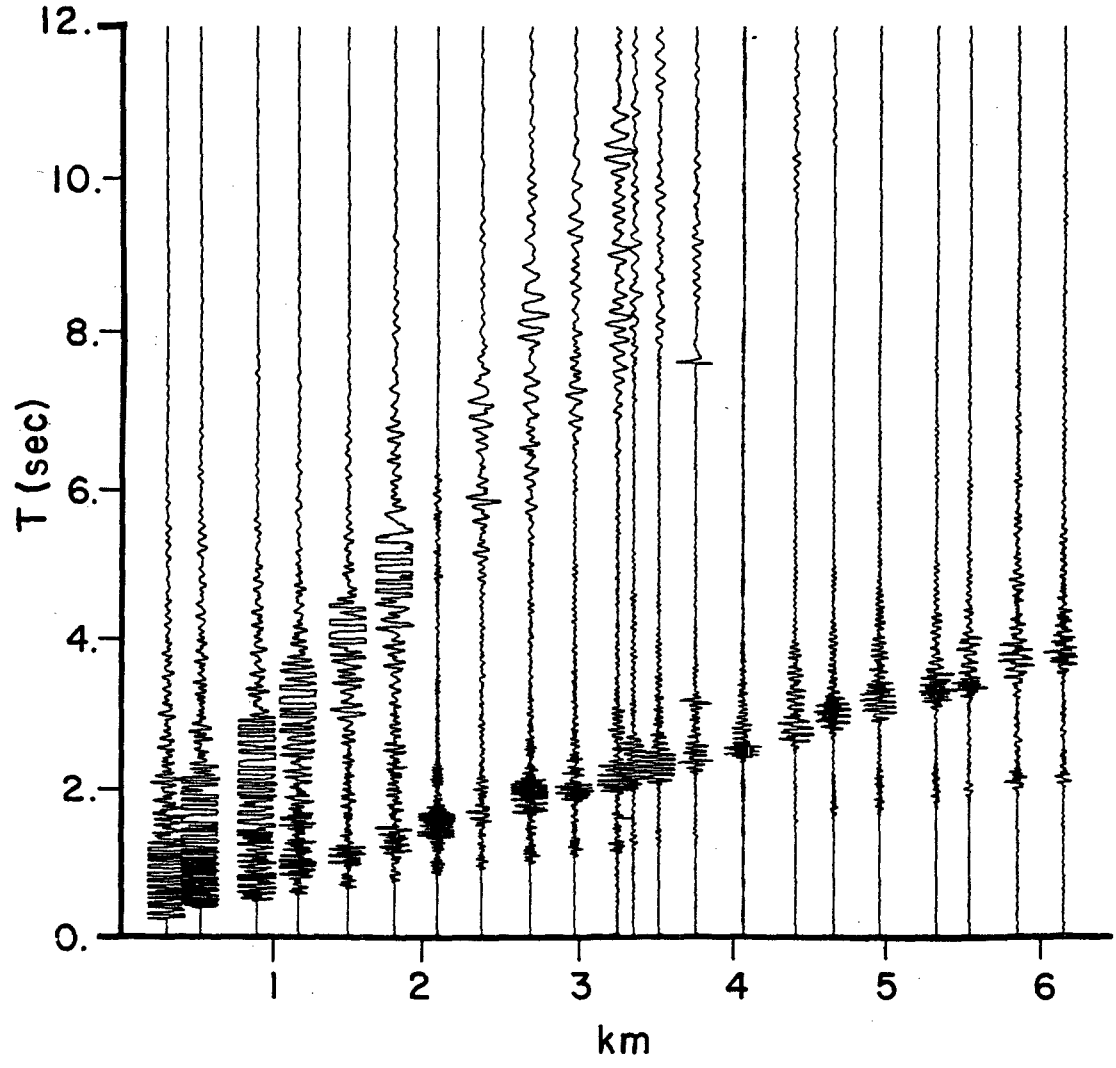

Figure 20. Shot point A, spread 1 seismograms. Maximum value of all traces is scaled to be equivalent to each other.

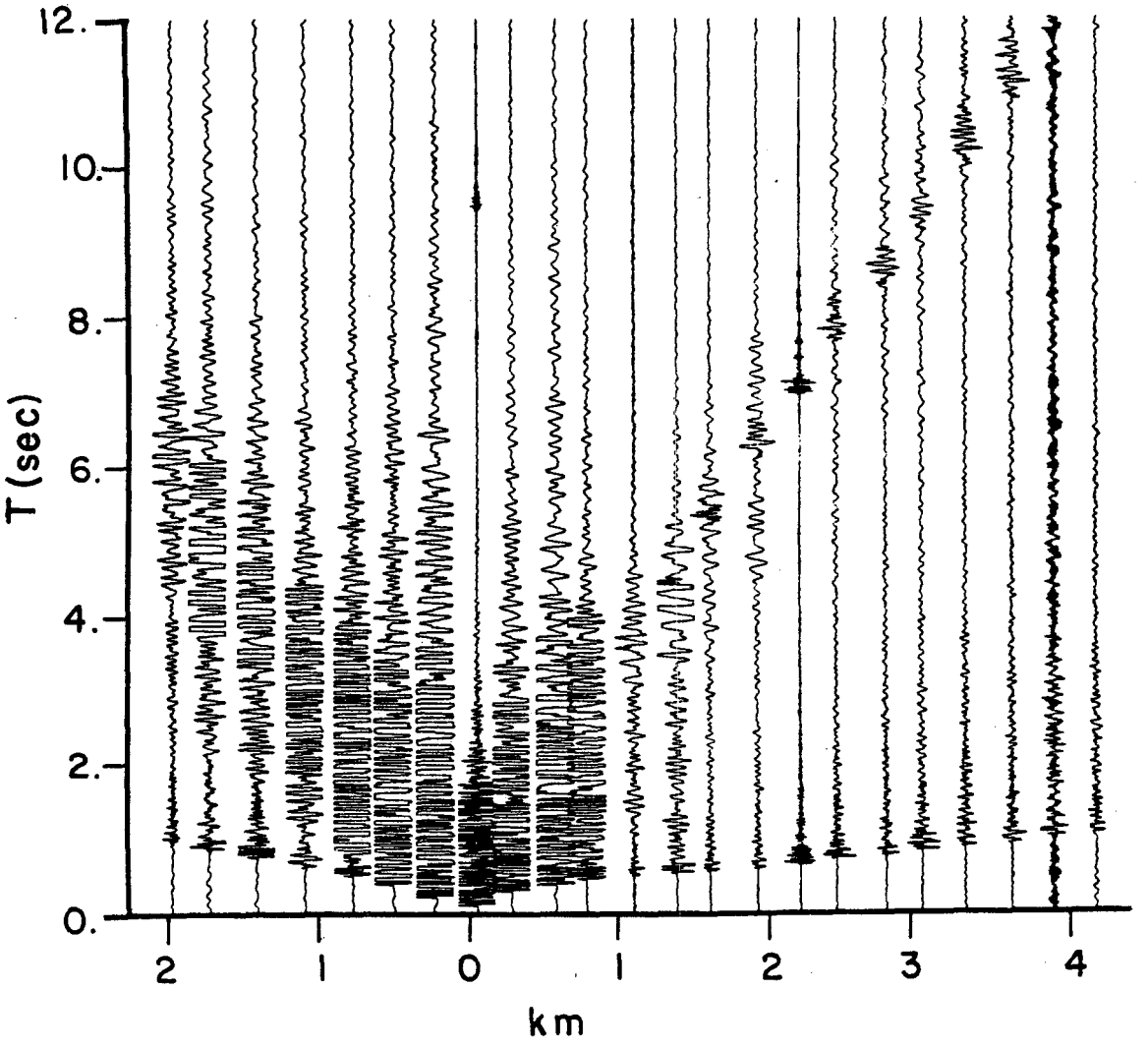

Figure 21. Shot point C, spread 3 seismograms.

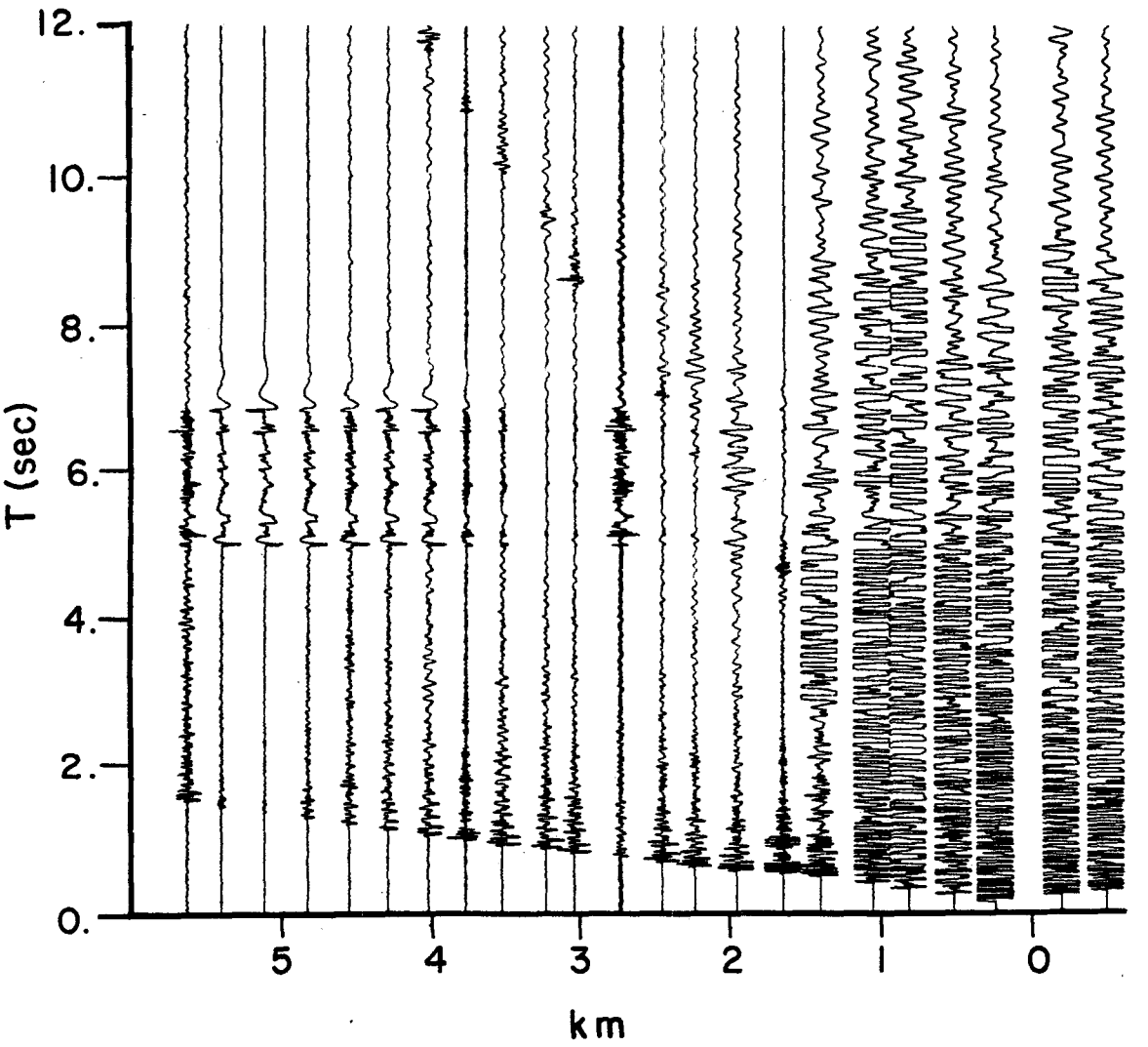

Figure 22. Shot point D, spread 3 seismograms.

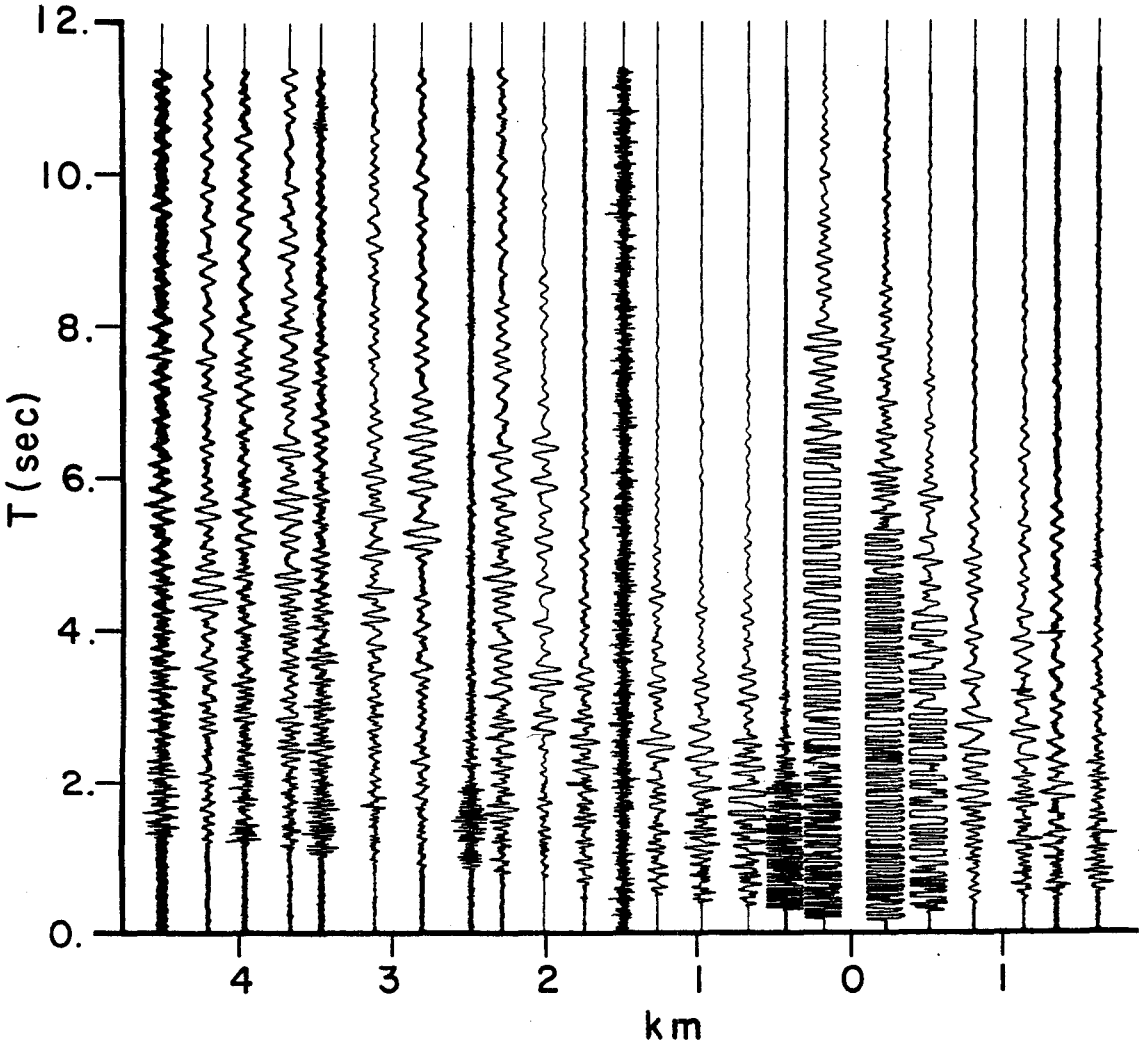

Figure 23. Shot point E, spread 4 seismograms.

Interpretation

The correlation of travel-time branches associated with the same layer and their apparent velocities is important before beginning interpretation. Figure 24 is a plot of first P-wave arrival times versus distance for the Roosevelt Hot Springs refraction profile. A series of straight line segments were fitted by least-squares to the travel-times and the corresponding velocities for each of these segments are included in Figure 24. The refraction branches from a shot point could have been subdivided into shorter more detailed apparent velocity segments, but because of scatter due to site response and time picking error the identification of additional segments was not justified. Therefore, the lines in Figure 24 are not directly comparable to the lines in Figures 13-19.

On the eastern flank of the Milford Valley and through the Mineral Mountains, the refraction line deviated from a straight line by up to 2 km. This implied that subsurface ray paths were not necessarily identical for reversed spreads. Also, the dips of velocity interfaces may have deviated from the plane of the profile. These limitations must be kept in mind, though I do not believe they introduced significant errors in the interpretation since the refraction profile generally ran perpendicular to the strike of most surface geologic features except the Hot Springs fault. In addition, to minimize error caused by deviations of the profile, coordinates for shot points and geophones were referenced to a straight line passing through the end points of the spread being modeled.

The velocity-depth model derived from the travel-time data for

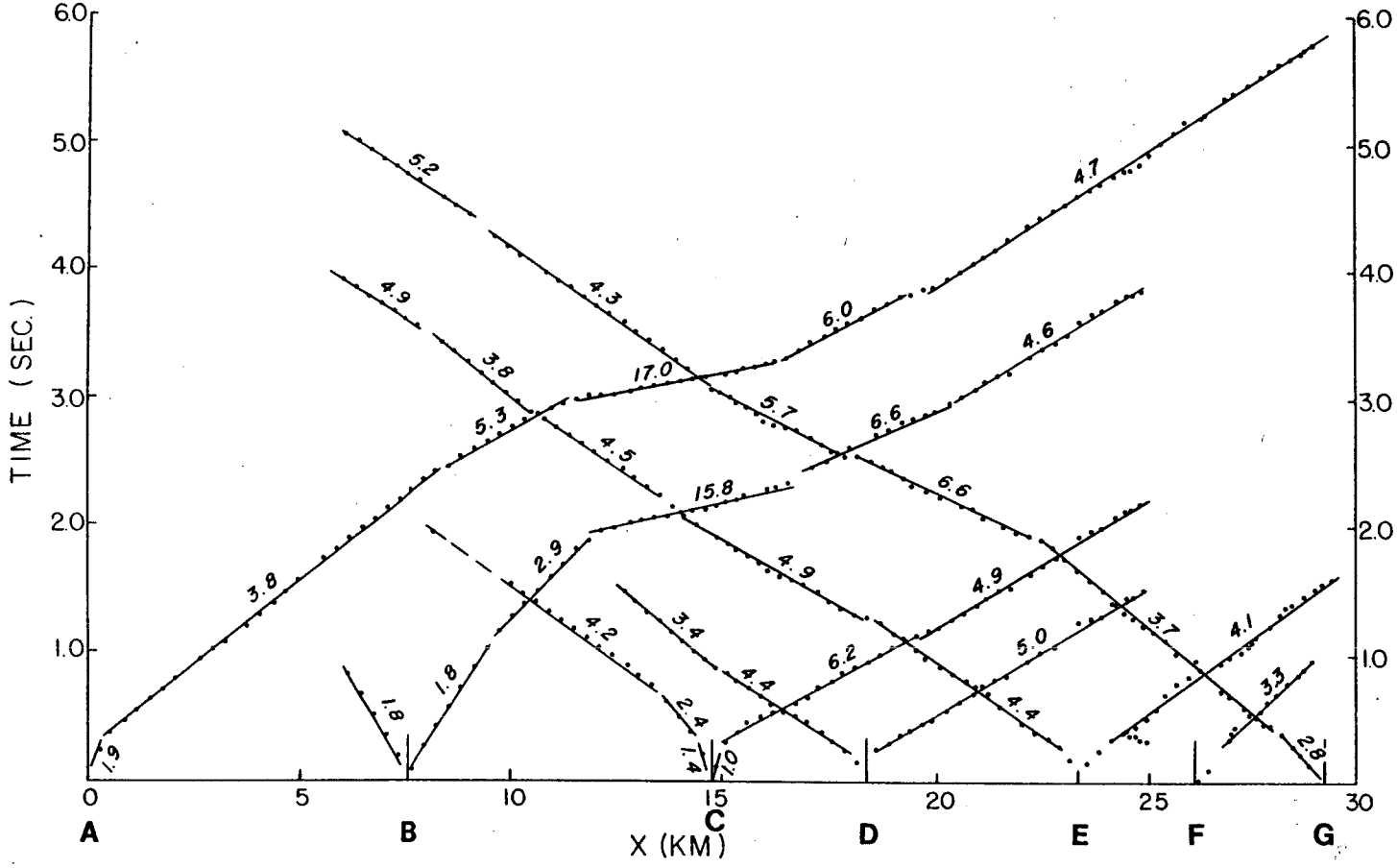

Figure 24. Travel-time plot of first arrivals. Apparent velocities shown for selected travel-time branches. Letters indicate shot point locations.

all shot points of the refraction profile is shown in Figure 25. Three velocity units were used to describe the general subsurface structure of the Milford Valley: 1) layer 1, a surficial layer with a velocity of 1.8 km/s; 2) layer 2, an intermediate horizon with a velocity of 4.0 km/s; and, 3) layer 3, a basement layer with a velocity of 6.7 km/s. The geophone spread between shot points A and B did not record waves propagating to the west and, therefore, the true dip, and velocity of subsurface layers could not be calculated with as much certainty compared with the rest of the profile.

Layer 1 is defined by direct waves from shot points A, B, and C, that are recorded as first arrivals out to 2 km from shot point B and less than 1 km for both shot points A and C. This indicates a thicker surficial layer beneath shot point B in the center of the valley than beneath shot points A or C located near the margins.

Surface geologic investigations and drill hole data show that layer 1 is mainly composed of Quaternary age gravels, sands, and clays, most of which were deposited when ancient Lake Bonneville covered the present Milford Valley. Additional layer 1 sediments were deposited as alluvial fans after Lake Bonneville receded.

The interface between layer 1 and layer 2 is delineated by first arrivals of P_2 from shot points A, B, and C. Seismic waves originating from shot point A, which are refracted along the top of layer 2, reach the surface as first arrivals to distances of 11.0 km. Similarly, waves arriving between 9.5 and 12.0 km, that originated at shot point B, have also propagated along layer 2. The only waves recorded from the interface between layer 1 and layer 2 are for three

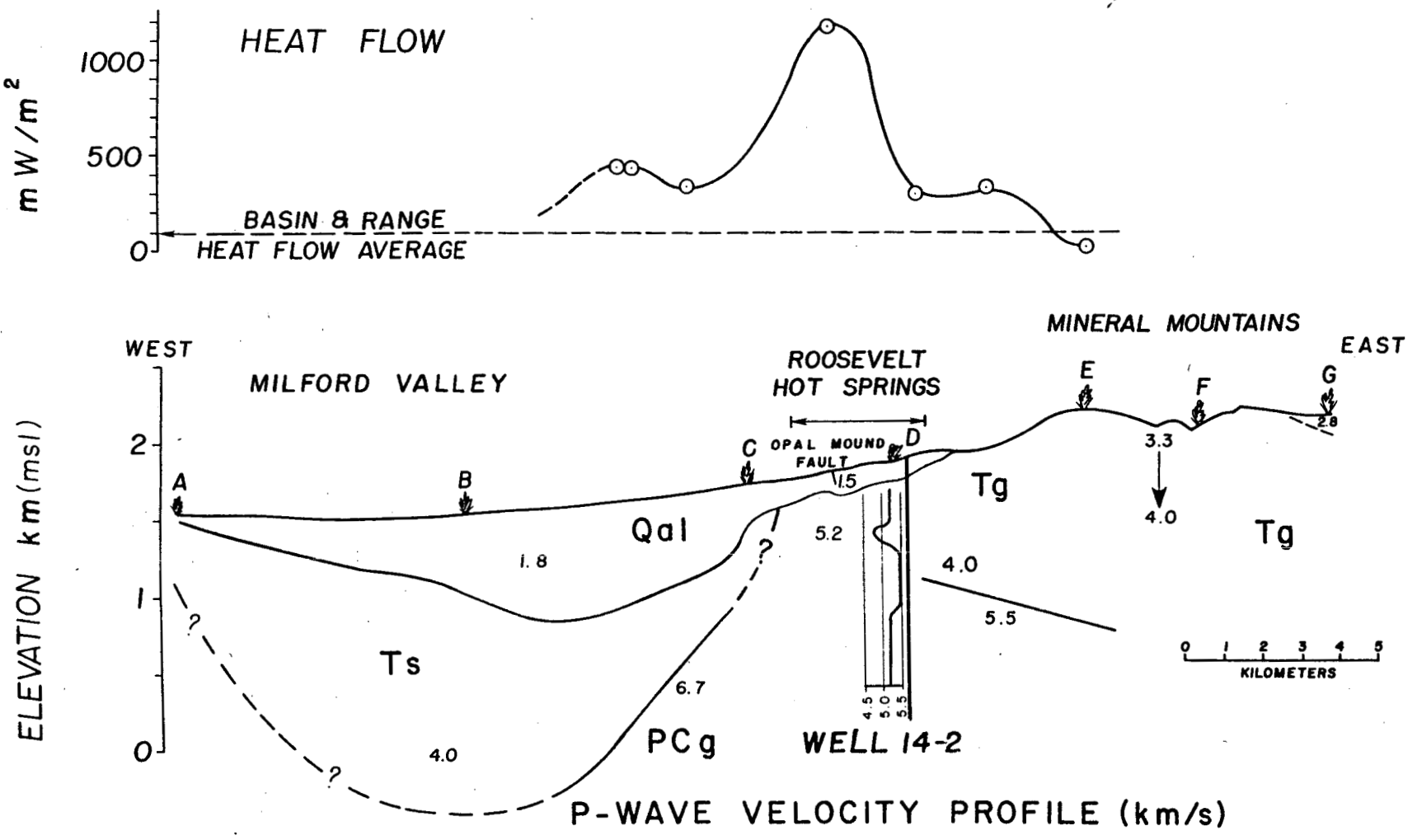

Figure 25. Interpreted velocity-depth model from first arrival time of refraction data. Milford Valley data interpreted using delay-time analysis. Surface gradient in the Mineral Mountains interpreted by Herglotz-Wiechert inversion. Generalized sonic log shown beside well 14-2. Heat flow data from Ward et al. (1978).

geophones west of shot point C between 13.5 and 14.5 km.

The composition of layer 2 can only be estimated since no well log control is available for the Milford Valley. In a geologic environment similar to the Roosevelt Hot Springs area, Arnow and Mattick (1968) identified three velocity units from a refraction profile southeast of Antelope Island in the Great Salt Lake of northern Utah. Their second layer exhibited a maximum velocity of 3.8 km/s, close to that of 4.0 km/s assigned to layer 2 of the Milford Valley. Arnow and Mattick (1968) interpreted this near surface layer to be Tertiary age silts, clays, and volcanics on the basis of well logs and mapped basin geology. Based on the geologic similarities of the Milford Valley to the Great Salt Lake basin and the observed seismic velocities, layer 2 of the graben is interpreted to be composed of Tertiary sediments.

High apparent velocities between 12.0 km and 16.5 km from shot points A and B are indicative of seismic waves propagating up-dip along the interface between layers 2 and 3. To determine the true velocity of layer 3, waves originating from shot point C that reach the surface between 9.0 and 13.0 km are used. The propagation paths of the P-waves probably approach true subsurface reversal since the refraction profile is linear on the western side of the Milford Valley. A true velocity estimate made by using the Hobson-Overton technique resulted in a value slightly more than 6.6 km/s.

In addition to the seismic data, a sonic log from Getty Oil Company well 52-21, located approximately 2.5 km southeast of shot point C, was examined (see Figure 1). The metamorphic rock

encountered in the drill hole has been assumed to be the rock that underlies the Milford Valley (Nielson et al., 1978). For depths to the interface, between layer 2 and layer 3, the sonic log indicates a velocity of 6.7 km/s (see Figure 2). Since the velocity estimated by the Hobson-Overton method and the velocity determined from the sonic log were so close, a velocity of 6.7 km/s was used in modeling layer 3 and was interpreted here as seismic basement.

A finite layer over a half space was used in describing the velocity structure between shot points C and D. A surficial layer with a velocity of 1.5 km/s overlies the basement layer with a velocity of 5.2 km/s that dips approximately 5° to the west.

Travel-time branches from sources east of shot point D and west of shot point C indicate that the velocity of the basement layer between shot points C and D is 5.2 km/s. Further evidence for this velocity was obtained from a sonic log of Thermal Power well 14-2, located approximately 0.4 km north of shot point D (Figure 1) that showed a velocity of 5.2 km/s for the granite (see Figure 2).

A change in basement velocity near shot point C from 6.7 km/s to 5.2 km/s cannot be rejected since a change in rock type occurs. The location of the lateral velocity change is uncertain however, an estimate of the position can be made from the travel-time curves (see Figure 24). Apparent velocities of travel-time branches from shot points C and D show that a velocity of 5.2 km/s may exist across the entire spread. On the other hand, apparent velocities for branches from shot points A and B indicate that layer 3 with a velocity of 6.7 km/s may extend nearly 2 km east of shot point C.

The absence of identifiable reflections from the basement between shot points C and D is a problem that has been noted previously. In an attempt to shed light on this question, synthetic seismograms were generated for two subsurface velocity distributions using a modified Cagnaird-DeHoop technique (Mellman and Helmberger, 1978). In both cases, the granite was modeled with a slight positive velocity gradient from 5.1 km/s to 5.5 km/s at a depth of 1 km. As expected reflections were found to be present in all records from 0 km to 5 km from the source.

When the change from alluvium to granite was modeled as a velocity step at a depth of 0.1 km, the reflections from the basement layer were generally five to six times greater in amplitude than the head wave and the two phases were separated in time. However, when the upper 0.1 km of granite was modeled as a velocity transition from 2.5 km/s to 5.1 km/s, the reflection and the head wave were not as distinguishable. The amplitudes of the reflections were only twice as great as the first arrival amplitudes, and for distances between 0 km and 2 km, the reflection and the head wave appeared to be a single phase. Beyond 2 km the two phases were separated in time but their amplitudes were nearly equal.

Since the sonic log from Thermal Power well 14-2 near shot point D does not begin until a depth of 0.2 km, the existence of a velocity transition zone in the upper 0.1 km of granite is not known. However, the absence of identifiable reflections in the Roosevelt refraction data between shot points C and D may be explained by considering a velocity transition. Synthetic seismograms suggested that for a

distance range of 0 km to 2 km from the source, reflections from the granite may be neither sufficiently larger in amplitude nor separated adequately in time from the head wave arrivals. On real seismic recordings where background noise and energy absorption exist, the possibility of locating the two phases may be reduced even further.

East of shot point D, the surface layer eventually thins out. On the geologic map the layer ends where the granite is first exposed at the surface 2.5 km east of shot point D.

Seismic analyses for the areas of the granite pluton required special attention. Elevation differences of up to 600 meters between geophones in the Mineral Mountains required travel-times to be corrected to a horizontal datum. For spreads recorded from shot points E, F, and G, the datum was the elevation of the sources (not the surface elevation). A velocity of 2.3 km/s used in the datum correction was determined from the direct arrivals propagating eastward from shot point E.

Figure 26, a plot of the travel time versus distance for geophones located on granite or basalt and recording shot points E, F, and G, reveals excessive scatter of some time points of up to 0.05 sec from best-fit curves. The scatter is partly caused by too low of a velocity used in the datum correction. However, if a velocity of 3.0 km/s were used, the scatter of some time points would still exceed 0.04 sec, an insignificant improvement. The scatter, therefore, may be caused by localized geologic effects or perhaps by lateral velocity variations deeper than the datum.

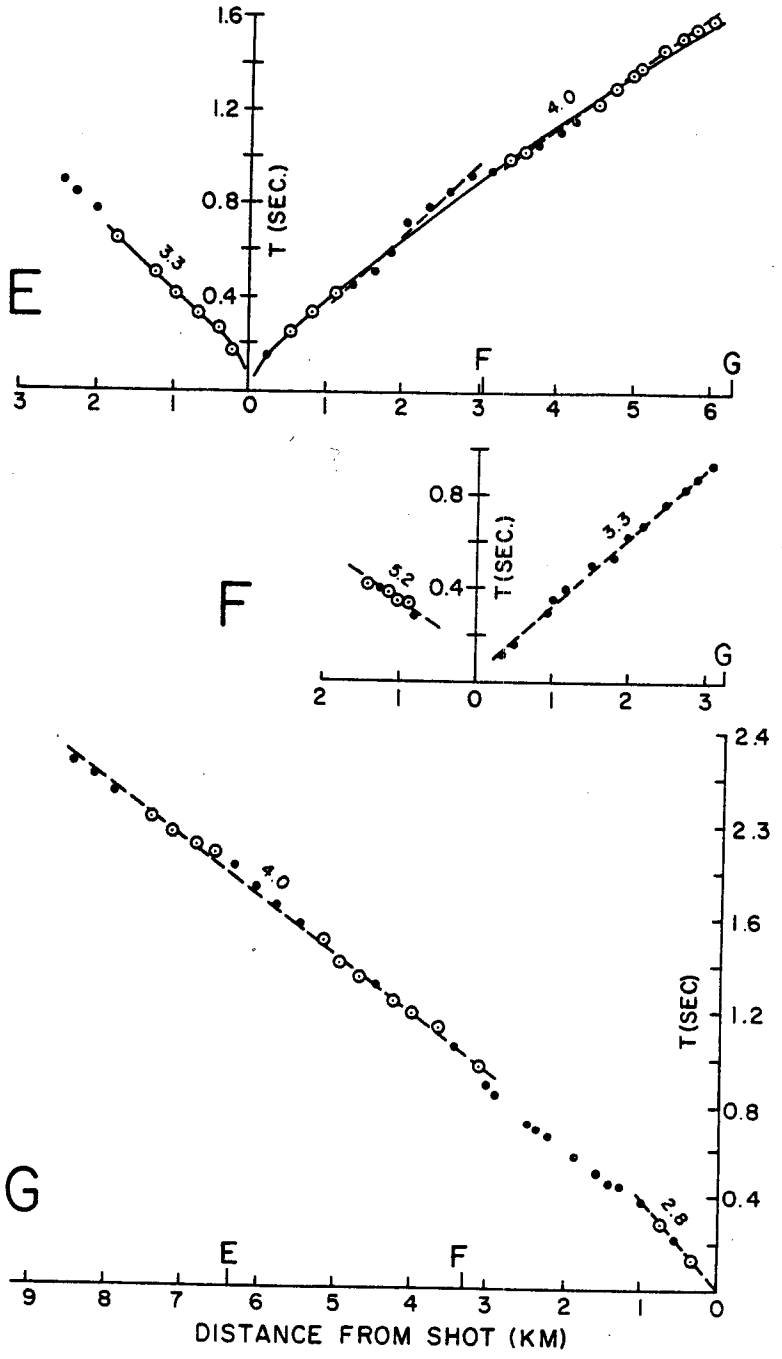

Figure 26. Datum corrected travel-times versus distance for Mineral Mountains first arrival times. Solid lines of shot point E show interpreted apparent velocity versus distance curve. Dashed lines of shot point E, F, and G indicated least squares straight lines through data. Times with circles are travel-times requiring the least time correction.

To compute the apparent velocities from the travel-time curves determined from the refraction data of shot point E, the time-distance points were fit by a least-squares second-order curve. The resulting equation yields the apparent velocity at any distance between 0 km and 6 km. Second-order curves were also fit to the time-distance points within one km east and west of shot point E. Solid lines are used to represent these curves in Figure 26. The Herglotz-Wiechert inversion method was then applied to the calculated curves assuming that the apparent velocity increased with depth.

Under the assumption that the travel-time branch east of shot point E represented a constant velocity, a least-squares straight line was determined using only the picks for where there was essentially no correction necessary to bring the geophone to a datum. Using picks with the least travel-time error, the resulting computation yielded a better estimate of velocity. Likewise, least-squares fits were computed for the time-distance points from shot points F and G. Curve fitting was not necessary for the picks determined from the data of shot points F or G since the time-distance points gave no evidence for seismic waves having traveled through velocity gradients. The dashed lines on Figure 26 represent the least-squares straight lines.

For the first shot point E, the Herglotz-Wiechert inversion was carried out for travel-times from 0 km to 1 km to the west. The resulting interpretation is a velocity increase from 2.4 km/s at the surface to 3.3 km/s near 0.2 km depth. A continuous increase in velocity from 2.4 km/s to nearly 5 km/s at a depth of 1.2 km is interpreted when inversion of all travel-time points to the east are

used. If we assume that a constant velocity of 4.0 km/s is represented by the picks between 1 km and 6 km east of shot point E and that a velocity gradient is represented by the picks between 0 km and 1 km, the interpreted velocity-depth model exhibits an increase in velocity from 2.4 km/s at the surface to 4.0 km/s at 0.2 km depth with a constant velocity below 0.2 km. Though the P-waves propagating west appear to have a lower velocity than those propagating east, the velocities may not be significantly different since the velocity estimate to the east involved time-distance points out to 6 km from the source.

A constant velocity of 3.3 km/s is represented by time-distance points plotted from 0 km to 3 km east of shot point F. This is directly comparable to velocities found for waves propagating west from shot point E. However, a much higher velocity of 5.2 km/s is exhibited by the picks from shot point F where the refraction profile is aligned north-south. If the granite is either anisotropic or unfractured in this region then the differences in the velocities for the two orientations may be considered significant. A lack of evidence negates any further major conclusions from being made.

Shot point G was different from shot points E or F because the charge was detonated in basalt and most of the data were recorded from geophones located on granite. Any delay or advance of travel-times caused by the basalt will be reflected in the travel-times picked for the geophones in the remainder of the profile. The velocity of the basalt of 2.8 km/s was determined from the time-distance points from 0 km to 1 km west of shot point G. A constant 4.0 km/s is determined

from waves arriving between 3 and 9 km of the source.

In Figure 19 a large increase in apparent velocity from 3.7 km/s to 6.6 km/s occurs for seismic waves originating from shot point G and arriving at geophones between shot points D and E. Since the velocity structure of the Mineral Mountains appears similar to a layered velocity structure, this apparent velocity increase is also interpreted to be due to waves that have refracted along a velocity interface at depths below the 4.0 km/s layer determined previously.

Geology and drill hole data indicate that this interface occurs within the pluton. However, the velocity of 6.6 km/s appears relatively high for igneous rocks under low pressures and shallow depths. First arrivals of seismic waves received near shot point D imply that the velocity interface may extend in the subsurface far enough west to intersect Thermal Power drill hole 14-2 located approximately 0.4 km north of shot point D. An examination of the acoustic log taken from the well indicates an increase in velocity from 5.2 km/s to 5.5 km/s between 0.65 km and 1.0 km depth (Figure 2). An estimate of the true velocity for this layer at depths greater than 0.7 km is thus 5.5 km/s. An average velocity of 3.8 km/s for the rocks above the interface is chosen from the time-distance points plotted west of shot point G in Figure 26. From these two true velocities an estimate of the dip of the interface can be calculated.

Since the P-waves recorded from shot point G have a greater apparent velocity than the estimated true velocity for the pluton, the waves must be propagating up-dip. Using standard refraction travel-time equations, the dip of the velocity interface was

calculated to be 5° east. The depth of the interface beneath shot point E is approximately 1.4 km and beneath shot point D, if the interface extends far enough west, the depth to the velocity change is approximately 0.6 km. This calculated depth corresponds to the upper portion of the velocity increase shown on the sonic log of well 14-2.

An interpretation of the velocity interface can be made by examining the data plotted in Figure 2b. The projected extension of the interface to Well no. 14-2 corresponds to a change from granite to monzonite at a depth near 0.65 km. If the velocities were related to rock composition then the velocities in the drill hole above the granite would also be 5.5 km/s. However, the sonic log does not indicate this. The plagioclase alteration intensity curve offers a better clue. Since hydrothermal alteration intensity is directly related to the degree of fracturing, the monzonite and granite above the interface must be extensively fractured. Therefore, the unusually low velocities for the Mineral Mountains appear to be more related to the fracturing and alteration than the lithologic discontinuities.

The velocity structure of the Mineral Mountains granitic pluton determined from the seismic refraction data is shown in Figure 27. The P-wave velocity is an unusually low 2.4 km/s at the surface with the velocity increasing to 3.3 km/s at a depth of 0.2 km. Seismic waves propagating east or west and surfacing between 1 and 3 km from the source have a velocity of 3.3 km/s. These waves have probably traveled as shallow turning rays just below the shallow velocity gradient. P-waves arriving at geophones greater than 3 km from the source with a velocity of 4.0 km/s have propagated just below the 3.3

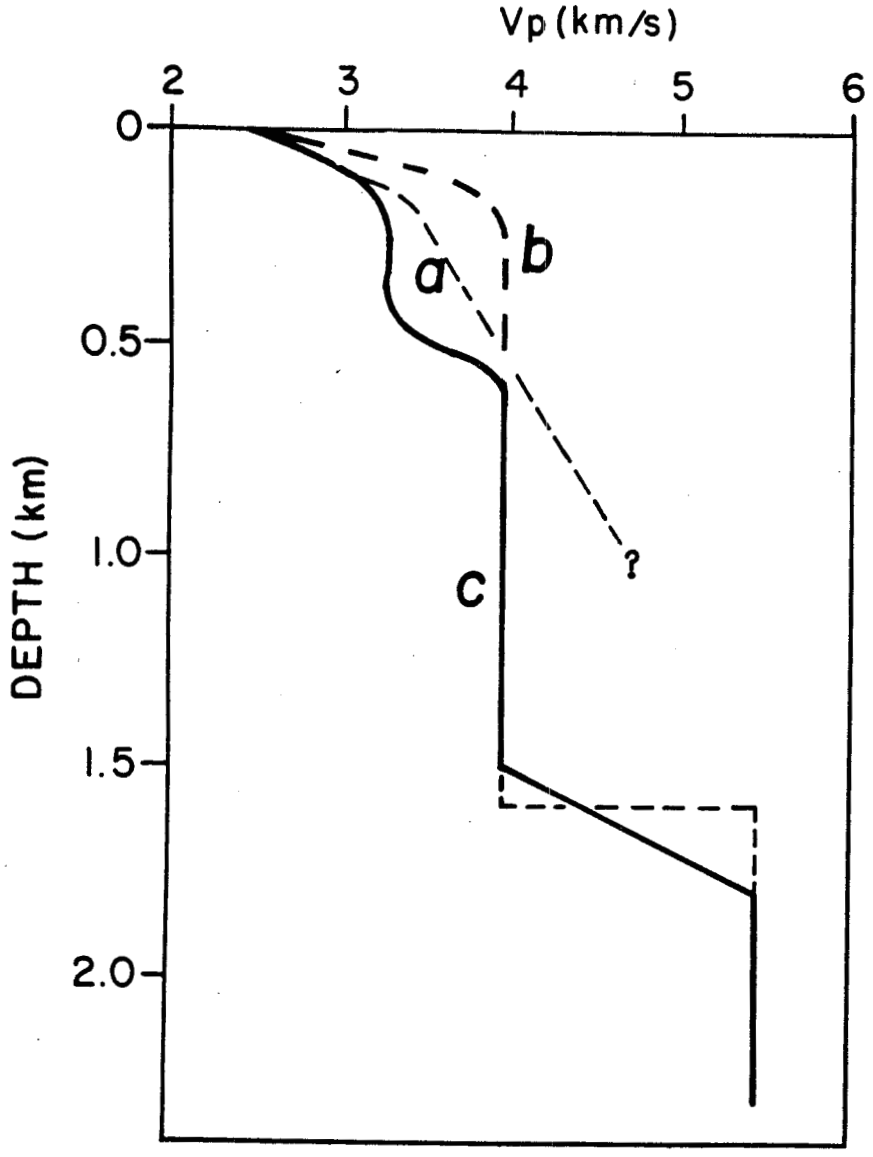

Figure 27. Mineral Mountains velocity depth curves (a) interpreted velocity gradient from inversion of travel-times east of shot point E (solid line, Figure 26) (b) interpreted velocity gradient from inversion of travel-times east and west of shot point E and from constant velocity east of shot point E (dashed line , Figure 26) (c) interpreted velocity-depth curve from all travel-time data. Depth of transition zone between 4.0 km/s and 5.5 km/s varies depending upon location.

km/s layer at a depth of 0.5 km. At a depth of approximately 1.4 km beneath shot point E, the P-wave velocity from granite increases to 5.5 km/s. These velocity changes appear to be related to the intensity of fracturing in the pluton.

CHAPTER 5

AMPLITUDE VARIATIONS OF THE SEISMIC REFRACTION DATA

Introduction

Amplitude decay, attenuation, and the quality factor, Q, are mathematically related by simple formulas. As a spherical wave spreads from its source, the energy must be distributed over the area of the sphere. Thus, the energy per unit area decreases inversely as the square of the distance from the source. The amplitude is inversely proportional to the distance the wave has traveled. The decrease in amplitudes is not due to spherical spreading alone, but also to absorption of seismic wave energy during its propagation because of the internal friction in rocks. This dissipation of energy comes about mainly in the frictional losses by movement within a solid of one surface past another and by direct conversion of mechanical energy into thermal energy. The energy loss due to absorption is exponential with distance.

For a homogeneous material, the amplitude A at a distance x from the source is given by

$$A = A_o \frac{x_o}{x} e^{-\alpha x} \qquad (12)$$

where A_0 equals the amplitude at a distance x_0, and α equals the absorption coefficient. For a given material, since the wave period T is inversely proportional to α, the absorption term exp $(-\alpha x)$ is

constant for a distance equal to the wavelength λ (Bath, 1973). This can be written as

$$e^{-\alpha\lambda} = e^{-\pi/Q} \tag{13}$$

where $\lambda = Tv$, and v equals the wave velocity. Q is related to α by $Q = \pi/\alpha Tv$. Therefore,

$$A = A_o \frac{x_o}{x} \exp\left(-\frac{\pi f x}{Qv}\right) \tag{14}$$

where f equals frequency. As can be seen, Q increases when absorption decreases.

As was discussed in Chapter 1, several factors such as rock type, porosity, temperature, pressure, and degree of fracturing may influence attenuation in geothermal areas. Mapping Q over a broad region will indicate anomalous zones of attenuation caused by these factors. The cause for abnormal attenuation and velocity may be seen to be related when Q is coupled with a map of velocity changes. For example, in areas of silica or carbonate deposition by hydrothermal fluids, an anomalous zone of high Q and high velocity may be seen. On the other hand, areas of low Q and low velocity with respect to the surroundings may suggest high porosity, high temperatures, or fracture zones.

Seismic wave amplitudes are also sensitive to velocity gradients. Even small increases in velocity with depth are capable of affecting amplitudes of head waves by one to two orders of magnitude. Braile (1977) has stated that the combined interpretation of travel-times and amplitudes of refracted and reflected waves best determines the presence of velocity gradients within layers. However, the effects of

velocity gradients and anelasticity cannot be distinguished by using only amplitude decay with distance (Hill, 1971).

With these limitations, interpretation of amplitudes measured from the record sections can be discussed. Because the first motion of the initial P-phase could not be identified with certainty on all records, the amplitudes were measured at the maximum peak-to-trough displacement in the first one or two cycles of the arrival. Since the technique is neither rigorous nor precise in amplitude determination only a qualitative interpretation is given.

Interpretation and Discussion

The following plots display the first arrival amplitudes versus distance for all shot points except shot point F. Though some scatter exists in the data due to local site responses and possible inaccuracies in the amplitude corrections, the large number of stations defines the trend of the amplitude decay reasonably well. Scatter in amplitudes between shot points A and C across the Milford Valley may also be due to the differing angle of emergence for the ray paths. Vertical geophones will have a greater response to energy emerging up-dip from layers that are dipping away from them. It can be seen that most of the amplitudes decay at rates between $1/x$ and $1/x^2$. The amplitudes of classical head waves decrease at a rate of $1/x^2$ for large distances (Grant and West, 1965).

For some time it was believed that the first arrivals greater than one km from shot point A were all originating from a head wave propagating along the top of the basement (Figure 28). However, when

Figure 28. Normalized amplitude versus distance plot for first arrivals from shot point A. Solid lines show amplitude decay curve referenced to estimated relative amplitude at one km.

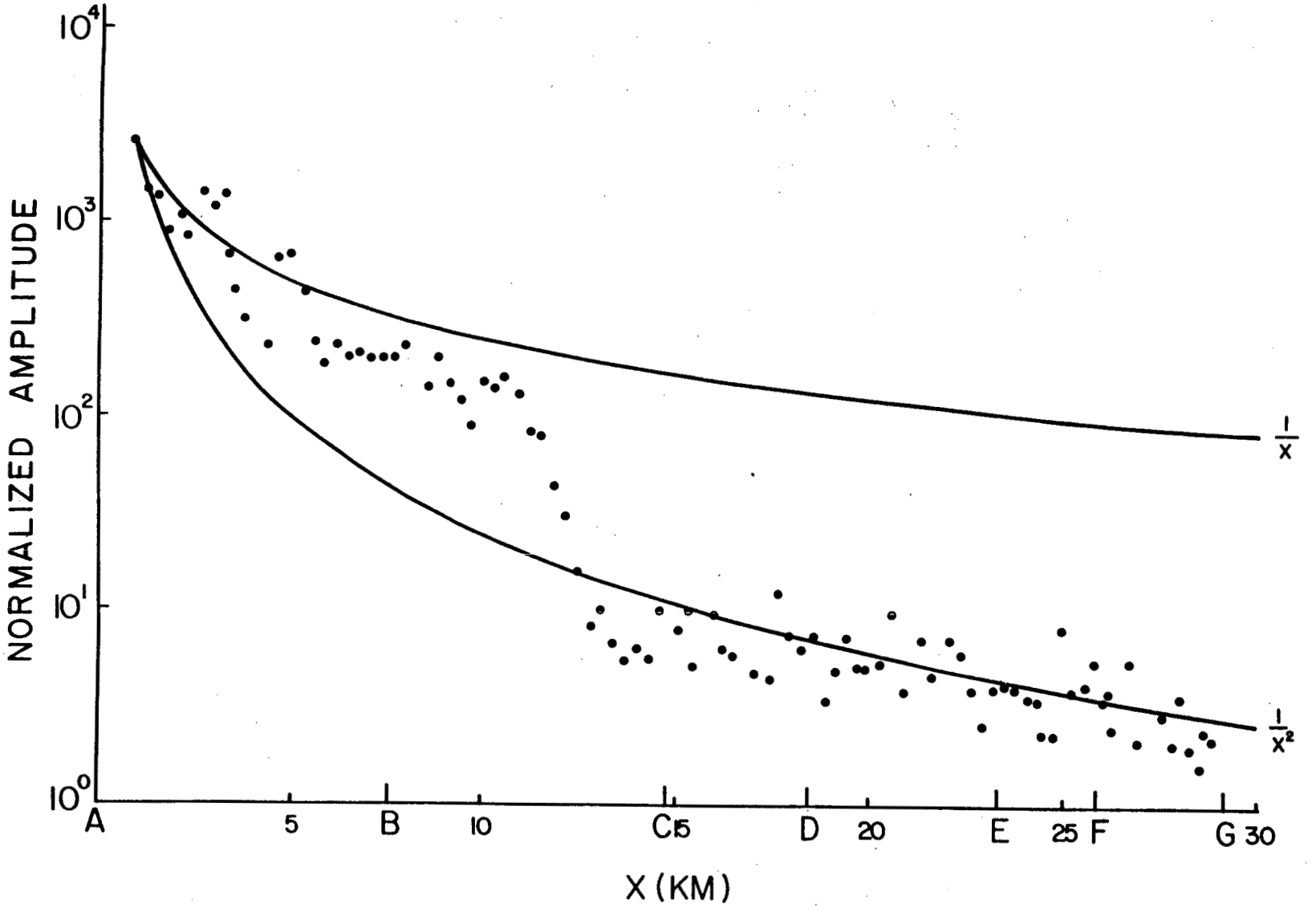
NORMALIZED AMPLITUDE
10^4
10^3
10^2
10^1
10^0
A
5
B
10
C15
D
20
E
25 F
G 30
X (KM)
$\frac{1}{x}$
$\frac{1}{x^2}$

the amplitudes were plotted a large decrease between 11 and 12 km from shot point A cast some doubt on this interpretation for several reasons. The decrease occurs only over a distance of 600 to 700 m. Also, a large increase in apparent velocity previously interpreted to be caused by a change in basement dip occurred over the same spread. This suggests that the first arrivals originated from two different layers rather than an unusual velocity model where head wave amplitudes decrease by a factor of 10 within one kilometer of basement. It was assuring to find that when amplitudes were plotted for shot point B (Figure 29), the same decrease occurred between 4 and 6 km where basement head waves had already been initially interpreted to be first arrivals.

One of the most interesting aspects of these data is that on all plots, the amplitudes remain nearly constant or only slightly decreasing between shot points C and D. That is, waves propagating across the Roosevelt Hot Springs KGRA vary less in amplitude than waves propagating both east and west of the KGRA. The only shot point from which this is not clearly seen is shot point D; however, the amplitudes do exhibit a greater decrease west of shot point C than between shot points C and D (Figure 31). Even for receivers close to the source (i.e. shot point C, Figure 30), the amplitudes are nearly constant. However, the amplitudes could not be determined within one km of shot point C since the records were clipped.

There are at least two possibilities for the low attenuation in the geothermal area. Beyer et al. (1976) found a higher Q in the vicinity of the Leach Hot Springs, Nevada, along with a velocity

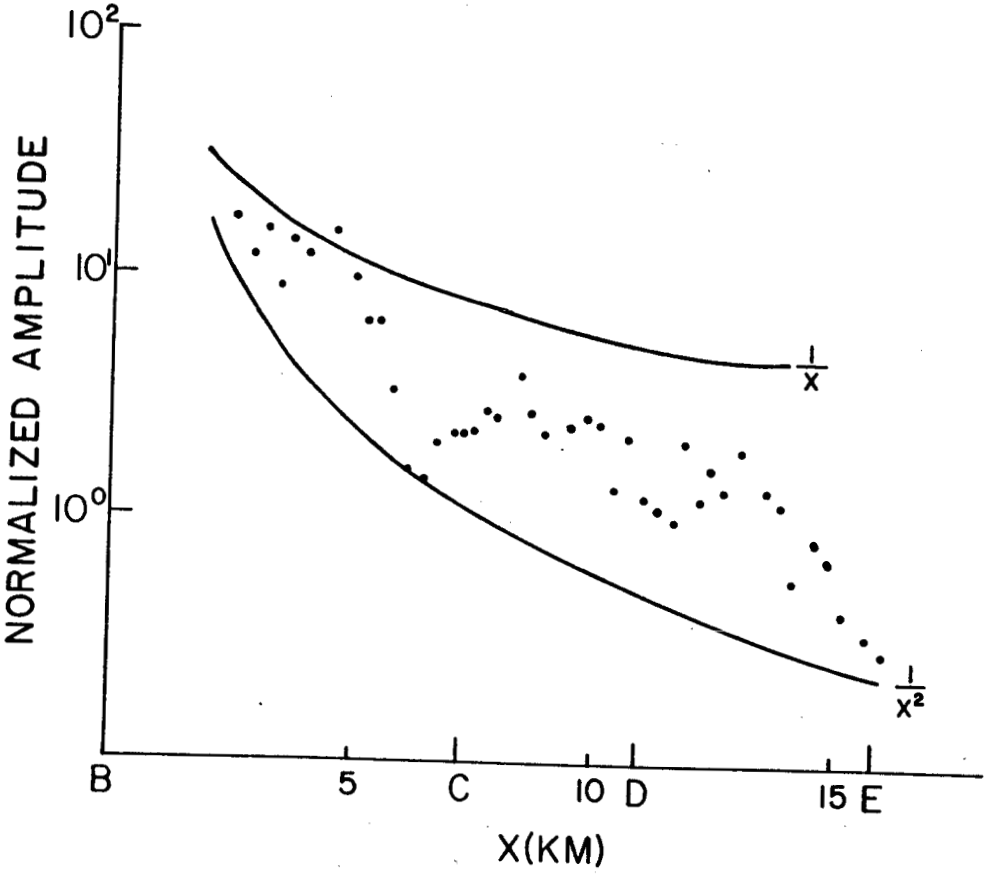

Figure 29. Normalized amplitude versus distance plot for first arrivals from shot point B. Solid lines show amplitude decay curve referenced to estimated relative amplitude at one km.

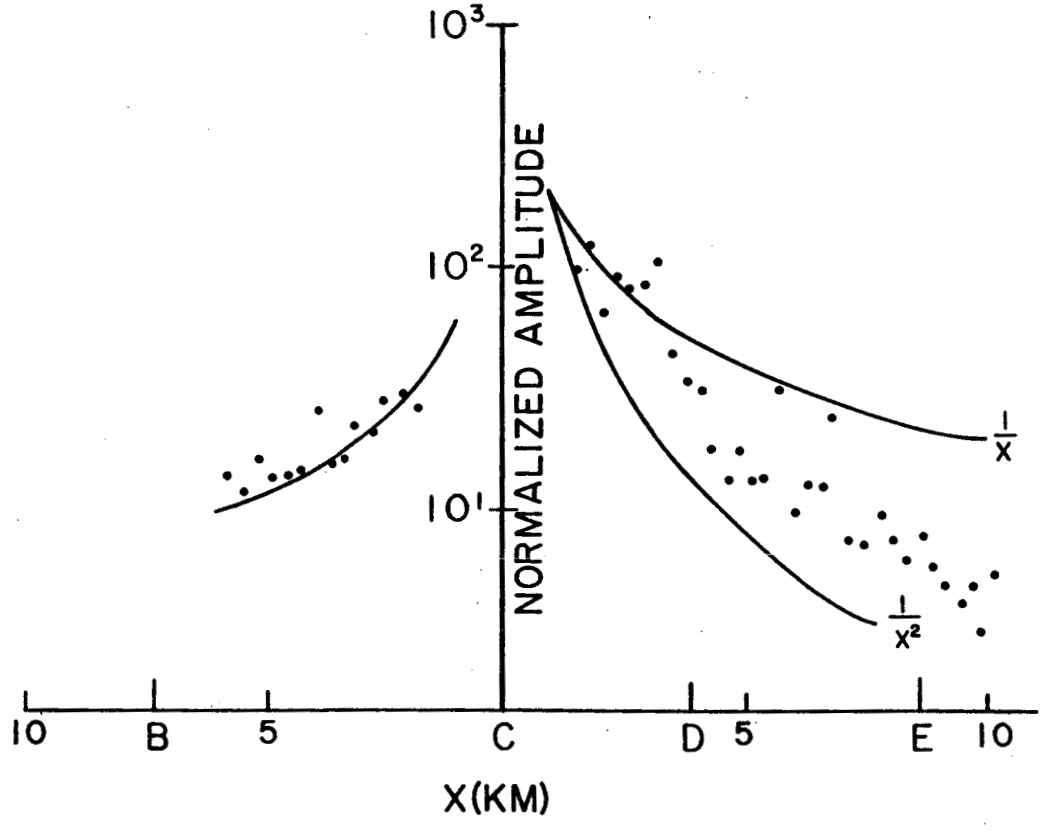

Figure 30. Normalized amplitude versus distance plot for first arrivals from shot point C. Solid lines show amplitude decay curve referenced to estimated relative amplitude at one km.

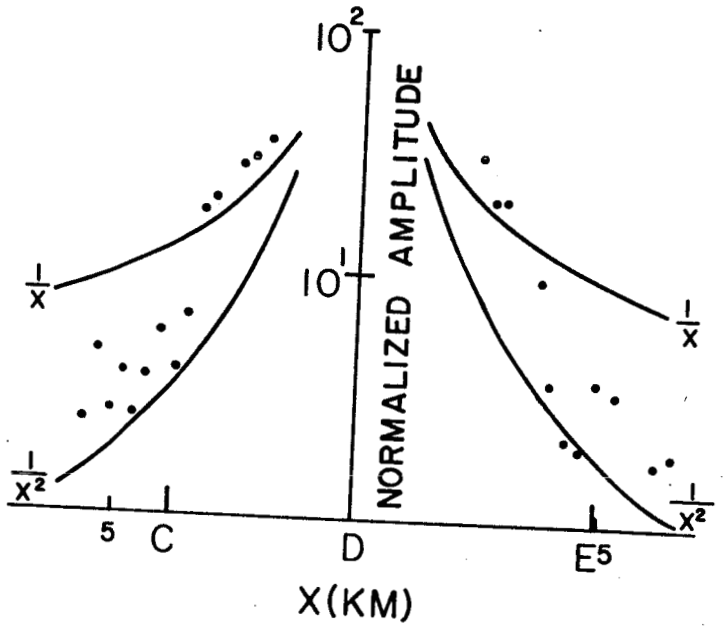

Figure 31. Normalized amplitude versus distance plot for first arrivals from shot point D. Solid lines show amplitude decay curve referenced to estimated relative amplitude at one km.

increase. The cause of both was suggested to be due to the dominance of materials that are much denser than the surrounding rocks. The increased density probably resulted from the deposition of silica from the hot springs. Since there has been extensive silica deposition in the Roosevelt KGRA, perhaps the same type of mechanism produced the constant amplitude anomaly.

The second possibility involves the presence of water or steam in the rock of the geothermal system. Q has been found to be initially higher and to increase more rapidly under pressure in dry rocks than in rock containing pore water (Johnson et al., 1979). Likewise, Gardner et al. (1964) showed that Q increased as water content decreased. Therefore, a vapor dominated system would be expected to show less attenuation than a reservoir with significant water. However, given that the Roosevelt KGRA is a liquid dominated system (Berge et al., 1976), this explanation for the cause of higher Q within the geothermal area does not appear feasible.

The data derived from shot points E and G exhibited amplitudes that decayed at a greater rate in the exposed granite of the Mineral Mountains than those along the other parts of the profile (Figures 32 and 33). East of shot point E the falloff approaches $1/x^4$ while west of shot point G the falloff is greater than $1/x^2$. The greater attenuation may be due to the intensely fractured granite. For waves surfacing west of shot point D, the rate of amplitude decay is closer to $1/x$. A significant increase in first arrival amplitude between 20 and 23 km in the record section recorded from shot point G (Figure 19) becomes obvious when the amplitudes versus distance are plotted

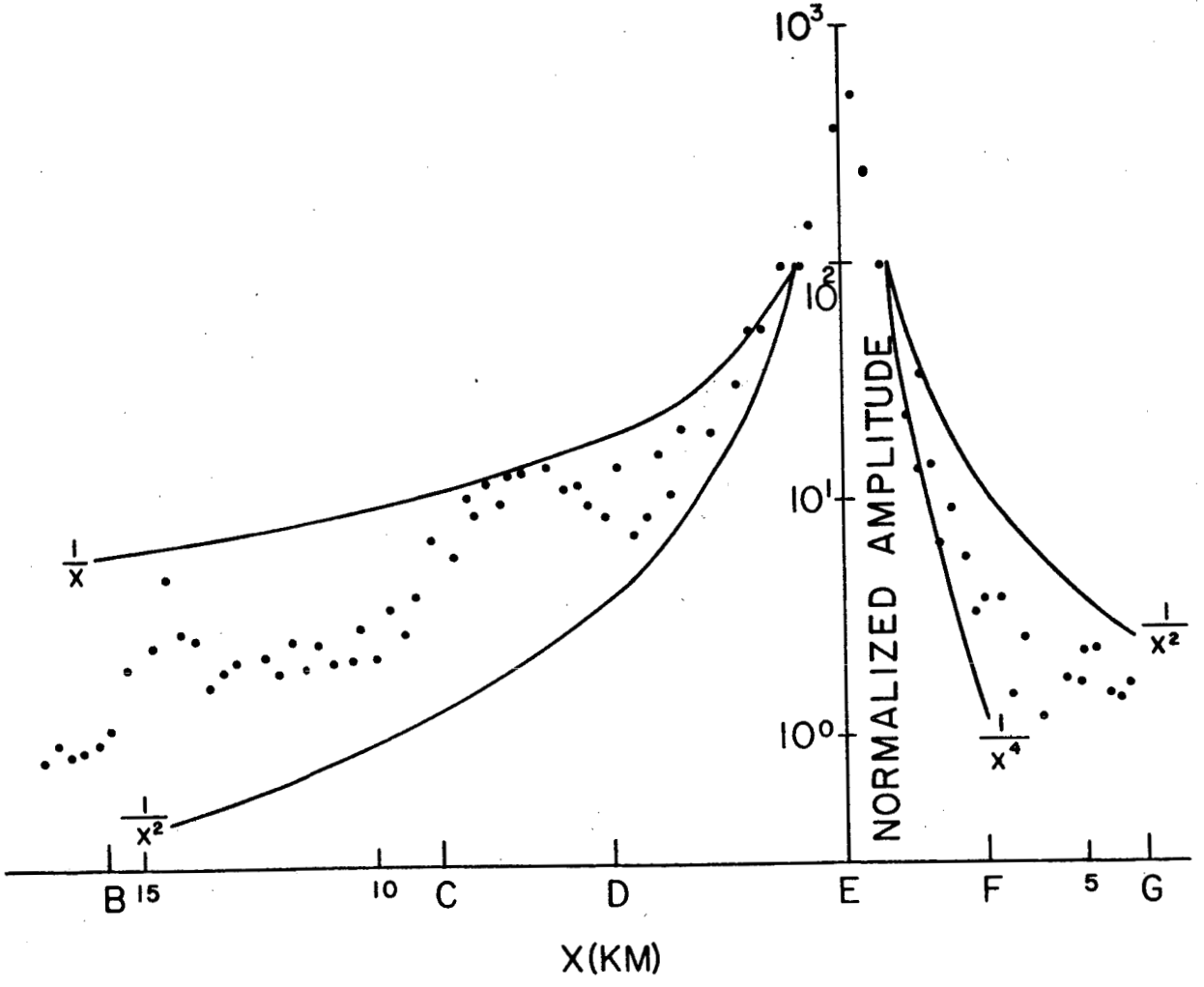

Figure 32. Normalized amplitude versus distance plot for first arrivals from shot point E. Solid lines show amplitude decay curve referenced to estimated relative amplitude at one km.

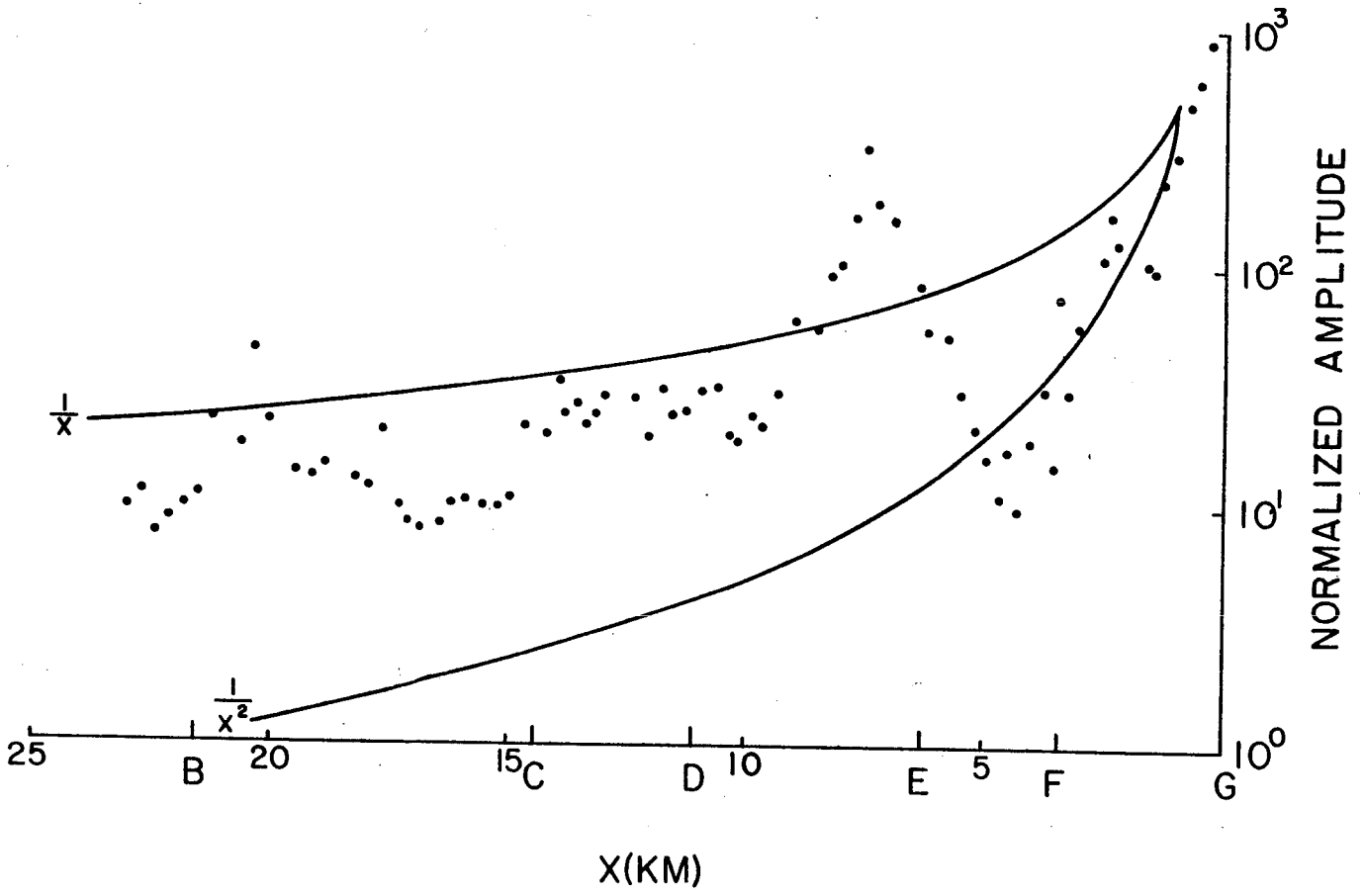

Figure 33. Normalized amplitude versus distance plot for first arrivals from shot point G. Solid lines show amplitude decay curve referenced to estimated relative amplitude at one km.

(Figure 33). At approximately the same distance, first arrival P-waves exhibiting an apparent velocity increase are interpreted to be refractions from the 5.5 km/s eastward dipping layer shown in Figure 25.

Focusing effects arising from constructive interference of two or three phases with nearly equal travel-times in this distance range are an explanation for the increase in amplitudes. Travel-time modeling of the interpreted velocity-depth curve shown in Figure 27 was utilized to test this possibility. The resulting travel-times for the 4.0 km/s refracted phase, the reflected phase from the transition zone, and the 5.5 km/s refracted phase match the experiment's observed travel-times. However, the model was not able to satisfy the location of the maximum interference of these phases which might cause the large amplitude increase. Obviously a more detailed model of the 4.0 km/s to 5.5 km/s transition zone is necessary but continued modeling would require additional assumptions for which there is no control.

CHAPTER 6

GRAVITY MODELING

Since several geological and geophysical studies have been conducted in the Roosevelt Hot Springs - Mineral Mountains area, it is important that their information be integrated into the interpretation of the refraction data. The result gives a better assessment of the subsurface structure with constraints implied from other data.

The structure of the Milford Valley was interpreted from gravity data along a profile approximately 1 km north of the refraction line (profile 2200N, Crebs and Cook, 1976) and along a profile between 1 and 2 km south of the refraction line (profile BB', Carter and Cook, 1978). Using a density contrast between the basement and the valley fill of -0.5 gm/cm^3, these gravity studies show a depth to bedrock in the Milford Valley of 1.4 km. However, the effects of water saturation were ignored. If the alluvium has a density of 2.67 gm/cm^3 then an alluvium porosity of 20 percent is implied from a dry alluvium density of 2.1 gm/cm^3. The density contrast for a 100% water saturated material is -0.3 gm/cm^3. A gravity model using this contrast yielded a maximum depth to bedrock in the Milford Valley of 1.8 km (Tripp et al., 1978).

The choice of a regional gravity field required to calculate a residual profile should approximate the true regional. In the earlier gravity modeling over the Milford Valley, the regional removed was

linear increasing in magnitude to the west. However, Carter and Cook (1978) fit a fifth-order polynomial surface to the gravity data to "best approximate the regional gravity field." The resulting residual gravity anomaly map (Figure 11, Carter and Cook, 1978) indicates that the residual along the refraction profile is less than 15 mgal between the Mineral Mountains and the Milford Valley.

The velocity model determined from the refraction data places the basement at least 1.8 km below the surface 3 km east of shot point B (Figure 25). Uncertainty in the depth is due to the lack of reversed subsurface coverage from the 6.7 km/s layer in the distance range of 0 to 10 km. Initial comparisons between the gravity model of Tripp et al. (1978) and the seismic model seem to agree reasonably well on the valley depth. However, there are several gross differences.

Since three layers are used in describing the velocities in the subsurface beneath the valley, three different densities are necessary. The surficial layer with a velocity of 1.8 km/s can be represented by the water saturated alluvium discussed previously. Its density contrast with layer 3, the bedrock, is -0.3 gm/cm^3. The deeper 4.0 km/s layer should be closer in density to that of the bedrock. The rock type is unknown since no well has penetrated this layer.

Woollard (1975) showed a density slightly less than 2.5 gm/cm^3 for sediments with a velocity of 4.0 km/s. Similarly, the Nafe-Drake curve (see Clarke, 1966) gives a density of 2.5 gm/cm^3 for a sediment velocity of 4.0 km/s. Without implying rock type, a density of 2.5 gm/cm^3 is estimated for the 4.0 km/s layer on the basis of the

measured velocity-density curves. This gives a density contrast of -0.2 gm/cm^3. The valley fill appears to have an overall density contrast that is much smaller than the -0.5 gm/cm^3 modeled by Crebs and Cook (1976) and Carter and Cook (1978). Therefore, a valley fill deeper than 1.4 km is required to produce the same gravity relief of 20 mgal. However, if the fifth-order residual anomaly map is used for modeling the lower density contrast may be sufficient for producing 15 mgal of relief.

The gravity effect was computed from the two-layer velocity model of the valley fill (Figure 34). When layer 2, the intermediate 4.0 km/s layer was assigned a density contrast of -0.2 gm/cm^3 the gravity relief across the valley was found to be approximately 14 mgal. The magnitude of this gravity anomaly indicates that a higher-order polynomial surface is a best estimate of the regional gravity field. The fifth-order residual with a maximum relief of 15 mgal corresponds closely to the observed profile using density contrasts of -0.3 gm/cm^3 for layer 1 and -0.2 gm/cm^3 for layer 2.

It is important to note that sandstones of the Navajo formation found along the flanks of the Mineral Mountains have sample densities averaging 2.6 gm/cm^3. However, the majority of the sedimentary section in this area is limestone with a density of 2.7 gm/cm^3. If the 4.0 km/s layer is assumed to be sandstone (density contrast of 0.1 gm/cm^3), the computed gravity anomaly across the Milford Valley graben is approximately 10 mgal (Figure 34). Only a residual resulting from the removal of a polynomial surface higher than fifth-order from the observed gravity would be capable of matching this relief. Carter and

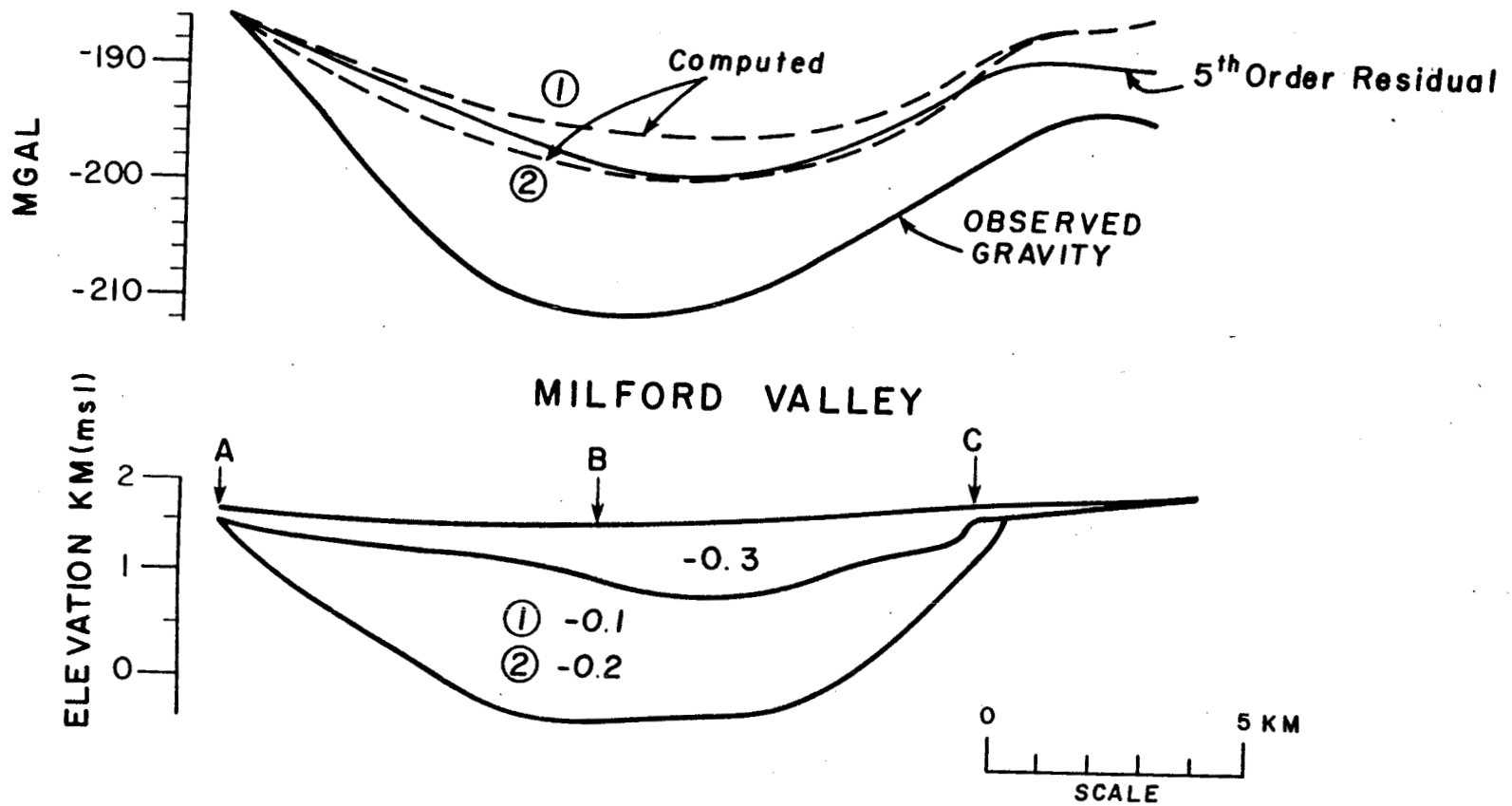

Figure 34. Two-dimensional gravity model for interpreted cross-section along refraction profile. Circled numbers indicate the gravity signature corresponding to the density contrast of layer 2 in Milford Valley graben.

Cook (1978) suggest that these higher-order surfaces are fitting small short wavelength anomalies and the smooth regional effects have already been closely approximated. Therefore, the gravity across the valley is poorly matched when the known sedimentary section is assumed to underlie the surface layer.

The presence of the shallow 5.5 km/s material near the western flank of the Mineral Mountains (Figure 25) may supply a clue as to why the highest values of gravity across the profile are displaced westward from the axis of the range to the vicinity of the Roosevelt Hot Springs. Since an increase in velocity generally implies an increase in density, higher density rock may be closer to the surface beneath the hot springs than beneath the bulk of the mountains. Also, the average velocity and therefore average density of the granite comprising the range (between 0 and 1.5 km depth) determined from the refraction data is lower than the velocity for rocks beneath the thin alluvium cover between shot points C and D.

The gravity contours of the terrain-corrected Bouguer gravity anomaly map (Figure 7, Carter and Cook, 1978) have pronounced gradients of 3 mgal/km over the alluvium adjacent to the western margin of the Mineral Mountains. The geology suggests that this gradient may result from normal faults forming the eastern edge of the Milford Valley graben. Gradients on the magnetic anomaly map also confirm this concept. The location and delineation of major faults and fractures zones are necessary to evaluate the source of the Roosevelt Hot Springs geothermal system.

Previous modeling with gravity and magnetic data have suggested that the faulting on the western edge of the Opal Mound horst begins approximately 0.2 km west of the Opal Mound fault (see Figure 7, Crebs and Cook, 1976). However, the velocity model derived from the refraction data interpreted here indicates that the main range front faulting begins 1 km west of the Opal Mound Fault. Detailed magnetic modeling on line 3000N of Crebs and Cook (1976) (by Dick Fox of the Earth Science Laboratory at the University of Utah) also suggests this configuration. The basement must remain within 100 m to 200 m below the surface out to at least 1.2 km west of the Opal Mound fault. At this distance the magnetic field falls off at 100 gammas/km. Any decreases in the magnetic intensity over a constant depth basement can be attributed to magnetite destruction caused by hydrothermal alteration from interaction of the geothermal system with the host rock. The valley fill thickening abruptly near shot point C is further corroborated by magnetotelluric investigations that indicate a deepening of basement approximately 0.5 km west of shot point C (Wannamaker, 1979, personal communication).

Other evidence for a shallow basement extending to near shot point C is suggested from the 100 m separation, dipole-dipole resistivity map (Figure 44, Ward and Sill, 1976). Conductors appear to exist 1 km west of the Opal Mound Fault. Brine-saturated alluvium produced by fluid leakage toward the valley is one explanation for the low resistivities encountered. If a moderately fractured near-surface basement is present then fluids released beneath the alluvium west of the Opal Mound fault could account for the resistivities.

CHAPTER 7

CONCLUSIONS

The interpretation of a detailed seismic refraction profile has furnished velocity information concerning the subsurface structure of the Milford Valley graben, the Roosevelt Hot Springs KGRA, and the Mineral Mountains horst. Additional information was obtained from a qualitative interpretation of attenuation from P-wave amplitude decay and synthetic seismograms in the geothermal area.

The primary objective was adequately satisfied by travel-time analysis of the first arrival times. Modeling suggests that the Milford Valley graben is composed of two velocity units whose maximum thickness exceeds 1.8 km. The surficial layer varies in thickness from 0.1 km to 0.6 km and has seismic velocities characteristic of Quaternary clays, sands, gravels, and boulders, thought to comprise the unit.

The second layer within the graben is interpreted as a thick Tertiary section of material for which there are no outcrops. The thickness varies from zero at the margins of the valley to greater than 1.2 km at the center near shot point B. This unit is not considered to be Paleozoic or Mesozoic sedimentary rock on the basis of gravity modeling. If limestone, the dominant sedimentary rock of the area, was assumed to comprise layer 2 the rock would have no density contrast with respect to the basement. Samples of sandstone

from the flanks of the Mineral Mountains also do not give a sufficient density contrast with the basement to cause the computed gravity to match the observed gravity anomaly across the Milford Valley graben. Therefore, by assuming the layer to be Tertiary sediments, and assigning a density contrast of -0.2 gm/cm^3 from velocity-density curves, the resulting gravity anomaly fits the fifth-order residual gravity. If the fifth-order polynomial surface contains local anomalies and not just regional effects, either a larger density contrast or a deeper valley is required to fit the observed gravity.

The basement is presumed to be composed of Precambrian(π) gneisses. A sonic log taken in a well on the western edge of the Mineral Mountains encountered metamorphic rock with a velocity of 6.7 km/s that is directly comparable to those velocities calculated from the travel-times of the refraction line.

Beneath the Roosevelt KGRA, granites exhibited a velocity of 5.2 km/s determined from the refraction data and from a sonic log drilled into the pluton. P-wave attenuation across the hot springs area was much less than attenuation in other portions of the profile. This may be caused by the induration of sediments by hydrothermal fluids. Synthetic seismograms suggest that the absence of identifiable reflections from the basement in the geothermal area may be explained by a positive velocity gradient in the upper 100 m of granite beneath the alluvium.

The seismic refraction data indicate that the start of the large displacements in the range front faulting is located at least one km west of the Opal Mound fault near shot point C. This interpretation

is supported by detailed magnetic models that indicate the magnetic basement must increase rapidly in depth to the west of shot point C. Electrical evidence for the location of the main fault is seen in numerous magnetotelluric soundings that show steep gradients of increasing resistivity to the west of shot point C, and in shallow conductors outlined by dipole-dipole resistivity.

No other faults or fracture zones were accurately detected by this refraction experiment. The large station spacings of nearly 250 m does not appear to be adequate for locating narrow structural lineaments. The width of the fracture zone associated with the Hot Springs fault could not be determined since the profile line paralleled the fault.

The bulk of the Mineral Mountains along the profile is characterized by unusually low-velocity granite. A slight positive velocity gradient appears to exist in the upper 0.2 km of the pluton with 3.0 km/s granite beneath the gradient. Velocities of 3.0 km/s extend to approximately 0.5 km where an increase in velocity to 4.0 km/s occurs. The closing of fractures at increased depth is the likely cause for the changes in velocities.

The refraction profile indicates an increase in velocity from 4.0 km/s to 5.5 km/s beneath the western edge of the Mineral Mountains with the increase becoming deeper to the east of the hot springs area. A petrologic study of plagioclase alteration intensity in well cuttings suggests that the velocity change is due to a decrease in fracturing of the igneous complex. The shallow higher velocity (and therefore higher density) material beneath the KGRA coupled with near

surface gneisses probably contributes to the gravity high centered on the western flank of the range.

If the source of the thermal anomaly is detectable by seismic methods, vertical reflections originating from shot points C, D, or E, and surfacing between those shot points should indicate the heat source's seismic properties. However, the record sections do not appear to contain any evidence for seismic waves that have penetrated and returned from hot rock or magma chambers even though an adequate amount of data were recorded to obtain reflections as deep as the Moho. Given that the experiment was not designed for the specific purpose of recording reflections, technical constraints may limit the detection of good reflections. On the other hand, no reflections would be expected if a large impedance contrast did not exist.

Additional seismic data in the Roosevelt Hot Springs KGRA is desirable to help constrain the current geophysical model of the geothermal system. To gather more detailed information about the subsurface structure, several north-south and additional east-west refraction experiments should be conducted across the KGRA. The profiles would not need to go beyond 5 km in length. If possible, geophone spacing should not exceed 50 m in order to have a better chance at locating fracture zones that were not possible in this investigation.

REFERENCES

Arnow, T., and Mattick, R.E., 1968, Thickness of valley fill in the Jordan Valley east of Great Salt Lake, Utah: U.S. Geol. Survey Prof. Paper 600-B, p. B79-B82.

Ballantyne, G. H., 1978, Hydrothermal alteration at the Roosevelt Hot Springs Thermal Area, Utah: Characterization of rock types and alteration in Getty Oil Company well Utah State 52-21: Topical rep. 78-1701.a.1.1.4, DOE/DGE contract EG-78-C-07-1701, 24 p.

Ballantyne, J.M., and Parry, W.T., 1978, Hydrothermal alteration at the Roosevelt Hot Springs Thermal Area, Utah: Petrographic characterization of the alteration to 2 kilometers depth: Technical rep. 78-1701.a.1.1, DOE/DGE contract EG-78-G-07-1701, 26 p.

Bath, M., 1973, Introduction to Seismology: New York, Halsted Press.

Berge, C.W., Crosby, G.W., and Lenzer, R.C., 1976, Exploration and evaluation of Roosevelt KGRA, Utah: AAPG, v. 60, p. 1390.

Beyer, H., Dey, A., Liaw, A., Majer, E., McEvilly, T.V., Morrison, H.F., and Wollenberg, H., 1976, Preliminary open file report on geological and geophysical studies in Grass Valley, Nevada: Lawrence Berkeley Lab. Rep., LBL-5262.

Bjornson, S., Arnorsson, S., and Tomasson, J., 1970, Exploration of the Reykjanes thermal area: UN Symposium on the Development and Utilization of Geothermal Resources, Pisa, Proceedings (Geothermics, Spec. Iss. 2, pt. 2), p. 1640.

Braile, L.W., 1977, Interpretation of crustal velocity gradients and Q structure using amplitude-corrected seismic refraction profiles: The Earth's Crust, AGU Monograph 20, p. 427-439.

Brumbaugh, W.D., and Cook, K.L., 1977, Gravity survey of the Cove Fort-Sulphurdale KGRA and the North Mineral Mountains area, Millard and Beaver Counties, Utah: Tech. rep. v. 77-4, DOE/DGE contract EY-76-S-07-1601, Univ. of Utah, 131 p.

Carter, J.A., and Cook, K.L., 1978, Regional gravity and aeromagnetic surveys of the Mineral Mountains and vicinity, Millard and Beaver Counties, Utah: Final rep. v. 77-11, DOE/DGE contract EY-76-S-07-1601, Univ. of Utah, 179 p.

Clark, S.P., Jr., (editor), 1966, Handbook of Physical Constants: Geol. Soc. of Amer., Memoir 97.

Condie, K.C., 1960, Petrogenesis of the Mineral Range pluton, southwestern Utah: unpub. M.S. thesis, Univ. of Utah, 94 p.

Crebs, T.J. and Cook, K.L., 1976, Gravity and ground magnetic surveys of the central Mineral Mountains, Utah: Final rep. v. 6, NSF Grant GI-43741, Univ. of Utah, 129 p.

Dobrin, M.B., 1976, Introduction to Geophysical Prospecting: New York, McGraw-Hill, Inc.

Earll, F.N., 1957, Geology of the central Mineral Range, Beaver County, Utah: unpub. Ph.D. thesis, Univ. of Utah, 112 p.

Evans, S.H., Jr., 1977, Geologic map of the central and northern Mineral Mountains, Utah: Tech. rep. v. 77-7, DOE/DGE contract EY-76-S-07-1601, Univ. of Utah.

_____, 1978, Studies in Basin and Range volcanism: unpub. Ph.D. thesis, Univ. of Utah.

Gardner, L.W., 1939, An areal plan of mapping subsurface structure by refraction shooting: Geophysics, v. 4, p. 247-259.

Gardner, G.H.F., Wyllie, M.R.J., and Droschak, D.M., 1964, Effects of pressure and fluid saturation on the attenuation of elastic waves in sands: J. Petroleum Tech., v. 16, pp. 189-198.

Goldstein, N.E., Norris, R.A. and Wilt, M.J., 1978, Assessment of surface geophysical methods in geothermal exploration and recommendations for future research: Lawrence Berkeley Lab., Univ. of Cal., Berkeley, DOE W-7405-ENG-48.

Grant, F.S., and West, G.F., 1965, Interpretation Theory in Applied Geophysics: New York, McGraw-Hill, Inc.

Hill, D.P., 1971, Velocity gradients and anelasticity from crustal body wave amplitudes: J. Geophy. Res., v. 76, p. 3309-3325.

_____, 1976, Structure of Long Valley caldera, California, from a seismic refraction experiment: J. Geophy. Res., v. 81, p. 745-753.

Hochstein, M.P., and Hunt, T.M., 1970, Seismic gravity and magnetic studies, Broadlands geothermal field, New Zealand: UN Symposium on the Development and Utilization of Geothermal Resources, Pisa, Proceedings (Geothermics, Spec. Iss. 2, pt. 2), p. 333-346.

Johnson, D.H., Toksoz, M.N., and Timur, A., 1979, Attenuation of seismic waves in dry and saturated rocks, II: Mechanism: Geophysics, v. 44.

Liese, H.C., 1957, Geology of the northern Mineral Range, Millard and Beaver counties: unpub. M.S. thesis, Univ. of Utah, 88 p.

Lipman, P.W., Rowley, P.D., Mehnert, H., Evans, S.H., Nash, W.P., and Brown, F.H., 1978, Pleistocene rhyolite of the Mineral Mountains Utah: geothermal and archeological significance: J. Res. U.S. Geol. Survey 6, p. 133-147.

Majer, E.L. and McEvilly, T.V., 1979, Seismological investigations at the Geysers geothermal field: Geophysics, v. 44, p. 246-269.

Mellman, G.R., and Helmberger, D.V., 1978, A modified first-motion approximation for the synthesis of body-wave seismograms: Geophys. J.R. astr. Soc., v. 54, p. 129-140.

Microgeophysics, Inc., 1977, Refraction shooting near Roosevelt Hot Springs: Data: Final rep., v. 77-4, DOE/DGE contract EY-76-S-07-1601, Univ. of Utah, 56 p.

Nielson, D.L., Sibbett, B.S., McKinney, D.B., Hulen, J.B., Moore, J.N., and Samberg, S.M., 1978, Geology of Roosevelt Hot Springs KGRA, Beaver County, Utah: DOE contract EG-78-C-07-1701, Earth Science Laboratory/Univ. of Utah Research Inst., 120 p.

Olson, T.L., and Smith, R.B., 1976, Earthquake surveys of the Roosevelt Hot Springs and the Cove Fort area, Utah: Final rep., v. 4, NSF grant GI-43741, Univ. of Utah, 83 p.

Oppenheim, A.V., and Schafer, R.W., 1975, Digital Signal Processing: New York, Prentice Hall, Inc.

Pakiser, L.C., and Black, R.A., 1957, Exploring for ancient channels with the refraction seismograph: Geophysics, v. 22, 32-47.

Palmasson, G., 1975, Geophysical methods in geothermal exploration: Second UN Symp. on the Development and Use of Geothermal Resources, San Francisco, Proceedings, v. 2, 1175-1184.

Parry, W.T., Bryant, N.L., Dedolph, R.E., Ballantyne, J.M., Ballantyne, G.H., Rohrs, D.T., and Mason, J.L., 1978, Hydrothermal Alteration at the Roosevelt Hot Springs thermal area, Utah: Final rep. 78-1701.a.1.1, DOE/DGE contract EG-78-C-07-1701.

Petersen, C.A., 1975, Geology of the Roosevelt area, Beaver County, Utah: unpub. M.S. thesis, Univ. of Utah, 49 p.

Sanford, A. R., Mott, R. P., Jr., Shuleski, P. J., Rinehart, E. J., Caravella, F. J., Ward, R. M., and Wallace, T. C., 1977, Geophysical evidence for a magma body in the crust in the vicinity of Socorro, New Mexico: The Earth's Crust, AGU Monograph 20, p. 385-403.

Scott, J.H., 1977, SIPT--A seismic refraction inverse modeling program for timeshare terminal computer systems: U.S. Dept. of Interior, open file rep. 77-365.

Scott, J.H., B.L. Tibbetts, and Burdick, R.G., 1972, Computer analysis of seismic refraction data: US Dept. of Interior, Bureau of Mines, Rep. of invest. 7595.

Sill, W.R., and Bodell, J., 1977, Thermal gradients and heat flow at Roosevelt Hot Springs: ERDA EY-76-S-07-1601, Univ. of Utah, 46 p.

Thangsuphanich, I., 1976, Regional gravity survey over the southern Mineral Range: unpub. M.S. thesis, Univ. of Utah, 37 p.

Tripp, A.C., Ward, S.H., Sill, W.R., Swift, C.M., Jr., and Petrick, W.R., 1978, Electromagnetic and Schlumberger resistivity sounding in the Roosevelt Hot Springs KGRA: Geophysics, v. 43, p. 1450-1469.

Wannamaker, P. E., 1978, Magnetotelluric investigations at the Roosevelt Hot Springs KGRA and Mineral Mountains area, Utah: Topical rep. v. 78-1701.a.6.1, DOE/DGE grant EG-78-C-07-1701, Univ. of Utah, 53 p.

Ward, S.H., and Sill, W.R., 1976, Dipole-dipole resistivity surveys, Roosevelt Hot Springs KGRA: NSF final rep., v. 2, grant GI-43741, Univ. of Utah, 29 p.

Ward, S.H., Parry, W.T., Nash, W.P., Sill, W.R., Cook., K.L., Smith, R.B., Chapman, D.S., Brown, F.H., Whelan, J.A., and Bowman, J.R., 1978, A summary of the geology, geochemistry, and geophysics of the Roosevelt Hot Springs thermal area, Utah: Geophysics, v. 43, p. 1515-1542.

Wilson, W.R., and Chapman, D.S., 1978, Interpretation of heat flow results at Roosevelt Hot Springs, Utah: EOS (abst), v. 59, p. 1201.

Woollard, G.P., 1975, Regional changes in gravity and their relation to crustal parameters: Paper presented at the 7th meeting of the Int. Gravity Comm., Paris, 2-6 Sept., 1974, Bureau Gravimetr. Int., Bull. d'Inform, 36, Sect. I, p. 106-110.

APPENDIX

TPREAD.DECODE

```
      SUBROUTINE DECODE(IREC,NWR,IBLOCK,NWB)
      DIMENSION IREC(1),IBLOCK(1)
      DATA ICOMP /O777777777777/
      DATA IPOS  /O000000000000/
C
C     (9*16) = 144 = (4*36)
C     A BLOCK OF 4 1108 WORDS CONTAINS 9 #'S
C     --- DECODE RECORD IN BLOCK OF 4 1108 WORDS
C
      J = 0
      K = 0
    5 J = J+1
      K = K+1
      FLD(20,16,IBLOCK(K))   = FLD( 0,16,IREC(J))
      FLD(20,16,IBLOCK(K+1)) = FLD(16,16,IREC(J))
      FLD(20, 4,IBLOCK(K+2)) = FLD(32, 4,IREC(J))
      FLD(24,12,IBLOCK(K+2)) = FLD( 0,12,IREC(J+1))
      FLD(20,16,IBLOCK(K+3)) = FLD(12,16,IREC(J+1))
      FLD(20, 8,IBLOCK(K+4)) = FLD(28, 8,IREC(J+1))
      FLD(28, 8,IBLOCK(K+4)) = FLD( 0, 8,IREC(J+2))
      FLD(20,16,IBLOCK(K+5)) = FLD( 8,16,IREC(J+2))
      FLD(20,12,IBLOCK(K+6)) = FLD(24,12,IREC(J+2))
      FLD(32, 4,IBLOCK(K+6)) = FLD( 0, 4,IREC(J+3))
      FLD(20,16,IBLOCK(K+7)) = FLD( 4,16,IREC(J+3))
      FLD(20,16,IBLOCK(K+8)) = FLD(20,16,IREC(J+3))
      K = K+8
      J = J+3
C     20 = 2*9 + 2
C     2000 = 222*9 + 2
      IF(K.LT.NWB) GO TO 5
    6 CONTINUE
C
C     NOW IBLOCK HAS NWB #'S
C     IF POSITIVE, CAN BE PRINTED OR WRITTEN TO DISK
C     IF NEGATIVE #, MORE DECODING IS NECESSARY
C     1108 IS 1'S COMPLIMENT MACHINE
C     TAPE #'S ARE IN 2'S COMPLIMENT FORM
C     ALSO, THE FIRST 20 BITS OF THIS NEGATIVE INTEGER
C     ARE ZERO AND MUST BE SET TO ONE
C
      DO 10 M=1,NWB
      ISIGN = FLD(20,1,IBLOCK(M))
C
C     CHECK LEFT MOST BIT OF 16 BIT WORD
C     IF 1 - # IS ASSUMED NEGATIVE
C     IF 0 - # IS ASSUMED POSITIVE
C     ANY POSITIVE NUMBER LARGER THAN 32,767 WILL BE
C     INTERPRETED AS A NEGATIVE NUMBER
C      I.E.,  32,767 = 0111111111111111
C             32,768 = 1000000000000000
```

```
C      32,768 HAS A ONE IN THE SIGN BIT AND WILL
C      BE TREATED AS A NEGATIVE NUMBER
C
       IF(ISIGN.EQ.0) GO TO 9
C      OTHERWISE, NEGATIVE
C      MAKE 1'S COMPLIMENT
C      EXTEND SIGN BIT TO FULL 36 BIT WORD
       IBLOCK(M) = IBLOCK(M) - 1
       FLD(0,20,IBLOCK(M)) = FLD(0,20,ICOMP)
       GO TO 10
C      POSITIVE
C      ZERO OUT ANY RESIDUAL 1'S FROM LAST RECORD
    9  FLD(0,20,IBLOCK(M)) = FLD(0,20,IPOS)
   10  CONTINUE
C
       RETURN
       END


POWER.DRIVE

C  POWER SPECTRUM ESTIMATION
C   POWER SPECTRUM IS SCALED AND PLOTTED ON SCREEN
C    NX= NUMBER OF DATA POINTS
C    NH= FILTER LENGTH
C    KFILT=0  NO FILTERING
C         =1  FILTER
C    LAG = SMOOTHING FACTOR FOR FILTER
C    CUTLO & CUTHI =  LOW & HIGH FREQUENCY CUTOFFS WITH
C         RESPECT TO NYQUIST
C    DELTA= SAMPLING RATE
C **************************************************
       DIMENSION A(512),X(512),OUT(4096),DATE(2)
       COMPLEX S(4096),H(4096)
       READ(1,97) NX,NH,KFILT,LAG,CUTLO,CUTHI,DELTA
       CALL INITT(120)
       DO 10 IK=6,16
       NR=2**IK
       IF(NX.LE.NR) GO TO 20
   10  CONTINUE
   20  READ(1,98) ISHOT,ISPRD,ITRACE
       READ(2,99) (OUT(J),J=1,NX)
       DO 30 LK=1,NX
       S(LK)=CMPLX(OUT(LK),0.0)
   30  CONTINUE
       CALL SPECT(S,NR,NH,H,KFILT,LAG,CUTLO,CUTHI,DELTA,
      1  A,X,OUT)
       CALL PLOTSS(X,A,NR,1HL)
       CALL GRID
       CALL DATIME(DATE,HOUR)
       WRITE(6,842) DATE,HOUR,ISHOT,ISPRD,ITRACE
       IF(KFILT.EQ.0) GO TO 40
```

```
      WRITE(6,843) NH,CUTHI,LAG
   40 CALL HDCOPY
      CALL ANMODE
      CALL TOUTPT(15)
      CALL CHSYNC
      CALL ERASE
   97 FORMAT (4I5,3F5.3)
   98 FORMAT(3I5)
   99 FORMAT(10F10.0)
  842 FORMAT(1X,3A6///1X,'SHOT=',I2/1X,'SPREAD=',I2/1X,
     1  'TRACE=',I2)
  843 FORMAT(//3X,'NH=',I4/3X,'CUT=',F4.2/3X,'LAG=',I3)
      STOP
      END


POWER.SPECT

C COMPUTES POWER SPECTRUM OF SEISMOGRAMS
C ***************************************
      SUBROUTINE SPECT(S,NR,NH,H,KFILT,LAG,CUTLO,CUTHI,
     1 DELTA,A,X,OUT)
      DIMENSION A(512),X(512),OUT(NR)
      COMPLEX S(NR),H(NR)
      FRQNYQ=1./(2.*DELTA)
      IF (KFILT.EQ.0) GO TO 170
      CALL FORK(S,NR,-1)
      CALL XYFLTR(S,NR,NH,CUTLO,CUTHI,DELTA,3,LAG,H,OUT)
      DO 160 J=1,NR
      S(J)=CMPLX(OUT(J),0.0)
  160 CONTINUE
  170 CALL FORK(S,NR,-1)
C  PERIODOGRAM GENERATED
      DO 180 J=1,NR
      S(J)=CMPLX((CABS(S(J))**2),0.0)
      S(J)=S(J)/FLOAT(NR)
  180 CONTINUE
      CALL FORK(S,NR,1)
      LAGW=INT(0.1*NR)
C  PERIODOGRAM SMOOTHED BY BARTLETT WINDOW
      CALL WINDOW(S,NR,LAGW,2)
      CALL STORE(S,NR)
      CALL FORK(S,NR,-1)
      NR=NR/2
      FAC=FRQNYQ/FLOAT(NR)
      NR=NR/4
      DO 190 J=1,NR
      JJ=J-1
      A(J)=CABS(S(J))
      X(J)=FAC*FLOAT(JJ)
  190 CONTINUE
      RETURN
```

```
      END
```

REFRACTION.XYFLTR

```
C  MAIN SUBROUTINE TO FILTER AND WINDOW
C  ************************************
      SUBROUTINE XYFLTR(FTRAN,NX,NH,CUTLO,CUTHI,DELTA,
     1  NWIND,LAG,H,OUT)
      DIMENSION FTRAN(NX),H(NX),OUT(NX)
      COMPLEX FTRAN,H
      WRITE(6,100) NH,CUTLO,CUTHI,DELTA,NWIND,LAG
      NH2=NH/2
      NN=NX-NH2
      NNPL1=NN+1
      CALL FILTER(CUTLO,CUTHI,H,NX,DELTA)
      CALL STORE(H,NX)
      CALL FORK(H,NX,1)
      CALL WINDOW(H,NX,LAG,NWIND)
      CALL STORE(H,NX)
      DO 14 I=1,NH2
      II=I+NH2
      IJ=NNPL1-I
      H(II)=H(I)
      H(IJ)=CMPLX(0.0,0.0)
   14 CONTINUE
      DO 15 J=1,NH2
      JJ=J+NN
      H(J)=H(JJ)
      H(JJ)=CMPLX(0.0,0.0)
   15 CONTINUE
      CALL FORK(H,NX,-1)
      DO 20 IX=1,NX
      FTRAN(IX)=FTRAN(IX)*H(IX)
   20 CONTINUE
      CALL FORK(FTRAN,NX,1)
      DO 30 IX=1,NN
      IXX=IX+NH2
      OUT(IX)=REAL(FTRAN(IXX))
   30 CONTINUE
      DO 40 IX=NNPL1,NX
      OUT(IX)=CMPLX(0.0,0.0)
   40 CONTINUE
  100 FORMAT(/1X,'SPECS FOR THIS FILTER'/10X,'SIZE OF',
     1  ' FILTER=',I5/10X,'FREQ CUTS ARE CUTLO=',F4.2,
     2 5X,'CUTHI=',F4.2/10X,'SAMPLING INT=',F7.3/10X,
     3 'NWIND=',I1/10X,'LAGS=',I5)
      RETURN
      END
```

REFRACTION.FILTER

```
C CONSTRUCTS NH POINT FILTER
C    CUTLO & CUTHI = LOW & HIGH FREQUENCY CUTOFFS WITH
C                    RESPECT TO NYQUIST
C                    (0.0.LE.CUTLO.LT.CUTHI.LE.1.0)
C    DELTA = SAMPLING RATE
C **********************
      SUBROUTINE FILTER(CUTLO,CUTHI,H,NH,DELTA)
      COMPLEX H
      DIMENSION H(NH)
      NH2=(NH/2)+1
      ANH2=NH2
      CL1=CUTLO-0.00001
      CH2=CUTHI
      DO 10 IX=1,NH2
      AX=IX-1
      RAD=AX/ANH2
      H(IX)=CMPLX(1.,0.)
      IF(RAD.LT.CL1.OR.RAD.GT.CH2) H(IX)=CMPLX(0.,0.)
      IF(RAD.GE.1.0.AND.CH2.GT.0.9999) H(IX)=CMPLX(1.,0.)
   10 CONTINUE
      FNQ1=1.0/(2.0*DELTA)
      WAVLEN=1.0/FNQ1
      CL1=(CL1+0.00001)*FNQ1
      CH2=CH2*FNQ1
      IF(CL1.LE.0.0.AND.CH2.GT..00001) WRITE(6,11)
      IF(CL1.GT.0.0.AND.CH2.GT.CL1) WRITE(6,12)
      IF(CL1.GT..0001.AND.CH2.GT.FNQ1-.0001) WRITE(6,13)
      IF(CL1.GE.CH2) WRITE(6,14)
      WRITE(6,20) FNQ1,WAVLEN,CL1,CE2
   11 FORMAT(1X,'LOW PASS FILTER USED')
   12 FORMAT(1X,'BAND PASS FILTER USED')
   13 FORMAT(1X,'HIGH PASS FILTER USED')
   14 FORMAT(1X,'IMPOSSIBLE FILTER ATTEMPTED.',
     1'  FILTER MUST BE PROPERLY RESPECIFIED.')
   20 FORMAT(2X,'NYQ FREQ=',F10.5,' CYCLES/DATA INT',
     1/2X,'NYQ WAVLEN=',F10.5,' DATA INT',/2X,
     2'LOW FREQ CUT OF FILTER=',F10.5,'CYCLES/DATA',
     3' INT',/2X,'HIGH FREQ CUT OF FILTER=',F10.5,
     4' CYCLES/DATA INT')
      RETURN
      END


REFRACTION.FORK

C COMPUTES FAST FOURIER TRANSFORM
      SUBROUTINE FORK(CX,LX,NSIGN)
      COMPLEX CX(LX),CARG,CEXP,CW,CTEMP
      PI=3.14159265
      SIGNI=NSIGN
      J=1
```

```
      SC=1./FLOAT(LX)
      DO 30 I=1,LX
      IF(I.GT.J) GO TO 10
      CTEMP=CX(J)
      CX(J)=CX(I)
      CX(I)=CTEMP
   10 M=LX/2
   20 IF(J.LE.M)GO TO 30
      J=J-M
      M=M/2
      IF(M.GE.1)GO TO 20
   30 J=J+M
      L=1
   40 ISTEP=2*L
      DO 50 M=1,L
      CARG=(0.,1.)*(PI*SIGNI*FLOAT(M-1))/FLOAT(L)
      CW=CEXP(CARG)
      DO 50 I=M,LX,ISTEP
      CTEMP=CW*CX(I+L)
      CX(I+L)=CX(I)-CTEMP
   50 CX(I)=CX(I)+CTEMP
      L=ISTEP
      IF(L.LT.LX)GO TO 40
      IF(SIGNI.GT.0.0) RETURN
      DO 60 I=1,LX
   60 CX(I)=CX(I)*SC
      RETURN
      END
```

REFRACTION.STORE

```
      SUBROUTINE STORE(H,NX)
      COMPLEX H(NX)
      NX1=NX/2+1
      NX2=NX1+1
      DO 50 IX=NX2,NX
   50 H(IX)=CONJG(H(NX-IX+2))
      RETURN
      END
```

REFRACTION.WINDOW

```
C CONSTRUCTS NX LENGTH WINDOW
C    NWIND=0 NO WINDOW
C          =1 RECTANGULAR
C          =2 BARTLETT
C          =3 HAMMING-TUKEY
C          =4 PARZEN
C    LAG - SMOOTHING FACTOR FOR WINDOW
C ***********************************
```

```
      SUBROUTINE WINDOW(H,NX,LAG,NWIND)
      COMPLEX H
      DIMENSION H(NX)
      PI=3.14159265
      NX2=(NX/2)+1
      XL=LAG
      XL2=XL/2.
      XNX=NX2
      IF(NWIND.EQ.0) GO TO 500
      IF(NWIND.EQ.1) GO TO 100
      IF(NWIND.EQ.2) GO TO 200
      IF(NWIND.EQ.3) GO TO 300
      IF(NWIND.EQ.4) GO TO 400
  100 DO 101 IX=1,NX2
      AX=IX-1
      IF(AX.GT.XL) H(IX)=CMPLX(0.0,0.0)
  101 CONTINUE
      WRITE(6,102) LAG
  102 FORMAT(1X,'RECTANGULAR WINDOW USED   LAG=',I5)
      GO TO 1000
  200 DO 201 IX=1,NX2
      AX=IX-1
      FACTOR=1.0-AX/XL
      H(IX)=H(IX)*FACTOR
      IF(AX.GT.XL) H(IX)=CMPLX(0.0,0.0)
  201 CONTINUE
      WRITE(6,202) LAG
  202 FORMAT(1X,'BARTLETT WINDOW USED   LAG=',I5)
      GO TO 1000
  300 DO 301 IX=1,NX2
      AX=IX-1
      FACTOR=0.5*(1.0+COS(PI*AX/XL))
      H(IX)=H(IX)*FACTOR
      IF(AX.GT.XL) H(IX)=CMPLX(0.0,0.0)
  301 CONTINUE
      WRITE(6,302) LAG
  302 FORMAT(1X,'HAMMING-TUKEY WINDOW USED   LAG=',I5)
      GO TO 1000
  400 DO 401 IX=1,NX2
      AX=IX-1
      FACTOR=1.0-(6.0*((AX/XL)**2))+(6.0*((AX/XL)**3))
      IF(AX.GT.XL2) FACTOR=2.0*(1.0-((AX/XL)**3))
      H(IX)=H(IX)*FACTOR
      IF(AX.GT.XL) H(IX)=CMPLX(0.0,0.0)
  401 CONTINUE
      WRITE(6,402) LAG
  402 FORMAT(1X,'PARZEN WINDOW USED   LAG=',I5)
      GO TO 1000
  500 WRITE(6,502)
  502 FORMAT(1X,'NO WINDOWING HAS BEEN APPLIED')
 1000 RETURN
      END
```

REFRACSCTION.DISP

```
C    PLCTS THE ROOSEVELT HOT SPRINGS REFRACTION DATA
C     REQUIRES :  @ASG,TR 11.,8C9,2479    TAPE ASSIGNMENT
C                 FILE #1 MUST CONTAIN TCOR AND ALPHA
       DIMENSION S(993),SS(22,2),R(1003),TCOR(5),ALPHA(5)
       INTEGER SS
       IMPLICIT INTEGER(F,T)
       REAL T,T1,T2,TINCH,TCOR
       DATA SS/ 5*1,3*3,3*5,2*6,4*7,8,4*9,
      $       1,2,3,4,5,2,3,4,2,3,4,3,4,2,3,4,5,5,2,3,4,5/
C   INPUT THE X DIMENSION FOR CALCOMP PLOTTER IN INCHES
       READ(5,101) XPLOT
       CALL IDPLOT(XPLOT,15.)
       WRITE(6,100)
C   INPUT TRACES TO BE PLOTTED
  100 FORMAT(1X,'ENTER START THEN END FILE & TRACE')
       READ(5,101) FILE1,TRACE1,FILE2,TRACE2
  101 FORMAT(     )
       WRITE(6,102) SS(FILE1,1),SS(FILE1,2),TRACE1,
     & SS(FILE2,1),SS(FILE2,2),TRACE2
  102 FORMAT(1X,'SHOT',I2,' SPREAD',I2,' TRACE',I3,/1X,
     $ 'TO SHOT',I2,' SPREAD',I2,' TRACE',I3)
       IF(SS(FILE1,1).NE.SS(FILE2,1)) GO TO 12345
       FILE=FILE2-FILE1
       IF(FILE.EQ.0) NSEIS=TRACE2-TRACE1+1
       IF(FILE.NE.0) NSEIS=25-TRACE1+(FILE-1)*24+TRACE2
C   INPUT    TCOR--SPREAD STARTING TIME CORRECTION
C            ALPHA-- FACTOR FOR NORMALIZING AMPLITUDES
       READ(1,103) (TCOR(J),ALPHA(J),J=1,5)
  103 FORMAT(F5.3,F10.5)
C   INPUT    EXP--ALL TRACES MULTIPLIED BY DISTANCE**EXP
C            NFILL--EQUALS 9 FOR SHADING POSITIVE PEAKS
C                    EQUALS 1 FOR NO SHADING
C            XFAC--ALL TRACES WILL BE DIVIDED BY XFAC
C            REDVEL--REDUCING VELOCITY IN METERS/SEC
       READ(5,101) EXP,NFILL,XFAC,REDVEL
       FLOVER=FILE1-1
       TROVER=TRACE1-1
       CALL SKPFLS(11,FLOVER,TROVER)
C   INPUT  X1--STARTING DISTANCE IN METERS
C          X2--ENDING DISTANCE IN METERS
C          T1--STARTING TIME OF PLOT IN SEC
C          T2--ENDING TIME OF PLOT IN SEC
       READ(5,101) X1,X2
       READ(5,101) T1,T2
       NX=IFIX((X2-X1)/250.+0.01)
       XINCH=FLOAT(NX)/2.54
       NT=IFIX((T2-T1+4.)*5.+.01)
       T2=T2+4.
```

```
      TINCH=FLOAT(NT)/2.54
      WRITE(6,104) X1,X2,XINCH,NX
  104 FORMAT(/6X,'X1         X2       XINCH    NX',/2F10.0,
     1 F10.5,I5)
      WRITE(6,105) T1,T2,TINCH,NT
  105 FORMAT(/6X,'T1         T2       TINCE    NT',/F9.1,
     1 F10.1,F11.5,I5)
      WRITE(6,106) NSEIS
  106 FORMAT(1X,'  NSEIS=',I4)
C  SCALE OF PLOTS X= 4 CM PER KILOMETER
C                 T= 5 CM PER SEC OF REDUCED TRAVEL-TIME
      SX=(X2-X1)/XINCH
      SZ=(T2-T1)/TINCH
      STEP= 0.004/SZ
      NX1=NX+1
      NT1=NT+1
      CALL PLOT(1.,1.,-3)
      DO 10 I=1,NX1
      X=(I-1)/2.54
      CALL PLOT(X,0.,2)
      CALL PLOT(X,.1,2)
   10 CALL PLOT(X,0.,2)
      CALL PLOT(0.,TINCH,3)
      DO 20 I=1,NT1
      T=TINCH-(I-1)/2.54
      CALL PLOT(0.,T,2)
      CALL PLOT(.1,T,2)
   20 CALL PLOT(0.,T,2)
      FIL=1
C  READS ONE FILE FOR EACH TRACE
      DO 80 I=1,NSEIS
      CALL INOUT(1,11,R,1003)
      NSHOT=INT(R(1))
      NSPRD=INT(R(2))
      NTRAC=INT(R(3))
      IF(I.EQ.NSEIS) GO TO 30
      IF(NTRAC.EQ.24) CALL SKPFLS(11,1,0)
      IF(NTRAC.EQ.24) FIL=FIL+1
      IF(NTRAC.EQ.12.OR.NTRAC.EQ.24) GO TO 80
   30 NPTS=INT(R(9))
      ST=R(5)+TCOR(FIL)
      DIST=R(8)
      T=ST-ABS(DIST)/REDVEL
C  PRINTS OUT SHOT,SPREAD, & TRACE TO ASSURE THAT THE
C   PROPER PLACE ON THE TAPE IS BEING READ
      WRITE(6,107) NSHOT,NSPRD,NTRAC
  107 FORMAT(1X,'SHOT=',I2,'  SPREAD=',I2,'  *** TRACE=',
     1 I2,' ***')
      WRITE(6,108) NPTS,DIST,T,NTRAC
  108 FORMAT('  NPTS     DIST         ST         ID',/I6,
     1 F9.0,F10.3,I9)
C  INPUT IANS--EQUAL 1 TO PLOT CURRENT TRACE
```

```
C                EQUAL 5 TO SKIP ONE TRACE
C                EQUAL 9 TO EXIT PROGRAM
      READ(5,101) IANS
      IF(IANS.EQ.9) GO TO 12345
      IF(IANS.EQ.5) GO TO 80
      DO 40 J=1,993
      S(J)=R(J+10)/25400.
   40 CONTINUE
      DEXP=ABS(DIST/1000.)**EXP
      WRITE(6,109) DEXP
  109 FORMAT(1X,F10.5)
      SC=ALPHA(FIL)*DEXP
      XD=(DIST-X1)/SX
      CALL PLOT(XD,0.,3)
      N=0
      IPEN=3
      IF(NFILL.EQ.9) GO TO 65
C  FOR NO SHADING
      DO 60 J=1,993
      S(J)=-1*S(J)*SC/XFAC
      Y=(T+(J-1)*.004-T1)/SZ
      X=XD+S(J)
      CALL PLOT(X,Y,IPEN)
      IPEN=2
   60 CONTINUE
      GO TO 80
C  FOR SHADING POSITIVE PEAKS
   65 DO 70 J=1,993
      S(J)=-1*S(J)*SC/XFAC
      Y=(T+(J-1)*.004-T1)/SZ
      X=XD+S(J)
      CALL PLOT(X,Y,IPEN)
      IF(S(J).GE.0.0) GO TO 67
      IF(N.EQ.1) GO TO 66
      N=1
      GO TO 67
   66 CALL PLOT(XD,Y,IPEN)
      CALL PLOT(XD,Y+STEP,IPEN)
      N=0
   67 IPEN=2
   70 CONTINUE
   80 CONTINUE
      T=0.
      CALL PLOT(XINCH+1.,T-1.,-3)
      CALL PLOT(0.,0.,999)
12345 CALL FINI
      STOP
      END


HWINV.MAIN
```

```
C  PROGRAM FOR COMPUTING VELOCITY VARIATION WITH DEPTH
C   FROM INPUT VELOCITY-DISTANCE DATA. VELOCITIES ARE
C  INTERPOLATED USING 2ND DEGREE CURVES FIT TO 3 POINTS.
C   N= NUMBER OF INTERPOLATED DISTANCE POINTS
C   M= NUMBER OF INPUT VELOCITY OR DISTANCE POINTS
C   NK = NUMBER OF INTERPOLATED DEPTHS
C   DX = DISTANCE INTERPOLATION INTERVAL
C   DH = DEPTH INTERPOLATION INTERVAL (LAYER THICKNESS)
      DIMENSION X(90),V(90),XXX(180),VV(180),Z(180)
      DIMENSION V1(90),X1(90),Z1(90),H1(90),TTL(16)
      PI=3.14159265
    1 READ(1,43) TTL
   43 FORMAT (16A5)
      READ(1,2) N,M,NK,DX,DH
    2 FORMAT (3I5,2F5.3)
      READ(1,3) (X(I),I=1,M)
      WRITE(6,3) (X(I),I=1,M)
      READ(1,3) (V(I),I=1,M)
      WRITE(6,3) (V(I),I=1,M)
    3 FORMAT (8F10.0)
      I=0
      XX=X(1)-DX
    5 FORMAT(10X,F15.5)
      K=1
   13 I=I+1
    6 FORMAT(20X,I10)
      D=X(I)*X(I+1)*(X(I+1)-X(I))+X(I)*X(I+2)*(X(I)-
     1 X(I+2))+X(I+1)*X(I+2)*(X(I+2)-X(I+1))
      A0=(V(I)*X(I+1)*X(I+2)*(X(I+2)-X(I+1))+V(I+1)*X(I)
     1 *X(I+2)*(X(I)-X(I+2))+V(I+2)*X(I)*X(I+1)*(X(I+1)-
     2 X(I)))/D
      A1=((V(I+2)-V(I+1))*X(I)**2+(V(I)-V(I+2))*
     1 X(I+1)**2+(V(I+1)-V(I))*X(I+2)**2)/D
      A2=(V(I)*(X(I+2)-X(I+1))+V(I+1)*(X(I)-X(I+2))+
     1 V(I+2)*(X(I+1)-X(I)))/D
      PRINT 71,D,A0,A1,A2,K
   71 FORMAT(1X,4F20.5,I8)
      DO 10 J=K,N
      K=J
      XX=XX+DX
      IF (XX.GT.X(I+1)) GO TO 11
   17 VV(J)=A0+A1*XX+A2*XX*XX
      XXX(J)=XX
   10 CONTINUE
      GO TO 12
   11 XX=XX-DX
      GO TO 13
   12 CONTINUE
      K=N+1
   31 K=K-1
      L=K-1
      IF (K.EQ.1) GO TO 33
```

```
      ZV=0.0
      DO 30 I=1,L
      AR=2.*VV(K)/(VV(I)+VV(I+1))
      DQ=(DX/PI)*ALOG(ABS(AR)+SQRT(ABS(AR*AR-1.)))
      ZV=ZV+DQ
   30 CONTINUE
      Z(K)=ZV
      GO TO 31
   33 CONTINUE
      Z(1)=0.0
      HH=0.
      J=0
      K=1
   80 J=J+1
      IF (HH.GT.Z(N)) GO TO 82
      HH=HH-DH
      DO 81 I=K,NK
      K=I
      HH=HH+DH
      IF (HH.GT.Z(J+1)) GO TO 80
      AQ=(HH-Z(J))/(Z(J+1)-Z(J))
      V1(I)=VV(J)+AQ*(VV(J+1)-VV(J))
      X1(I)=XXX(J)+AQ*(XXX(J+1)-XXX(J))
      Z1(I)=HH
   81 H1(I)=DH
   82 H1(1)=DH/2.
      H1(NK)=0.0
      PRINT 40,TTL
   40 FORMAT (/,3X,16A5,//,26H      DISTANCE   DEPTH      ,
     1 16HP-VEL   THICKNESS)
      PRINT 41,(X1(I),Z1(I),V1(I),H1(I),I=1,NK)
   41 FORMAT(5X,F6.1,4X,F6.0,3X,F7.1,3X,F6.0)
      STOP
      END
```

David N. Anderson
Executive Director
Geothermal Resources Council
P.O. Box 1033
Davis, CA 95616

Dr. James K. Applegate
Department of Geology
Boise State University
Boise, ID 83725

Mr. Sam Arentz, Jr., President
Steam Corporation of America
1720 Beneficial Life Tower
Salt Lake City, UT 84111

Dr. David J. Atkinson
Hydrothermal Energy Corp.
2519 Horseshoe Canyon Drive
Los Angeles, CA 90046

Dr. Carl F. Austin
c/o Geothermal Technology
Code 2661, NWC
China Lake, CA 93555

Mr. Lawrence Axtell
Axtell Resources, Inc.
645 San Julio Rd.
Solano Beach, CA 92075

Mr. Larry Ball
DOE
Division of Geothermal Energy
3rd Floor, MS 3122C
20 Massachusetts Ave., N.W.
Washington, DC 20545

Mr. Ronald Barr
Earth Power Corporation
P.O. Box 1566
Tulsa, OK 74101

Dr. Randy Beach
Anaconda
Min. Res. Gp.
555 17th St.
Denver, CO 80217

Dr. Rudolf A. Black
DOE
Dir. of Div. of Geothermal Energy
3rd Floor, MS 3122C
20 Massachusetts Ave., N.W.
Washington, DC 20545

Dr. David D. Blackwell
Southern Methodist University
Department of Geological Sciences
Dallas, TX 75275

Dr. Marvin G. Bloomquist
Research Associate
Mobil Research & Develop. Corp.
Research Dept.
P.O. Box 900
Dallas, TX 75221

Dr. Gunnar Bodvarsson
Oregon State University
School of Oceanography
1377 N.W. Alta Vista Dr.
Corvallis, OR 97330

Mr. C. M. Bonar
Director, Geothermal Projects
Atlantic Richfield Co.
P.O. Box 1829
Dallas, TX 75221

Roger L. Bowers
Hunt Energy Corp.
2500 1st Natl Bank Bldg.
Dallas, TX 75202

Gerald Brophy
DOE
Division of Geothermal Energy
3rd Floor, MS 3122C
20 Massachusetts Ave., N.W.
Washington, DC 20545

Mr. William D. Brumbaugh
Geophysics Bldg., Room 12
Interpretation Group
Conoco
Ponca City, OK 74601

Mr. Glen Campbell
Geothermal Supervisor
Gulf Min. Resource Company
1720 South Bell Aire St.
Denver, CO 80222

Regina Capuano
Earth Science Lab
391A Chipeta Way
Salt Lake City, UT 84108

Tom Cassel
Technecon Analytic Research, Inc.
2400 Chestnut Street
Philadelphia, PA 19103

Ray Chantler
McCulloch Oil Corp.
10880 Wilshire Blvd.
Los Angeles, CA 90024

Dr. Bob Christiansen
U.S. Geological Survey
345 Middlefield Road
Menlo Park, CA 94205

Eugene V. Ciancanelli
Consulting Geologist
12352 Escala Drive
San Diego, CA 92128

Dr. Jim Combs
Geothermal Services, Inc.
10072 Willow Creek Rd.
San Diego, CA 92131

Mr. F. Dale Corman, President
O'Brien Resources, Inc.
49 Toussin Avenue
Kentfield, CA 94904

Dr. R. Corwin
Dept. Eng. Geoscience
University of California @ Berkeley
Berkeley, CA 94720

Mr. Ritchie Coryell
Program Manager
National Science Foundation
1800 G Street, N.W.
Washington, DC 20050

Dr. Gary Crosby
Phillips Petroleum Company
71-C PRC
Bartlesville, OK 74003

Mr. W. L. D'Olier
Geothermal Operations
Thermal Power Co.
601 California Street
San Francisco, CA 94108

Mrs. Katie Dixon
3781 Lois Lane
Salt Lake City, UT 84117

Mr. William Dolan
Chief Geophysicist
Amax Exploration Inc.
4704 Harlan Street
Denver, CO 80212

John E. Dooley
R. F. Smith Corp.
552 E. 3785 S.
Salt Lake City, UT 84106

Robert C. Edmiston
Anadarko Production Co.
P.O. Box 1330
Houston, TX 77001

Mr. Samuel M. Eisenstat, President
Geothermal Exploration Co., Inc.
400 Park Ave.
New York City, NY 10022

Dr. Val A. Finlayson
Research Engineer
Utah Power and Light Company
1407 West North Temple
Salt Lake City, UT 84110

Mr. Milton Fisher
295 Madison Avenue
New York City, NY 10017

Mr. Ron Forrest, Geologist
Phillips Petroleum Co.
P.O. Box 858
Milford, UT 84751

Ken Fournier
Union Oil
Union Research Center
Box 76
Brea, CA 92621

Dr. Frank Frischknecht
Box 25046, Denver Federal Center
U.S. Geological Survey
Denver, CO 80225

Robert Furgerson
Argonaut Enterprises
1480 Hoyt Street
P.O. Box 26330
Denver, CO 80226

Mr. Gary Galyardt, Geologist
U.S. Geological Survey
MS 602
Box 25046, Federal Center
Denver, CO 80225

Ms. N. Sylvia Goeltz
UV Industries, Inc.
19th Floor, University Club Bldg.
Salt Lake City, UT 84111

Dr. N. E. Goldstein
Lawrence Berkeley Laboratory
Building 90
University of California, Berkeley
Berkeley, CA 94720

Mr. Steven M. Goldstein
The Mitre Corporation
Metrek Division
1820 Dolley Madison Blvd.
McLean, VA 22101

Robert Gray
DOE
Division of Geothermal Energy
3rd Floor, MS 3122C
20 Massachusetts Ave., N.W.
Washington, DC 20545

Mr. Bob Greider, V. P. Exploration
Intercontinental Energy Co.
P.O. Box 17529
Denver, CO 80217

Mr. J. H. Hafenbrack
Exxon Co. USA
P.O. Box 120
Denver, CO 80201

Mr. Dee C. Hansen
Utah State Engineer
442 State Capitol
Salt Lake City, UT 84114

Richard J. Haren
CSIRO Minerals Research Labs
Division of Mineral Physics
P.O. Box 136
North Ryde, N.S.W. 2113
AUSTRALIA

Dr. Norman Harthill
Executive Vice President
Group Seven, Inc.
9250 W. 5th Ave.
Lakewood, CO 80226

Dan E. Haymond
P.O. Box 239
Salt Lake City, UT 84110

Mr. Jack Von Hoene
Davon, Inc.
250 North 100 West
Milford, UT 84751

George Hopkins
Geotronics Corp.
10317 McKalla Place
Austin, TX 78758

Mr. Gerald W. Huttrer, Sr. Geologist
Intercontinental Energy Corporation
7503 Marin Dr., Suite 1-C
Englewood, CO 80110

Cohut I. Ioan
Parcul Petofi II
3700 - Oradea
ROMANIA

Mr. Laurence P. James
2525 South Dayton Way #1406
Denver, CO 80231

Dr. George R. Jiracek
Department of Geology
University of New Mexico
Albuquerque, NM 87131

Mr. Richard L. Jodry
P.O. Box 941
Richardson, TX 75080

Dr. Paul Kasameyer
Lawrence Livermore Lab, L-224
P.O. Box 808
Livermore, CA 94550

Dr. George Keller
Professor and Head
Department of Geophysics
Colorado School of Mines
Golden, CO 80401

Mr. James B. Koenig
Geothermex
901 Mendocino Avenue
Berkeley, CA 94704

Dr. George A. Kolstad
DOE
Mail Stop J309
Germantown, MD 20545

Dr. Phillip N. LaMori
Occidental Research Corp.
2100 S.E. Main Street
P.O. Box 19601
Irvine, CA 92713

Dr. Mark Landisman
Professor of Geophysics
University of Texas, Dallas
Box 688
Richardson, TX 75080

A. W. Laughlin, Group Leader
Geothermal Programs, Geol Appl Grp G-9
Los Alamos Scientific Laboratory
P.O. Box 1663
Los Alamos, NM 87545

Mr. Guy W. Leach, Geologist
Oil Development Company of Texas
Box 12053, American Natl Bank Bldg.
Amarillo, TX 79101

Dr. T.J. Lee
L.A. Research and Assoc. Pty. Ltd.
P.O. Box 217
Gordon, N.S.W., 2072
Australia

Mr. Dick Lenzer
Phillips Petroleum Company
P.O. Box 239
Salt Lake City, UT 84110

Earth Sciences Division Library
Building 90
University of California
Lawrence Berkeley Laboratory
1 Cyclotron Road
Berkeley, CA 94720

Don R. Mabey
U.S. Geological Survey
Rm. 468, Post Office Bldg.
Salt Lake City, UT 84101

Charles William Mase
Geothermal Studies
Mail Stop 18
U.S. Geological Survey
345 Middlefield Road
Menlo Park, CA 94025

Mr. Skip Matlick
Republic Geothermal
P.O. Box 3388
Santa Fe Springs, CA 90670

James O. McClellan, President
Geothermal Electric Systems Corp.
5278 Pinemont Drive, Suite A-150
Salt Lake City, UT 84107

Dr. Robert B. McEuen
Exploration Geothermics
5202 College Gardens Court
San Diego, CA 92115

Clifton McFarland
DOE
Division of Geothermal Energy
3rd Floor, MS 3122C
20 Massachusets Ave., N.W.
Washington, DC 20545

Mr. Don C. McMillan
Utah Geological & Mineral Survey
606 Blackhawk Way, Research Park
Salt Lake City, UT 84108

Dr. Tsvi Meidav
Consultant
40 Brookside Ave.
Berkeley, CA 94705

Mr. Frank G. Metcalfe, Pres.
Geothermal Power Corporation
1127 Grant Ave., Suite 6
P.O. Box 1186
Novato, CA 94947

Dr. Martin Molloy
U.S. DOE
133 Broadway
Oakland, CA 94612

Dr. Frank Morrison
Professor of Geophysics Eng.
University of California
Hearst Mining Building
Berkeley, CA 94720

Dr. L. J. Patrick Muffler
U.S. Geological Survey
345 Middlefield Road
Menlo Park, CA 94205

Dr. Steven R. Munts
Cominco American Inc.
E. 15120 Euclid
Spokane, WA 99210

Mr. Clayton Nichols
DOE
Division of Geothermal Energy
Idaho Operations Office
550 Second Street
Idaho Falls, ID 83401

Dennis Nielson
Earth Science Lab
391A Chipeta Way
Salt Lake City, UT 84108

Mr. Carel Otte
President of Geothermal Division
Union Oil Company
P.O. Box 7600
Los Angeles, CA 90051

Roy Parodi
American Thermal Resources Inc.
950 E. Katella, Suite 9
Orange, CA 92667

Dr. Wayne Peeples
Dept. of Geological Sciences
Southern Methodist University
Dallas, TX 75221

H. Dean Pilkington
Amax Exploration, Inc.
4704 Harlan Street
Denver, CO 80212

Mr. C. R. Possell
General Ener-Tech, Inc.
4842 Viane Way
San Diego, CA 92110

Dr. Kenneth Poulson
Brush Wellman
67 W. Century Pkwy
S.L.C., UT 84115

Dr. Alan O. Ramo
Sunoco Energy Development Co.
12700 Park Central Pl.
Suite 1500, Box 9
Dallas, TX 75251

Marshall Reed
DOE
Division of Geothermal Energy
3rd Floor, MS 3122C
20 Massachusetts Ave., N.W.
Washington, DC 20545

Robert S. Reed
Thermogenics, Inc.
c/o Hughes Aircraft
Centinela and Teale
Culver City, CA 90230

Dr. Robert W. Rex, President
Republic Geothermal, Inc.
11823 E. Slauson Ave., Suite 1
Santa Fe Springs, CA 90670

Ms. Barbara Ritzma
Science & Engineering Department
Marriott Library
159 MLi, CAMPUS

Dr. Jack Salisbury
DOE
Division of Geothermal Energy
3rd Floor, MS 3122C
20 Massachusetts Avenue, N.W.
Washington, DC 20545

Dr. Konosuke Sato
Metal Mining Agency of Japan
Tokiwa Bldg.
1-24-14 Toranomon
Minato-Ku, Tokyo
JAPAN

Dr. John V. A. Sharp
Hydrosearch, Inc.
333 Flint Street
Reno, NV 89501

Mr. Wayne Shaw
Getty Oil Company
P.O. Box 5237
Bakersfield, CA 93308

S. Shikinami
Shingen Kaihatsu K.K.
Fukuyoshicho Annex #301
22-18, Akasaka 2-Chome,
Minato-Ku, Tokyo 107 JAPAN

Mr. Gregory L. Simay
City of Burbank - Public Service Dept.
164 West Magnolia Blvd.
Burbank, CA 91503

Mr. W. P. Sims
DeGolyer and MacNaughton
One Energy Square
Dallas, TX 75206

Dr. H. W. Smith
Department of Electrical Engineering
University of Texas, Austin
Austin, TX 78712

Marty Steyer
Natl Geothermal Info Resource
Lawrence Berkeley Lab, 50A-0143A
Univ. of California
Berkeley, CA 94720

Mr. Paul V. Storm
California Energy Company, Inc.
Wells Fargo Bldg., Suite 300
P.O. Box 3909
Santa Rosa, CA 95402

Dr. Chandler Swanberg
New Mexico State University
P.O. Box 4408
University Park Dr.
Las Cruces, NM 88003

Dr. Charles M. Swift, Jr.
Chevron Oil Co.-Minerals Staff
P.O. Box 3722
San Francisco, CA 94105

Dr. Bernard Tillement
Aquitaine Co. of Canada
2000 Aquataine
540 5th Avenue, S.W.
Calgary, Alberta
Canada 2TP OM4

David D. Tillson
Washington Public Power Supply System
P.O. Box 968
Richland, WA 99352

Dr. Ronald Toms
DOE
Division of Geothermal Energy
3rd Floor, MS 3122C
20 Massachusetts Avenue, N.W.
Washington, DC 20545

Alan Tratner
Geothermal World Corp.
18014 Sherman Way, Suite 169
Reseda, CA 91335

Dr. John Tsiaperas
Shell Oil Company
Box 831
Houston, TX 77001

Dr. A. F. Veneruso
Geothermal Technology Division 5736
Sandia Laboratories
Albuquerque, NM 87115

Dan Vice
555 Park Lane
Billings, MT 59102

Dr. James R. Wait
Rx7, Room 242, RB1
U.S. Dept. of Commerce
National Oceanic & Atmospheric Admin.
Environmental Research Labs
Boulder, CO 80302

John Walker
DOE
Division of Geothermal Energy
3rd Floor, MS 3122C
20 Massachusetts Ave., N.W.
Washington, DC 20545

Mr. D. Roger Wall, Geologist
Geothermal Resources Division
Aminoil USA, Inc.
1250 Coddingtown Center
Santa Rosa, CA 95401

Dr. Paul Walton, President
American Geological Enterprises, Inc.
1102 Walker Bank Bldg.
Salt Lake City, UT 84111

J. L. Wilson
4321 Post Road
San Diego, CA 92117

Ed Witterholt
City Services Oil Co.
Energy Research Lab
Box 50408
Tulsa, OK 74150

Mr. William B. Wray, Jr.
VanCott, Bagley, Cornwall & McCarthy
141 East 1st South
Salt Lake City, UT 84111

Dr. Paul C. Yuen
University of Hawaii @ Manoa
2540 Dole Street, Holmes 240
Honolulu, HI 96822

Dr. S. H. Yungul
Chevron Resources Co.
P.O. Box 3722
San Francisco, CA 94119

Dr. Elliot J. Zais
Elliot Zais & Associates
7915 N.W. Siskin Dr.
Corvallis, OR 97330

Kenneth L. Zonge
Zonge Engineering & Res.
5634 E. Pima Street
Tucson, AZ 85712

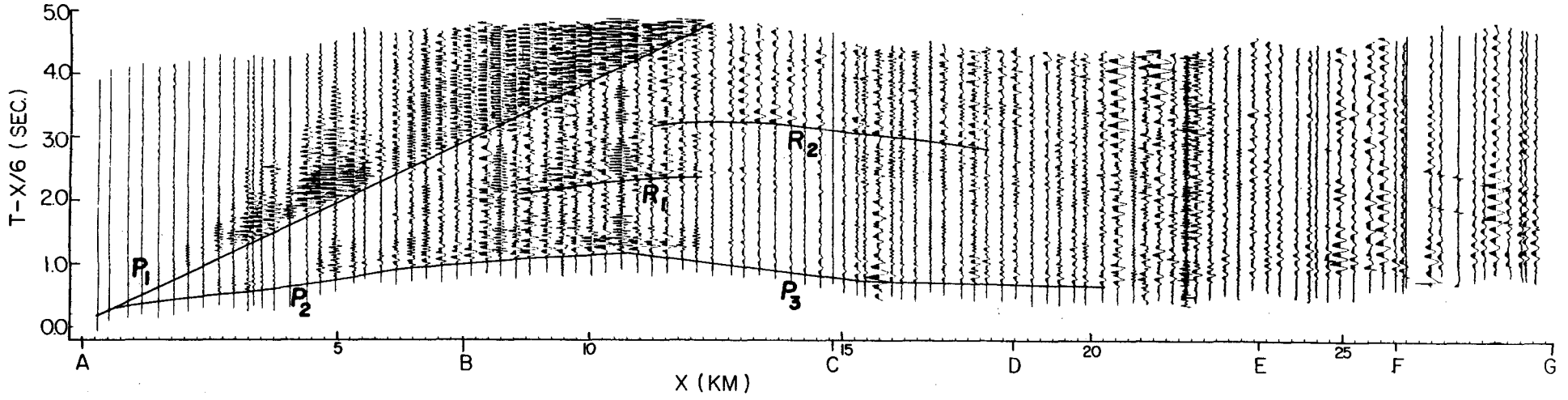

Figure 13. Normalized seismograms from shot point A. Amplitudes have been multiplied by x^3 where x equals the distance from the shot point. P-wave phases labeled according to Figure 12.

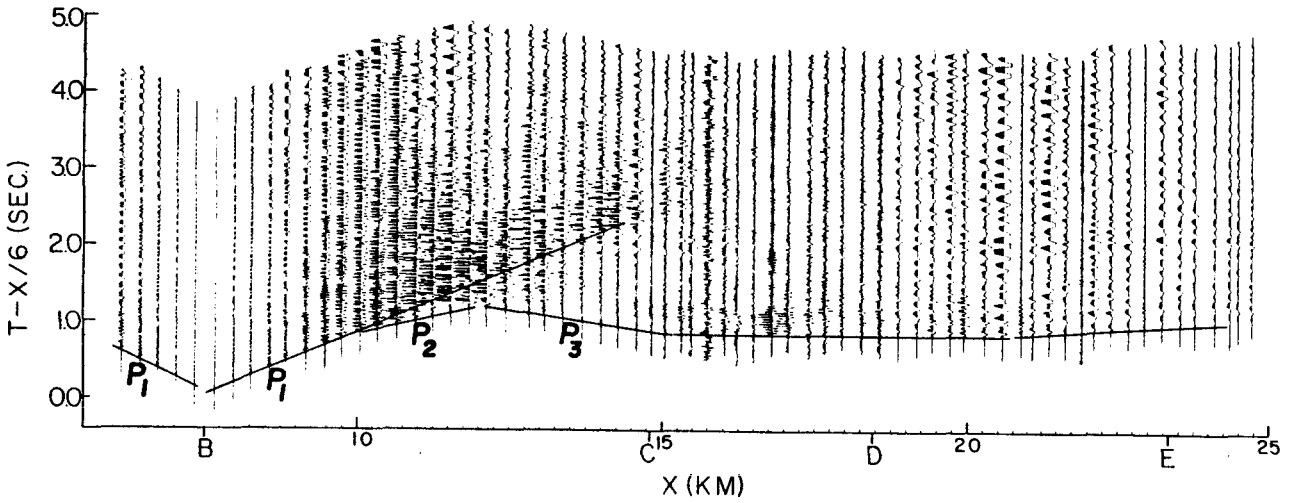

Figure 14. Normalized seismograms from shot point B. Amplitudes have been multiplied by $x^{3/2}$ where x equals the distance from the shot point. P-wave phases labeled according to Figure 12.

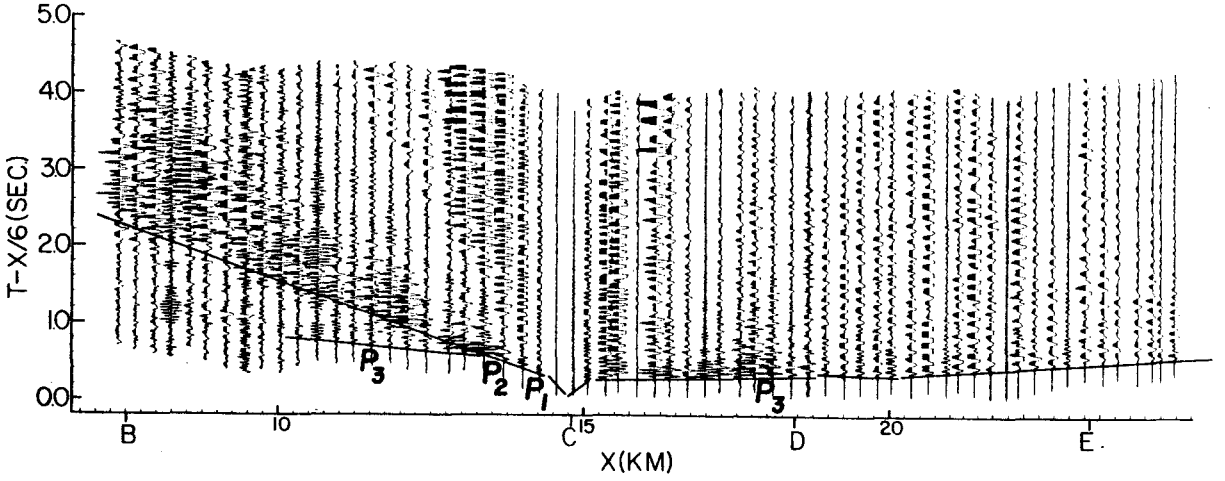

Figure 15. Normalized seismograms from shot point C. Amplitudes have been multiplied by $x^{3/2}$ where x equals the distance from the shot point. P-wave phases labeled according to Figure 12.

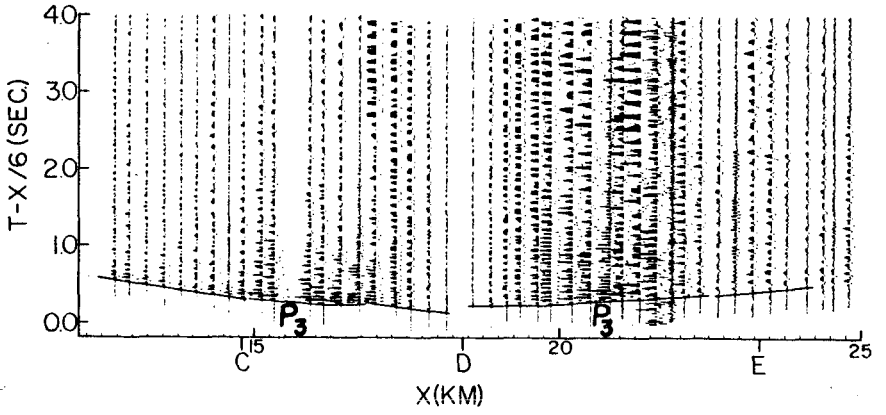

Figure 16. Normalized seismograms from shot point D. Amplitudes have been multiplied by $x^{3/2}$ where x equals the distance from the shot point. P-wave phases labeled according to Figure 12.

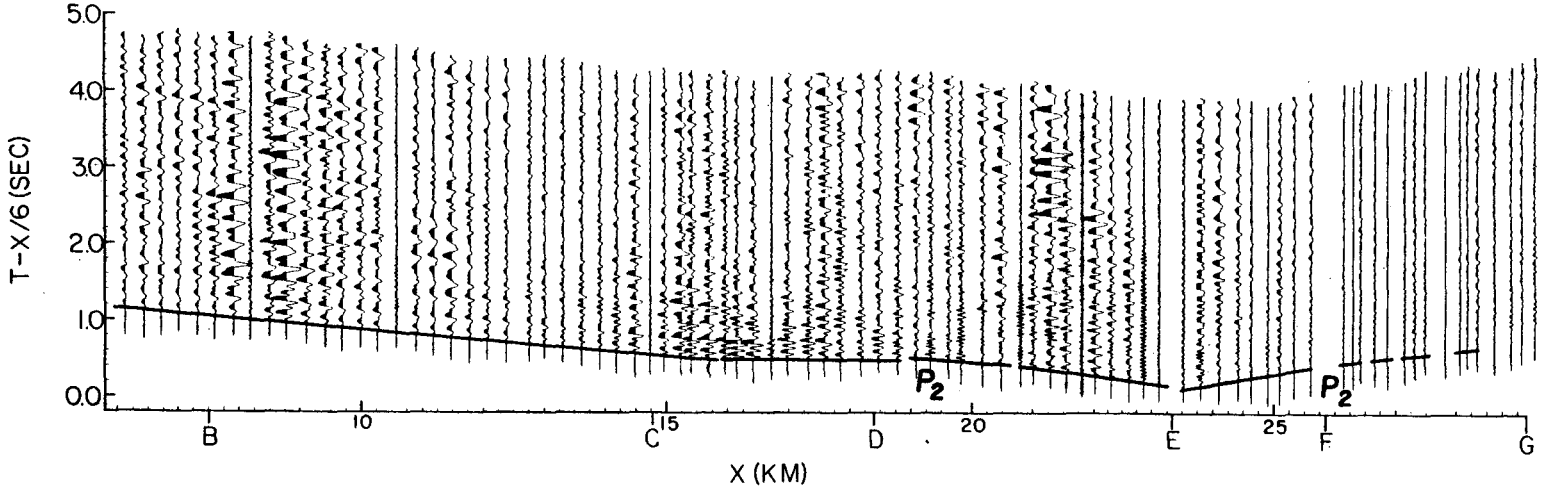

Figure 17. Normalized seismograms from shot point E. Amplitudes have been multiplied by $x^{3/2}$ where x equals the distance from the shot point. P-wave phases labeled according to Figure 12.

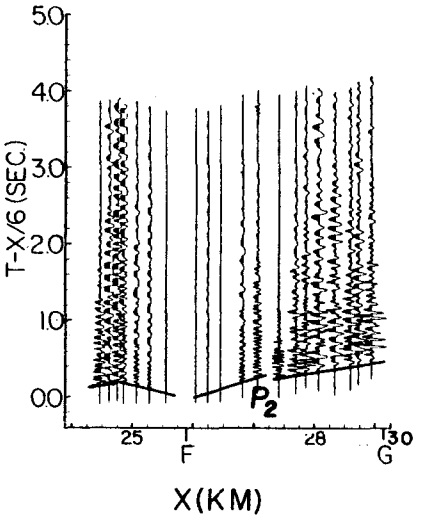

Figure 18. Normalized seismograms from shot point F. Amplitudes have been multiplied by $x^{3/2}$ where x equals the distance from the shot point. P-wave phases labeled according to Figure 12.

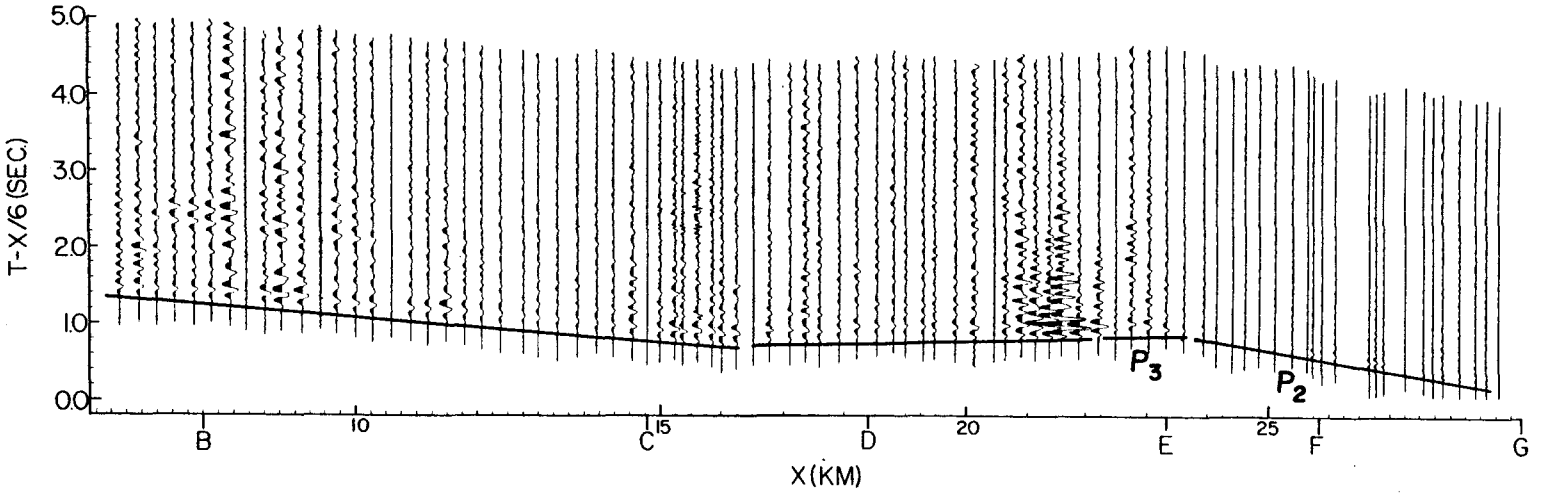

Figure 19. Normalized seismograms from shot point G. Amplitudes have been multiplied by $x^{3/2}$ where x equals the distance from the shot point. P-wave phases labeled according to Figure 12.